Scuola Internazionale Superiore di Studi Avanzati - Trieste

Mechanical Unfolding of the Cytosolic Domain from hHCN2 Channel by using Single Molecule Force Spectroscopy

Pedroni Andrea

(2012-2016)

Supervisor: **Prof.Vincent Torre**

Thesis submitted for the partial fulfillment
of Doctor of philosophy in Neurobiology

SISSA - Via Bonomea 265 - 34136 TRIESTE - ITALY

Declaration of Authorship

The thesis and the work presented in it was done wholly or mainly while in candidature for PhD title at SISSA - Scuola Internazionale Superiore di Studi Avanzati between November 2012 and December 2016, under the supervision of Professor Vincent Torre. Where the thesis is based on work done by myself jointly with others, I have made clear exactly what was done by others and what I have contributed myself. Where I have consulted the published work of others, this is always clearly attributed.

SISSA - SCUOLA INTERNAZIONALE SUPERIORE DI STUDI AVANZATI

Abstract

Area of Neurobiology
Neurobiology Area

Doctor of Philosophy

Mechanical Unfolding of the Cytosolic Domain from hHCN2 Channel by using Single Molecule Force Spectroscopy

by Andrea PEDRONI

Atomic force microscopy (AFM)-based single molecule force spectroscopy (SMFS) has emerged into a reliable technique for probing structural and mechanical properties of biological samples at molecular level. It has been successfully applied to investigate the mechanical unfolding of soluble proteins as well as membrane proteins. In contrast with the traditional structural techniques it provides a direct mechanical interaction with targets molecule in their near-physiological environment. The possibility to sample one molecule at a time, made the techniques extremely valuable for studying complex dynamic behaviors, unveiling rare events that are usually averaged in large data distribution from big populations of molecules. Here we investigate the mechanical unfolding of the purified cytosolic c-linker and cyclic nucelotide binding domain (CNBD) domain from the human hyperpolarization-activated and cyclic nucleotide-gated (hHCN)2 channel, and characterize the ligand-depended differences in the unfolding behaviour of the molecule. In parallel, we develop an all-in-one environment for Force vs distance (F-d) curves analysis, containing informatics tools to handle the reproducibility and automation required for exploring stochastic processes like folding and unfolding of complex proteins.

Contents

List of Figures

List of Abbreviations

aa	**a**mino**a**cid
a/r	**a**pproach/**r**etraction (cycle)
AFM	**A**tomic **F**orce **M**icroscopy
cAMP	**c**yclic **A**denosine **M**ono**P**hosphate
CNBD	**C**yclic **N**ucleotide **B**inding **D**omain
CNG	**C**yclic **N**ucleotide-**G**ated (channel)
cryo-EM	cryo-**E**lectron **M**icroscopy
DFS	**D**ynamic **F**orce **S**pectroscopy
F	**F**olded (state)
F-d	**F**orce versus **d**isplacement (curve)
FFM	**F**riction **F**orce **M**icroscopy
HCN	**H**yperpolarization-activated **C**yclic **N**ucleotide-gated (channel)
MFM	**M**agnetic **F**orce **M**icroscopy
MWNT	**M**ulti **W**all **N**ano **T**ube
NMR	**N**uclear **M**agnetic **R**esonance
SEFM	**S**canning **E**lectron **F**orce **M**icroscopy
SKPM	**S**canning **K**elvin **P**robe **M**icroscopy
SMFS	**S**ingle **M**olecule **F**orce **S**pectroscopy
SNOM	**S**canning **N**ear-field **O**ptical **M**icroscopy
SNR	**S**ignal to **N**oise **R**atio
SPM	**S**canning **P**robe **M**icroscopy
STM	**S**canning **T**unnel **M**icroscopy
SWNT	**S**ingle **W**all **N**ano **T**ube
TEM	**T**rasmission **E**lectron **M**icroscopy
TM	**T**rans**m**embrane
TMD	**T**rans**m**embrane **D**omain
TS	**T**ransition **S**tate
TTS	**T**ip **S**ample **S**eparation
U	**U**nfolded (state)
WLC	**W**orm **L**ike **C**hain (model)

List of Symbols

$\ddagger$	energy barrier
Å	angstrom
cos	cosine
E	Young's modulus
exp	exponential
F	force
F_N	normal force
G	Gibb's free energy
H	enthalpy
Hz	hertz
I	current
I_f	funny current
I_h	hyperpolarizing current
kDa	kilodalton
k	spring constatn
k_0	unfolding rate
k_B	Boltzmann constant
k_F	unfolding rate under external force
l	length
L_c	contour length
ln	natural logarithm
ms	millisecond
mV	millivolt
N	newton
n	number
nm	nanometer
p	persistence length
Q	heat
S	entropy
$S(1-6)$	transmembrane helices
r	loading rate
s	second
T	temperature
t	time
V	volt

w	width
x_β	length along reaction coordinates in two state model
x_u	distance between folded and transition state in two state model
Δ	differential
θ	angle of energy landscape tilting under external force
μ	micro
ϱ	thickness
τ	relaxation time

To my family

Chapter 1

Protein Structure and Function

Proteins are the major and more versatile functional elements in living systems. They are deeply involved in all the processes concerning cellular life, including mechanical support and movement generation, catalysis, transport and storage of other molecules, immune protection, growth and differentiation, and many others (Berg et al., 2002). The extraordinary diversity and specificity of proteins function reside in their precise structural determination, which is the final result of one of the most crucial and complex physical-chemical process taking place in the cells: the protein folding. During this process a linear chain of amino acids (primary structure) gets a defined three-dimensional conformation (tertiary structure), at the end of which the formed protein may assume its specific biological function. Cellular physiological health depends on the success of this process and disease on its failure (Luheshi et al., 2008).

1.1 Protein Folding Problem

In 1962 Max Perutz and John Kendrew were awarded the Nobel Prize in Chemistry for their pioneering work in the first ever application of X-ray crystallography in structural determination of two globular proteins: haemogobin and myoglobin (Kendrew et al., 1958; Kendrew et al., 1960; Perutz et al., 1960) (Figure 1.1). The emerged internal regularity in the structure was partially expected, in fact conformational arrangement such as α-helices had already been predicted by Linus Pauling some year before (Pauling et al., 1951; Pauling and Corey, 1951). Nonetheless, the irregularity in the packaging of those α-helices was totally unexpected. These observations gave rise to a series of new questions and focused the interest on the comprehension of the relationship existing between structure and function of proteins and organic macromolecules. In this contest, became extremely relevant to solve the so-called *"protein folding problem"*, that can be regarded as three main questions: (i) which is the proper code driving the primary amino acidic sequence to its three-dimensional active conformation; (ii) what are the physical-chemical principles leading this process; (iii) how to predict the final protein structure starting from the primary amino acidic sequence (Dill et al., 2008; Dill and MacCallum, 2012). The first relevant insight into the question came from Christian Anfinsen's experiments on the renaturation of the

Figure 1.1. The first known structure of a globular protein, obtained by Kendrew and colleagues in 1958: myoglobin at 6 Å resolution. (Kendrew et al., 1958).

ribonuclease A (Anfinsen et al., 1954; Anfinsen et al., 1961). He demonstrated that small globular proteins reversibly fold, by themselves and in the absence of any catalytic biomolecules, only depending on the amino acidic sequence and their physiological environment. Those observations leaded to the formulation of the so-called thermodynamic hypothesis (or *"Anfinsen's dogma"*) of protein folding (Anfinsen, 1973), described in his 1972 Nobel prize acceptance lecture as follows: *"This hypothesis states that the three-dimensional structure of a native protein in its normal physiological milieu (solvent, pH, ionic strength, presence of other components such as metal ions or prosthetic groups, temperature, and other) is the one in which the Gibbs free energy of the whole system is lowest; that is, that the native conformation is determined by the totality of interatomic interactions and hence by the amino acid sequence, in a given environment."* In other words, folded proteins do exist in a global minimum free-energy state, no other thermodynamically stable configurations with comparable free energy levels may exist, the free-energy minimum needs to be kinetically accessible (no formation of intermediate complexes or deviations in shaping process), and reasonably small changing in the surrounding environment cannot bring the system to escape from its minimum free-energy state. An idealization of this concept is depicted in Figure 1.2 (a), where the folded protein is considered to lay into the free-energy minimum at the bottom of a flat and smooth (*kinetically accessible*), high and steep (*stable*) energy surface. This repre-

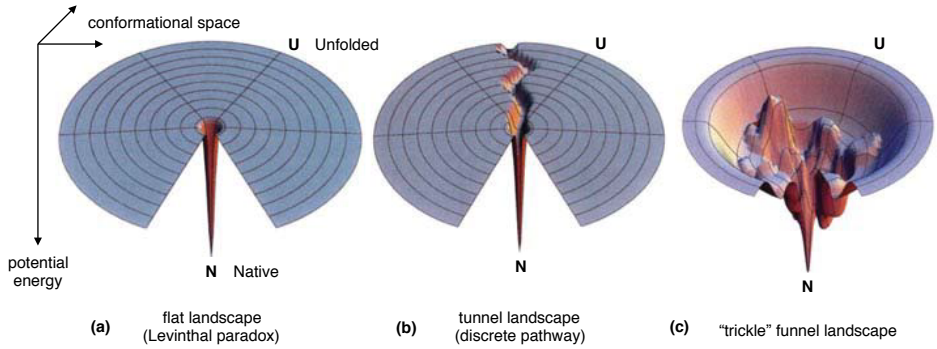

Figure 1.2. Conceptual energy landscape evolutions for protein folding. a) *"Levinthal golf course"* with a wide and flat conformational space, lacking in an energy gradient and with an insurmountable entropic barrier. b) *"Tunnel landscape"* with a single narrow folding pathway, misleading in describing proteins landing off the single pathway. c) Trickle funnel-shaped landscape with possible detours around local energy maxima and entropic delay in low gradient regions. (Dill and Chan, 1997).

sentation is also known as *"Levinthal golf course"*, thanks to the molecular biologist Cyrus Levinthal who in 1969 proposed a paradox pointing out some inaccuracies in this model and in thermodynamic hypothesis itself. The so-called *"Levinthal paradox"* states that it would be virtually impossible for a protein to sample all the available structural arrangements, searching for the native configuration, in a biologically meaningful time. The absence of an energy gradient would present the protein with an insurmountable entropic barrier to find the minimum free-energy state. For example: considering 2 rotational angles for each residue composing a primary amino acid sequence, an n residues long protein would have 2^n possible rotational angles to experience. Now, supposing for each rotational angle 3 stable states (that's an underestimated value), the protein would have $32^n \sim 10^n$ possible conformation, so that, if the average speed of rearrangement for a single chemical bound is $10^{-13} s$, the protein will take t=$10^n/10^{13} s$ as total time for systematically explore every possible conformation. It means that for a (small) protein composed by 100 residues, the total time taken for reaching its native state could be t=$10^{87} s$, a time much longer than the age of the universe ($\sim 6 \times 10^{17} s$). The disagreement between this theoretical time counting and the actual folding time (that is in the order of μs or ms) represents the paradox, underlining that the protein folding cannot be just considered as a random walk through all the possible conformations (Levinthal, 1969). This paradox raised questions about the kinetic of the folding process and Levinthal himself proposed the notion of protein folding pathway as preferential route through which a protein may quickly converge to its native states. However, even the single pathway model, depicted as *"tunnel landscape"* in Figure 1.2 (b), fails in describing proteins that eventually lands off

the narrow pathway. Again, due to the lack of an energy gradient out of the pathway, it would be impossible for those proteins experience a huge number of conformations searching for the pathway in reasonable biological time. Ever since, there have been multiple studies (largely kinetic-experimental studies) exploring specific folding pathway hypothesis, but the solution to this problem emerged from statistical thermodynamics, in particular from the energy landscape theory (Bryngelson and Wolynes, 1987; Leopold et al., 1992; Bryngelson et al., 1995; Dill and Chan, 1997). Models of foldable polymers suggested that more compact, low-energy conformational ensembles have fewer conformations, indicating that protein folding energy landscapes would have been funnel-shaped, following a kinetic gradient, becoming narrower toward the bottom (Figure 1.2 (c)).

Nowadays, the most widely accepted model describes the protein folding as a hierarchic process just going down to a rough funnel-shaped energy landscape via multiple parallel pathways, towards the native state to the bottom of the funnel (Yon, 2002) (Figure 1.3). At the highest energy state, the unfolded structure

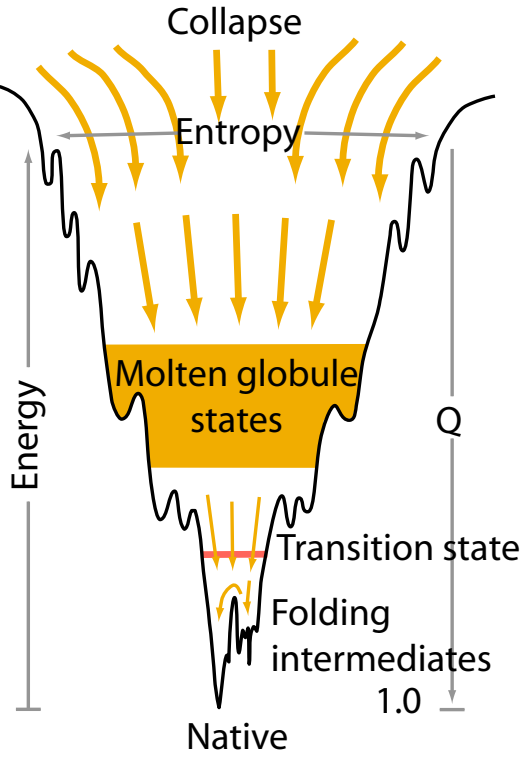

Figure 1.3. Hierarchic termodinamically driven funnel-shapped energy lanscape model. (Englander and Mayne, 2014).

exists in a polar solvent. Considering the protein-solvent as an isolated system, during the folding process the total entropy has to increase: $\Delta S_{\text{prot}} + \Delta S_{\text{sol}} \geq 0$, where ΔS_{prot} is the protein entropy, and ΔS_{sol} is the solvent entropy. The polar molecule of the solvent (mainly water molecules), may interacts whit polar side chains of amino acidic residues by hydrogen bounding, forming a solvation

shell. In this phase, the primary structure may arrange itself in the spontaneous formation of ordered local structural elements (helices and turns), and solvation shell maintains the stability of these structures within localized segments of the nascent protein. As the protein gets local stable structure it absorbs heat Q form the environment , so that ΔS_{sol} = -Q/T, where -Q is the heat absorbed from the protein by the environment, so that Q - $T\Delta S_{\text{prot}} \leq 0$. In an isobaric process, as the system does not perform work, the hentalpic variation is $\Delta H = Q$. The energy variation is $\Delta G = \Delta H$ - $T\Delta S_{\text{prot}}$, so that:

$$\Delta G = \Delta H - T\Delta S_{\text{prot}} \leq 0 \tag{1.1}$$

Where, T = const (in an isothermal process), and G represents the Gibbs free-energy of the protein coherently with the tendency of the system to gets a minimum free-energy state. However, as the system progresses to the native state, ΔS_{prot} should decrease disfavoring the condition states from the equation 1.1. Non-polar (hydrophobic) side chains of amino acid residues cannot interact with polar molecule of the solvent and that leads to a redaction in dissociative degrees of freedom for the molecule, and local decreases in the entropy along the amino acidic chain occur. The aggregation of hydrophobic regions reduces the surface area of the solvent exposed to non-polar side chains, reducing in turns the localized areas of decreased entropy, and leads to an increased entropy of the solvent, fulfilling the condition in the equation 1.1. This process is called "hydrophobic collapse" and it strongly contributes to balance the entropy decrease of the polypeptide, as it reaches a more ordered state, and the overall entropy increasing within the protein-solvent system. Moreover, the increasing level of structuration and stable interaction within the nascent protein, reduce the number or available conformations, decreasing both entropy (narrowing of the funnel) and energy (deepening of the funnel). That contributes to continuously thermodynamically "push" down the protein along the funnel (Tanford, 1978). Kinetically, in this phase folding intermediates seemed to form asynchronously over a range of time scales suggesting the coexistence of multiple unfolding routes rather than a single path (Roder et al., 1988). After the hydrophobic collapse the partially folded nascent protein crosses the so-called "molten globule" phase, exhibiting native-like secondary structures but still a loose and dynamic tertiary structure (Kuwajima, 1989; Semisotnov et al., 1991). Ideally, the molten globule corresponds to the narrow region of the funnel-shaped energy landscape, in which the protein is supposed to exist in a significantly lower free-energy configuration respect to the unfolded state, but still separated from the native by a transition state (Ohgushi and Wada, 1983; Onuchic et al., 1995). The local roughness along the funnel represents possible transient trapping of protein configurations in local free energy minima (Leopold, 1992; Bryngelson et al., 1995). Deeper

local minima may trap the protein in a misfolded state from witch it cannot escape (kinetic traps), and it corresponds to a failure of the protein folding process, usually leading to severe pathological consequences (Dobson, 2003; Luheshi et al., 2008). Concluding, the process of protein folding can be considered essentially thermodynamically controlled, driven by the decrease in Gibbs free-energy and regulated by various types of forces, including the enthalpic contribution of non-covalent bond formations, entropic effects of uptake or release of solvent molecules, burial of non-polar (hydrophobic) forming surfaces and restrictions in rotational and translational degrees of freedom (Ji and Liu, 2011). However, despite more than 50 years of advances and increasing knowledge in the fields, the physical and biochemical principles supporting the protein folding process remain not fully understood and still there is not general agreement on them.

1.2 Membrane Protein Folding

At the beginning, the membrane proteins folding process remains even more unclear respect to the soluble proteins folding problem. Only years after the results obtained by Kendrew and colleagues with globular proteins (Kendrew et al., 1958), Henderson and co-worker were able to obtained a 7 Å resolution model of the bacteriorhodopsin from purple membrane, offering the first ever structure solved for a membrane protein (Henderson and Unwin, 1975). The work revealed a packaged ensemble of transmembrane (TM) helices, perpendicularly spanning the lipid bilayer. Moreover, it was becoming evident as the amino acids sequence of membrane proteins, exhibits a sort of over-organization in regions of consecutive hydrophobic residues, long enough to cross the membrane if organized in helical structures (Kyte and Doolittle, 1982). Although, α-helices can been considered the main building blocks for transmembrane proteins, other constitutive structure like β-barrels and half TM helices, have been observed (Cuthbertson et al., 2005; Bigelow et al., 2004). Unlike soluble proteins that fold in an isotropic milieu, the entire transmembrane proteins folding process is though to take place into the well-defined environment of the membrane. The lipid bilayer present a symmetric organization with a central non-polar hydrocarbon core, constituted by aliphatic lipid chains, and an external interface composed by the polar lipid headgroups surrounded by a thick layer of water molecules (Tieleman et al., 1999). Thus, the hydrophobicity of the residues composing the helical structures became extremely relevant in the process of thermodynamic partitioning between the water and the lipid matrix, both during the protein insertion into the membrane (see below) and in the maintaining of their native conformation. The process by which a nascent transmembrane protein reaches is native state into the lipid bilayer can be divided in to distinct steps (Popot and Engelman, 1990). During the first step the protein is inserted into the membrane with the fundamental involvement of the so-called *translocon* machinery (see below). After that,

a second phase provides the assembling and the conformational rearrangement to make the protein gets the tertiary and the quaternary structure.The translocon machinery (also named *SecY* complex in bacteria and the *Sec61* complex in eukaryotes) consists of a hydrophilic cavity inserted into the membrane, direcltly interacting with ribosomes.

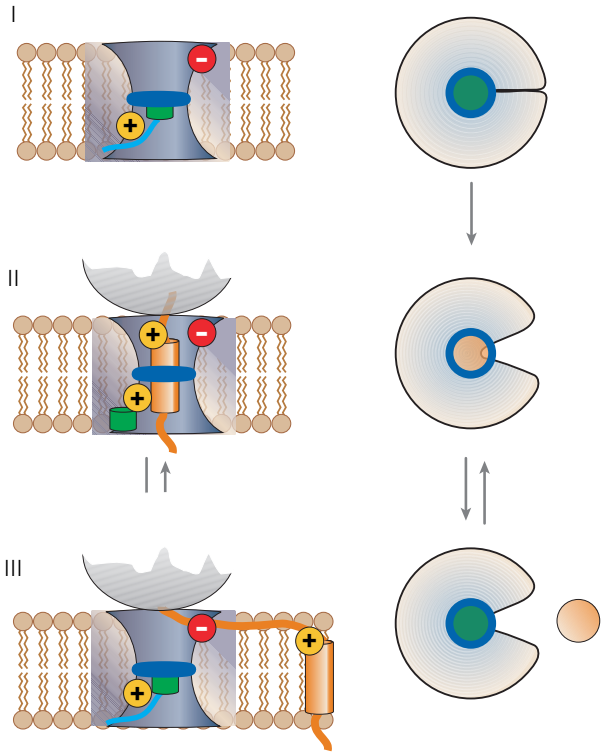

Figure 1.4. Sec61 translocon structure and functional model. (Bowie, 2005).

A translocon (Figure 1.4) has a diameter of few tens of Angstroms and can accommodates parts of the nascent peptides composed of about twenty amino acid residues at a time, which is sufficient to form a trasmembrane α-helix (Sadlish et al., 2005). It directly receives the translated nascent proteins within its hydrophilic cavity, and through a periodically opening of a lateral "gate", it makes the segment senses the environment and partitions due to its specific constitutive residues (Heinrich et al., 2000; Hessa et al., 2005). Thus, the translocon system provides to the right orientation for each new-formed segment, deciding whether it has to cross the membrane going to face the intracellular side or has to be settled into the lipid bilayer (Berg et al., 2004; White, 2007; Rapoport, 2007). Generally, hydrophobic sequences are inserted into the membrane, whereas hydrophilic sequences cross the membrane through the pore or emerge between the translocon

and the ribosome. After the insertion the forming protein needs to reach its stable and native conformation. Evidence suggest in this phase membrane proteins behave like soluble proteins, thermodynamically descending a funnel-shaped energy landscape thought multiple pathways, toward an energy minimum (Lu and Booth, 2000). However, membrane proteins folding process has to be idealized as more determined and less extended in terms of entropy. Indeed, the polypeptide partitioning in the bilayer, the lipid protein interaction, as well as the interaction within the protein itself, significantly reduce the possible structural arrangements of the nascent protein.

1.3 Structural investigation Techniques

One of the unsolved issues in protein folding problem remains how to determine the three-dimensional final conformation of a polypeptide just starting from the amino acid sequence. Even if *in silico* methodologies have considerably advanced, there is still no way to consistently predict protein structures with high accuracy, starting from the primary structure (Moult, 1999; Floudas et al., 2006). Therefore, to have insights at atomic level resolution of individual and complexes of biological molecules, experimental methodologies are still required and are widely used. Among them, three main techniques can be counted: X-ray crystallography, nuclear magnetic resonance (NMR) spectroscopy, and electron cryo-microscopy (cryo-EM). Each of them presents both advantages and disadvantages or limitation in terms of sample preparation, data collection and analysis. Synchrotron-based X-ray protein crystallography, as mentioned above, has been successfully used since the half of the last century to solve proteins structure. NMR has emerged as complementary method, making them the most routinely used techniques for determine structure and dynamic of proteins at atomic resolution. Both methods determine time and spatial averages of properties from an extremely large ensemble of molecule and have a comparable resolution limit of about 2 - 3.5 Å. X-ray crystallography depicts an average conformation coming from many static snapshots obtained by the diffraction pattern of X-rays that are shot through to a crystallized matrix containing the protein. The pattern is determined by the electron density within the crystal, and the diffraction is the result of an interaction between the high energy X-rays and the electrons of the atom composing the molecule. It can be applied to large molecular complexes (> 100 kDa), but it is limited to molecules that can be purified and crystalized. The crystal growing is an empirical procedure and there are no established rules to obtain good crystals, so that a different protocol needs to be tuned for every new type of protein. A high concentration of purified protein must bee available. Moreover, the crystal lattice may affect the inter-molecular packaging and the molecule may results as stacked in non-physiological sub-states. Generally, membrane proteins result in more difficult procedure for crystallization rather than soluble proteins,

because thir stability and structure are strictly dependent on the lipid bilayer in which they are embedded (Drenth, 2007).

NMR is a more suitable technique for smaller molecule and complexes, providing representation in the nanosecond to second time regime. The sample is not stacks in a matrix but it is in solution, allowing a better characterization of loose structures that could have been not crystalized. It uses different physical principle, measuring the distances between atomic nuclei, rather than the electron density in a molecule. In NMR, a strong high frequency magnetic field is applied to stimulate atomic nuclei that have a magnetic spin, and it measures the frequency of the magnetic field of the atomic nuclei during their oscillation period back to the initial state. For proteins, NMR usually measures the spin of protons. High concentration of solubilized protein is required (Wuthrich, 1986).

Especially for molecular complexes that cannot be crystalized, electron cryomicroscopy (cryo-EM, or cryo-electron microscopy) is a valuable alternative (Chiu, 1993). This technique is a combination of transmission electron microscopy (TEM) and cryo-equipment. The cryo-EM technique provides a way to observe the structure in solution, by freezing the samples extremely fast in a layer of vitreous ice. Freezing reduces electron damage, allowing a higher dose of electron exposure to gain better signal-to-noise ratio (SNR) in images. It has been widely used in the investigation of tertiary or quaternary structure of big molecular complexes but due to its nature it provide representations of a static conformations, without any relevant insight into the dynamic (Milne et al., 2013).

In last decades, atomic force microscopy (AFM)-based single molecule force spectroscopy (SMFS) technique (see below) has emerged into a reliable technique for protein structural and functional biology. It provides a direct mechanically interaction with target molecules and offers the possibility of in real time measurements of samples, in teir near like-physiological environment. Moreover, as a single molecule technique, in contrast with the majority of the "conventional" approaches, it allow to probe one molecule at a time, unveiling possibly those rare events that are usually averaged in data distribution from big populations of molecules.

Chapter 2

Atomic Force Microscopy

2.1 Scanning Probe Microscopy

In 1986 Gerd Binning and Heinrich Rohrer were awarded the Noble prize in Physics for the invention of the Scanning Tunnelling Microscope (STM) and the ambition of single atoms imaging and manipulation was finally achieved (Binnig et al., 1982a; Binnig et al., 1982b). STM was the first example of the so-called Scanning Probe Microscopy (SPM), in which the common functional principle is based on a sharp probe moved to interact with a given surface, making possible to obtain a mapping of a large variety of chemical and physical properties of the sample, including topography, fiction, stiffness, adhesion, charge and others. However, since STM's functional principle relies specifically on tunnel currents acting between the scanning probe and the surface, a major drawback in this technique was the restricted application field due to the requirement of conductive samples. This limitation was shattered in 1986 with the development of a STM variation named Atomic Force Microscopy (AFM), which utilizes forces arising between single atoms to detect the properties of the surfaces (Binnig et al., 1986). This different approach allowed probing both nonconductive and conductive surfaces in air and in liquid. AFM leaded to a new variety of biomedical application; imaging at molecular level and resolution beyond the light diffraction limit became possible, even in biologic samples, but the real breakthrough was the possibility of measure native sample in their native state and in their physiological condition (Drake et al., 1989; Bustamante et al., 1997). Afterwards, to satisfy application in material science, electromagnetism, chemistry and others, different SPM based variation have been implemented, such as Friction Force Microscopy (FFM) (Mate et al., 1987; Marti et al., 1990), Scanning Electrostatic Force Microscopy (SEFM) (Stern et al., 1988), Magnetic Force Microscpoy (MFM) (Martin and Wickramasinghe, 1987), Scanning Near Field Optical Microscopy (SNOM) (Betzig et al., 1991; Betzig et al., 1992), Scanning Kelvin Probe Microscopy (SKPM) (Nonnenmacher et al., 1991; DeVecchio and Bhushan, 1998) and others (Williams and Wickramasinghe, 1990; Hansma et al., 1989).

2.2 AFM setup

The versatility and the large variety of possible application, without particular restriction in sample choice or preparation, make the AFM the most diffuse SPM technique. As suggested by the name the technique is based on the detection of the forces acting between the probe and the sample. The probe consists in a sharp tip mounted at the end of a flexible cantilever that bends in the function of the properties of the surface (Binnig et al., 1986). This approach can be idealized as a blind person reading Brail, in which the finger that interacts with the protrusions pattern *"feeling"* the surface rather than *"seeing"* it. AFM system can be simplified as a combination of three main elements: (i) the cantilever, (ii) the piezoelectric actuator (iii) the optic detection system. All of them are strictly imbricated and modulated by a complex computer-controlled system of loops and feedbacks (Figure 2.1).

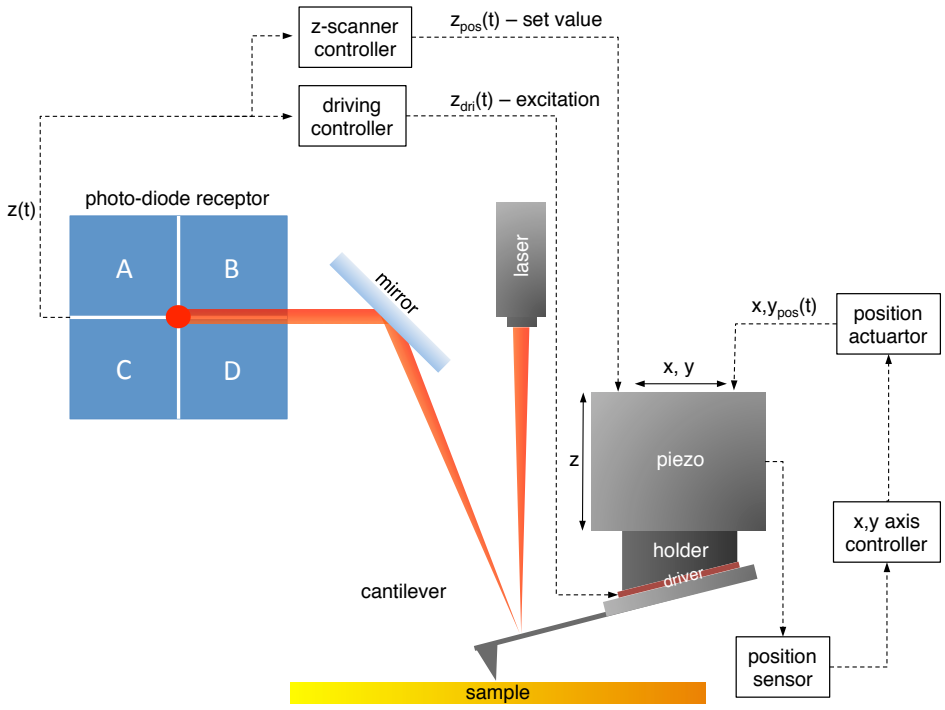

Figure 2.1. AFM setup.

2.2.1 The cantilever

The cantilever is the proper sensor that, directly interacting with the surfaces through a sharp tip, determines the quality of the signal acquired by the AFM. Cantilevers may exist in different shape, dimension and material, accordingly to their designed application. Modern and commonly used cantilevers are made of silicon, silicon-nitride (Si_3N_4) or diamond, and usually present a rectangular or

triangular shape (Akamine et al., 1990; Wolter et al., 1991; Tortonese et al., 1993) (Figure 2.2 a and b). In addiction to the morphological characteristics, the specificity and the applications of a cantilever are also defined by a combination of mechanical properties (i.e the horizontal, lateral and torsional spring constant, the resonance frequency, the quality factor and the reflectivity). The horizontal spring constant or stiffness, that usually ranges between 10^{-2} to 10^{2} N/m (depending on the modality of scanning required), defines the capability of the cantilever to properly deflect in response to the small forces acting between the tip and the surface. It can be assumed that the cantilever behaves like a Hookean spring, so that its bending can be converted into a force F by using the Hook's law:

$$F = k \cdot dx \tag{2.1}$$

where k is the spring constant of the cantilever and dx is the measure of its deflection. Usually, the spring constant is provided by the manufacturer, and strictly depends on the geometrical properties of the cantilever itself (length, width and thickness) and the material of fabrication (Young's modulus). For instance, the theoretical spring constant of a rectangular cantilever can be calculated as follow:

$$k = \frac{E\varrho^3 w}{4l^3} \tag{2.2}$$

where E is the Young's modulus, ϱ is the thickness, w is the width and l is the length of the cantilever (Yeh et al., 2006). However, this procedure assumes that materials used in the cantilever production are stable and extremely reproducible. Usually, for each cantilever in every experimental session an independent calibration is essential. Different calibration procedures have been developed (Sader et al., 1995), such as measuring the static deflection in response to a given force (Senden and Ducker, 1994; Torii et al., 1996), or measuring changes in dynamical properties of vibrating cantilevers (Hutter and Bechhoefer, 1993; Cleveland et al., 1993; Sader et al., 1995). Equally relevant mechanical property of cantilevers is the lateral spring constant or lateral stiffness, that determines the magnitude of the lateral deflection in topography measurement (an higher lateral spring constant minimize the error and usually increasing the lateral resolution). The torsional spring constant (highly depending on the length and mechanical features of the cantilever), became important in friction measurement in lateral direction. The resonant frequency (in the order of tenth of kHz) and the quality factor affect the imaging bandwidth and determine the AFM resolution especially in non-contact mode. The goodness of the reflectivity of the cantilever becomes relevant for optical detection system (see below). Finally, the shape and the radius of curvature of the tip dramatically affect the interaction with the sample and determining the resolution of the acquired signal.

The most common cantilevers for conventional measurement have a pyramidal-shaped tip (with 3 or 4 walls) under an angle of 35 degree and are about 4 μm

high, with a radius of curvature in a range between 20 and 50 nm (Figure 2.2 (c)). Usually, for imaging thinner tip are required. For artificial and regular substrates imaging many technique can be used to obtain sharper a apex on the tip, for instance focusing an ion beam to grow a thin filament on the tip of conventional cantilevers or directly attaching to the tip Single Wall Nano-Tube (SWNT) or Multi Wall Nano-Tube (MWNT) (Cheung et al., 2000; Wilson and Macpherson, 2009) (Figure 2.2 (d)). Biological samples normally have more variable roughness, whit big protrusions and they are usually stickier than artificial surfaces. That makes difficult using too much sharp and fragile tips and normally the resolution can't be push beyond the molecular level. For quantitative measurements of forces, spherical apex cantilever can be used (Figure 2.2 (e)). The diameter of these spheres may range from 10 to even 100 μm.

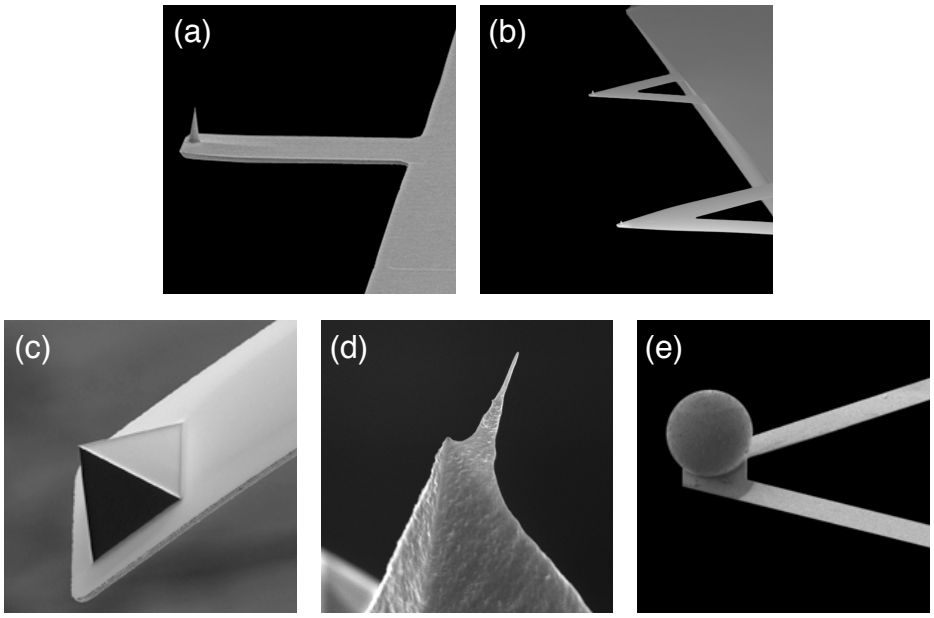

Figure 2.2. Cantilevers types. (a) rectangular cantilever, (b) triangular cantilever, (c) pyramidal shaped tip, (d) Single Wall Nano-Tube (SWNT) cantilever, (e) spherical apex cantilever.

2.2.2 The piezo actuator

Precise lateral x, y and vertical z displacements of the probe respect to the sample (or vice versa, accordingly to the set up configuration), are achieved by a computer-controlled piezo actuator (Binnig and Smith, 1986; Chen, 1992). The cantilever holder is fixed to the piezo actuator, normally tilted 15-20 degrees in order to have the cantilever and the tip protruding thought the sample. The movement of the piezo is exerted by applying a voltage, equal in amplitude but opposite in sign, at opposing quadrant of the element. As a piezoelectric material, the electric field applied make the crystal structure of the element expands

in one direction and contracts in the other. An analog system manages the controlled movement of the piezo along the z axe. The bending effect of the element is assumed as a linear function of the field's amplitude. However, the piezo element may exert non-linearity and hysteresis, becoming more significant with the increasing of the scanning area (displacement to volts ratio is smaller for small electric field magnitudes). Computer controlled closed loop with position measurement and feedback control have been implemented to avoid these inaccuracies. Moreover, for *dynamic* measurement (see below), in witch the cantilever is driven close to its resonant frequencies, an additional piezoelectric element is required as driver for shaking the cantilever an maintain its vibrational amplitude (Napoli et al., 2003). In liquid, due to the higher viscosity of the medium, *dynamic* measurements are usually more critical. Waves produced by the oscillation of the cantilever spread in the medium and can be reflected by the sample, significantly affecting the measurements. Different solutions have been develop to minimize this vibrational disturb, such as piezoelectric bi-morph cantilever (Huang et al., 2004), acoustic driver and electromagnetic driver (Han et al., 1996).

2.2.3 The optical beam detection system

The deflection of the cantilever exerts by the interaction with the sample, is measured by a laser beam focused on the reflecting back of the cantilever and reflected off to a photodiode detector (Alexander et al., 1989; Neubauer et al., 1990). Any change in the angle of reflection of the cantilever's back produces a displacement in the beam position on the photo-diode receptor, and due to the macroscopic distance from which it receives the reflected light path, any microscopic deflection produces a magnified displacement of the laser spot on the photo-diode receptor. The photo diode receptor is normally divided in four quadrants A, B, C and D (Figure 2.1), and considering I_{A}, I_{B}, I_{C} and I_{D} the output of current for each of them, three main signal can be simultaneously measured:

- The so-called *Sum* signal:

$$Sum = I_{\mathrm{A}} + I_{\mathrm{B}} + I_{\mathrm{C}} + I_{\mathrm{D}} \tag{2.3}$$

  corresponding to the voltage in output for the maximized reflection of the cantilever.

- The *vertical deflection* z signal, corresponding to a normal force F_{N} deflecting the cantilever, so that:

$$F_{\mathrm{N}} = z \cdot dx = \frac{(I_{\mathrm{A}} + I_{\mathrm{B}}) - (I_{\mathrm{C}} + I_{\mathrm{D}})}{I_{\mathrm{A}} + I_{\mathrm{B}} + I_{\mathrm{C}} + I_{\mathrm{D}}} \tag{2.4}$$

  where $z \cdot dx$ corresponds to the *Hook's law* (2.1).

- The *torsional deflection* (z_{yT}) signal, that corresponds to a lateral force F_L twisting the cantilever, so that:

$$F_L = z_{yT} \cdot k_{yT} = \frac{(I_A + I_C) - (I_B + I_D)}{I_A + I_B + I_C + I_D} \tag{2.5}$$

  where k_{yT} is the cantilever torsional spring constant. Its contribution is relevant only operating in *contact mode* (se below).

2.3 AFM operational mode

When the probe is driven in a raster-scanned mode (in x-y direction), the vertical deflection value is used in AFM imaging to produce topographical reconstruction of the sample. Instead, when the probe is moved along z axe AFM can be used to obtain a measure of the force acting between the tip and the sample.

2.3.1 Topographic reconstruction

Topographic reconstructions in AFM consist in a rendering of the informational profile acquired through the cantilever deflection, line by line, in a lateral sample scanning along x, y axes. Three operational modes have been established and are commonly used for topological reconstruction images with AFM: the so-called *contact mode*, *non-contact mode* and *tapping mode*^{TM}.

- *Contact (static) mode* consists in sampling the surface in the *"blind's finger-like"* manner. The tip is continuously kept in touch with the surface, and the topography reviled is the direct measure of the deflection of the cantilever due to the strong repulsive forces acting between the tip and the surface. In contact mode atomic resolution is possible especially on artificial surfaces both in air and in liquid. It is not commonly used for biological or irregular surfaces because, due to the frictional forces exert during the raster-scanned movement, deformation or damages both of the tip and the sample may occur (Figure 2.3).

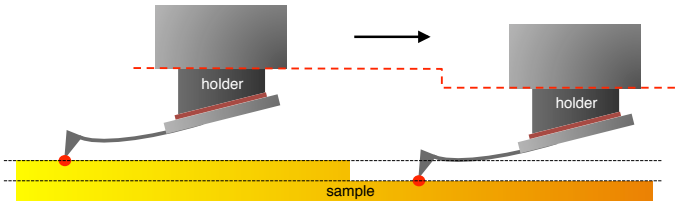

Figure 2.3. Contact mode.

- *Non-contact (dynamic) mode* the cantilever is brought in proximity of the surface and driven close to its resonant frequencies with a determined vibration amplitude (less than 100 nm) and phase. Attractive long distance interaction forces and repulsive short distance interaction forces affect the cantilever oscillation. Variation in frequency, amplitude and phase can be used as distinct channel for obtaining specific information regarding the surface (Figure 2.4).

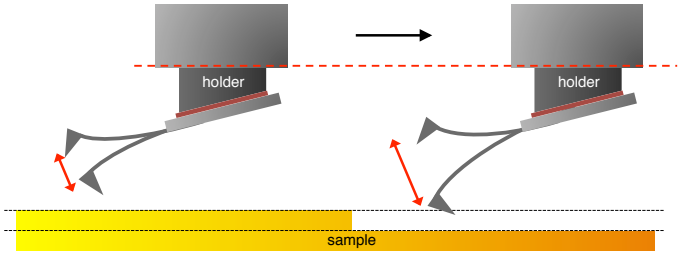

Figure 2.4. Non-contact mode.

- *Tapping mode*^{TM} (patented by Veeco) the cantilever is driven at a frequency close to the first resonant frequency with a constant amplitude and brought in proximity of the surfaces so that it touches the sample only at its maximum deflection. This modality is a sort of combination of the previous two; nonetheless due to the short time of direct contact with the surface can be considered a non-contact mode. The so-called set point value of the amplitude can be manually chose, modulating the intensity of the contact between the tip and the sample. This mode represents the more versatile solution for biological imaging and topographic measurements (Figure 2.5).

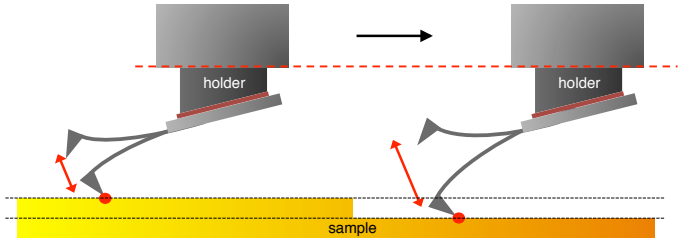

Figure 2.5. Tapping mode.

2.3.2 Force versus displacement curves

As mention before the piezo actuator can be controlled also along z direction and the interaction between the tip and the surface can be measured in terms of forces. This approach is commonly used to provide information regarding mechanical properties of the sample (stiffness or adhesive forces) or to investigate

the nature of the interaction exerted by the sample itself onto the tip. A typical AFM *force versus displacement* (F-d) curve is depicted in Figure 2.6. It describes the variation in the *vertical deflection* signal along the so-called *approach and retract cycle* (a/r cycle) in terms of forces acting between the tip and sample.

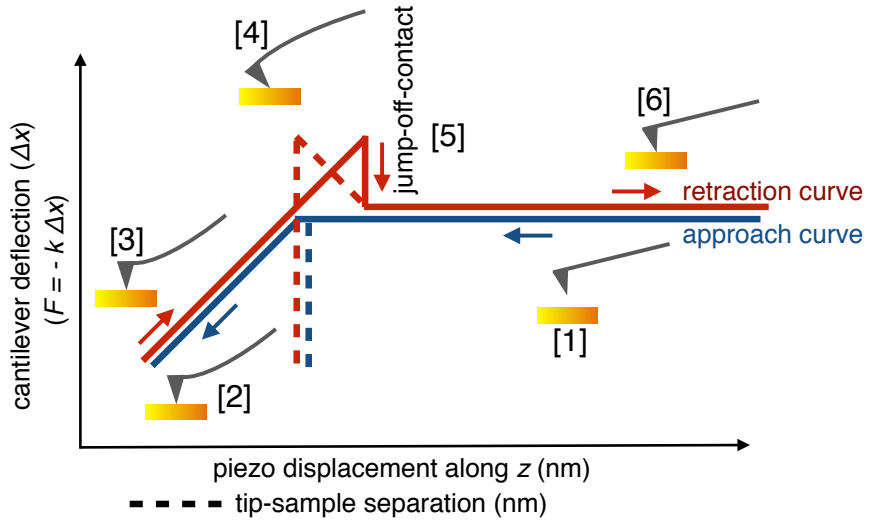

Figure 2.6. Typical F-d curve along an a/r cycle.

At the beginning the cantilever is far away from the surface and any significant interaction can be measured. Fluctuations in the deflecting signal may be caused just by the thermal noise [1]. As the cantilever is driven in proximity of the surfaces, long-range forces may start affecting the cantilever. In case of attractive forces, like van der Waals and electrostatic, a bending of the cantilever toward the sample will be recorded. On the contrary, if the acting electrostatic forces are repulsive the cantilever will be banded away from the sample. The piezo along this phase of "approach" is continuously extended toward the sample until the tip gets into contact with the surface. During the last phase of the approach, even if the tip is still quite far from the surface, attractive forces may cause the so-called "jump-to-contact", in which the contact between the tip and surfaces happens earlier than the expected time. This phenomenon limits the range of information or may even causes the damage of the tip or the sample. In these cases, a more gentle contact can be mange by controlling ionic concentration in the solution, making electrolytes screening these interaction causing the jump-to-contact (Muller and Engel, 1997). Once in contact with the surface, the probe will be banded upward by an increasing repulsive force exerted by the electron orbitals of the atoms in the probe and the sample will begin to overlap [2]. In this region of the force curve,

properly called "contact region", information regarding mechanical properties of the sample may be obtained in function of the deformation both of the tip and the sample. Afterwards, as a preset value of loading is reached, the piezo stars the "retract phase" moving the tip away from the surface and the cantilever began to relax toward its resting state [3]. During the detachment of the tip from the surfaces other interaction may be measured, adhesion forces, hydrophobic forces or solvation forces [4]. When the piezo drives away the cantilever so that its bending exert a sufficiently high force to overcame the adhesion forces, the so called jump-off-contact occur [5]. After that the cantilever escapes all the influence of the surface and relaxes to the resting position, far away form the sample and concluding in this way the a/r cycle [6] (Zlatanova et al., 2000). As described before by using Hooke's law (2.1), the cantilever deflection is converted into force and plotted versus the tip-sample separation (TSS) distance recording by the piezo displacement. The actual tip-sample distance is the difference between the piezo z displacement and the deflection of the cantilever (Figure 2.7). At zero force, the value of TSS coincides with the piezo displacement, whereas the maximum difference is reached for the maximum force value (Heinz and Hoh, 1999; Cappella and Dietler, 1999).

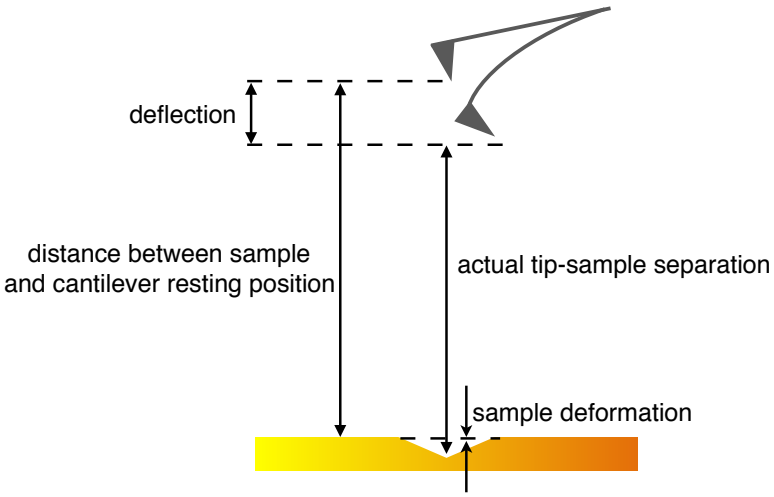

Figure 2.7. Tip sample separation and piezo displacement.

Chapter 3

Single Molecule Force Spectroscopy

In the last decades has emerged as fundamental the role of forces in the comprehension of a number of biological phenomena. So far, different techniques have been developed to probe and measure forces driving these processes within the molecular realm. In parallel, improvements in single molecule manipulation approaches raised in a repertoire of powerful and versatile nano-applications and techniques, including optical tweezers, magnetic tweezers, atomic force microscopy, micro-needle manipulation, biomembrane force probe, flow induced stretching and others (Gosse and Croquette, 2002; Cluzel et al., 1996; Kishino and Yanagida, 1988; Evans et al., 1995; Kim et al., 2007). A typical AFM based single molecule force spectroscopy (SMFS) experiment relies on stretching a molecule or a complex of molecules to measure the mechanical resistance of the their interaction and the intermolecular forces exerted. It was initially introduced in characterization of receptor-ligand bonds dynamic (Moy et al., 1994; Lee et al., 1994), but rapidly this approach turned out as a valuable tool for the characterization of the unfolding process and the mechanical stability of proteins ad macromolecules (Engel and Gaub, 2008; Harris and Booth, 2012; Kedrov et al., 2007). This application offers allows to obtain description of the unfolding forces of biomolecules and observe possible intermediates in chemical reactions. The main advantage of the SMFS is its possibility to separate the properties of individual molecules from the ensemble average behaviour observed in traditional in bulk biochemical techniques. Moreover the direct and mechanical interaction and manipulation of the sample permit to investigate proteins and organic macromolecules in their native condition as well as in their physiological environment.

3.1 Unfolding thermodynamic

As already described in Chapter 1, the native conformation of a protein represent a Gibbs free-energy minimum and a variation in Gibbs free energy ΔG for an alteration in the protein-solvent system, results in a combination of changes in enthalpy ΔH and entropy ΔS. For an ideal system at constant pressure and

constant temperature the variation in ΔG can be calculated as follow:

$$\Delta G = \Delta H - T\Delta S \tag{3.1}$$

and it can be used to determine whether a reaction is favorable or unfavorable to occur. Among the protein heterogeneity and regardless of the folding mechanism, two separated groups of protein can be considered. The first one includes two-state proteins that fold without intermediates from the folded F configuration to the unfolded U state. The second group includes muti-state proteins that fold via multiple intermediates. According to the Bell-Evans model the unfolding process from F to U can be simplified as a two state model in which the protein exists in the folded low-energy, low entropic conformation, separated from an unfolded high-energy, entropic state by an energy barrier (‡), the so-called transition state (TS) (Figure 3.1 a) (Evans, 1998; Bell, 1978; Baldwin and Rose, 1999a; Baldwin and Rose, 1999b). Two-state proteins have to cross a single TS, whereas multi-state proteins have to cross more than one. Thermodynamically the difference in free energy between the unfolded U and folded F state define the stability of a protein so that the unfolding process can be considered as governed by the unfolding rate k_0, defined as follow:

$$k_0 = {\tau_D}^{-1} exp\left(-\frac{\Delta {G_0}^{\ddagger}}{k_B T}\right) \tag{3.2}$$

where τ_D is the relaxation time and $\Delta {G_0}^{\ddagger}$ is the height of the transition state and represent the activation energy for the process. Accordingly with the equation 3.2 the unfolding rate increases when $\Delta {G_0}^{\ddagger}$ is decreased. An external applied unfolding force F leads to a change in the energy landscape as follow:

$$\Delta G^{\ddagger}(F) = \Delta {G_0}^{\ddagger} - F x_\beta \tag{3.3}$$

Where x_β is the length along the reaction coordinates and it is defined as:

$$x_\beta = x_u cos(\theta) \tag{3.4}$$

where x_u is the distance between folded and the transition state along the reaction coordinate and θ is the angle of the externally applied force relative to the reaction coordinate. The application of an external unfolding force F, results in a mechanical unfolding potential (-$Fcos(\theta)x_u$), which tilts the energy landscape as depicted in Figure 3.1 b, resulting in a decrease of $\Delta {G_0}^{\ddagger}$. For single molecule force experiments it can be assumed that θ is small, so that it can be considered $x_\beta \approx x_u$. Therefore, the unfolding rate under an externally applied force F is given by:

$$k_F = {\tau_D}^{-1} exp\left(-\frac{\Delta {G_0}^{\ddagger} - F_x}{k_B T}\right) \tag{3.5}$$

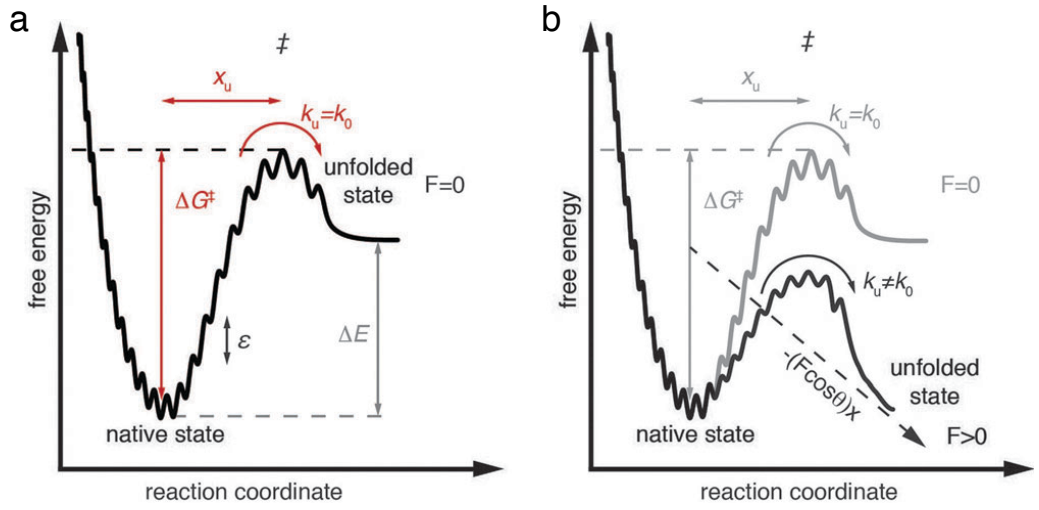

Figure 3.1. (The Bell-Evans model characterizes a folded structure by a two-state model (a). The folded structure resides into an energy valley, separated by an energy barrier from the unfolded state. The transition state (‡) of the barrier has to be overcome to induce unfolding of the folded structure. An external force F changes the thermal probability of reaching the top of the energy barrier. The energy profile along the reaction coordinate (pulling direction of the AFM cantilever) is tilted by the mechanical energy ($-Fcos(\theta)x$), (dashed line). θ describes the angle of the externally applied force relative to the reaction coordinate (b). As a result of this tilt, the energy barrier that separates the folded from the unfolded state decreases and the probability of the folded structural segment to unfold increases (Zocher et al., 2013).

The transition rate across the energy barrier and the force required to break an interaction both depend on the rate and duration of the applied force (Evans, 2001; Evans and Ritchie, 1997). The most probable unfolding force F^* depends on the most probable loading rate r_f^* , which is the slope of a force peak multiplied by the speed of unfolding:

$$F^* = \frac{k_B T}{x_u} ln \left(\frac{x_u r_f^*}{k_B T k_0} \right) \tag{3.6}$$

In general, AFM-based SMFS does not allow to perform experiments under equilibrium conditions. Nevertheless, parameters that describe the untilted energy landscape at equilibrium, such as x_u, k_0 and $\Delta G_0^‡$ can be obtained. To evaluate these parameters, is required to measure the most probable unfolding force F^* of a rupture event at different loading rates using dynamic force spectroscopy (DFS). The data obtained from these DFS unfolding experiments can be fitted using the equation 3.6. The ground-to-transition state distance x_u can be obtained from the slope of the DFS fit (F^* vs $ln(r_f^*)$). The height of the activation energy

barrier $\Delta G_0^{\ddagger}$ can be calculated using an the Arrhenius equation:

$$\Delta G^{\ddagger}(0) = -k_B T ln(\tau_D k_0) \tag{3.7}$$

The two state energy landscape illustrated in is an oversimplification, since the structures of soluble and membrane proteins are stabilized by weak non-covalent interactions, for example ionic bonds, hydrogen bonds and van-der-Waals interactions. These interactions break when the protein is transferred from the native state into the completely stretched and unfolded state. Thus, a large number of energy barriers have to be overcome during the folding or unfolding of a protein, which results in a rough energy landscape (Figure 3.1). Therefore, in typical DFS experiments l only the most prominent energy barriers can be identified and quntified, while minor energy barriers might not be detected.

3.2 Force-extension protein unfolding

In a typical SMFS experiment of unfolding, a single molecule is attached between the tip and sample. The piezo is moved away from the surface and the molecule undergoes a mechanical stretch (Figure 3.2 a step 1). During the extension of the molecule, as the distance between the tip and substrate increases, a restoring force generated by folded domains causes the cantilever deflection. The folded domain resists to the stretch until the pulling force applied by the displacement of the piezo and the banding of the cantilever reaches a sufficiently high value to overcome the kinetic barrier of the transition state (breaking force value) (Figure 3.2 a step 2 and 4) . That causes the mechanical unraveling of the folded structure and the cantilever relaxes to its resting position in the so-called jump to zero (Figure 3.2 a step 3), until a new folded segment start exerting a restoring force (Figure 3.2 a step 4).The deflection of the cantilever is recorded by the displacement of the laser on the photoreceptor and converted in force, and it is plotted versus the piezo displacement, generating a typical F-d curve displaying a so-called saw-tooth pattern, in which each peak represents an unfolding event (Figure 3.2 b).

In addition to force measurements, information regarding the the structure and the length of folded structures can be obtained. The increasing part of a force peak describes a semi-flexible polymer chains under stretch (Bustamante et al., 1994; Marko and Siggia, 1995), and can be fitted by using the worm like chain model (WLC):

$$F = \frac{k_b T}{p}\left[\frac{x}{L_c} + \frac{1}{4}\left(1 - \frac{x}{L_c}\right)^{-2} - \frac{1}{4}\right] \tag{3.8}$$

where k_b is the Boltzmann constant and T is the absolute temperature. p is the persistence length value, and it is related to the polymer unit and it is considered between 0.3 nm and 0.5 nm, which is approximately the length of a peptide bond.

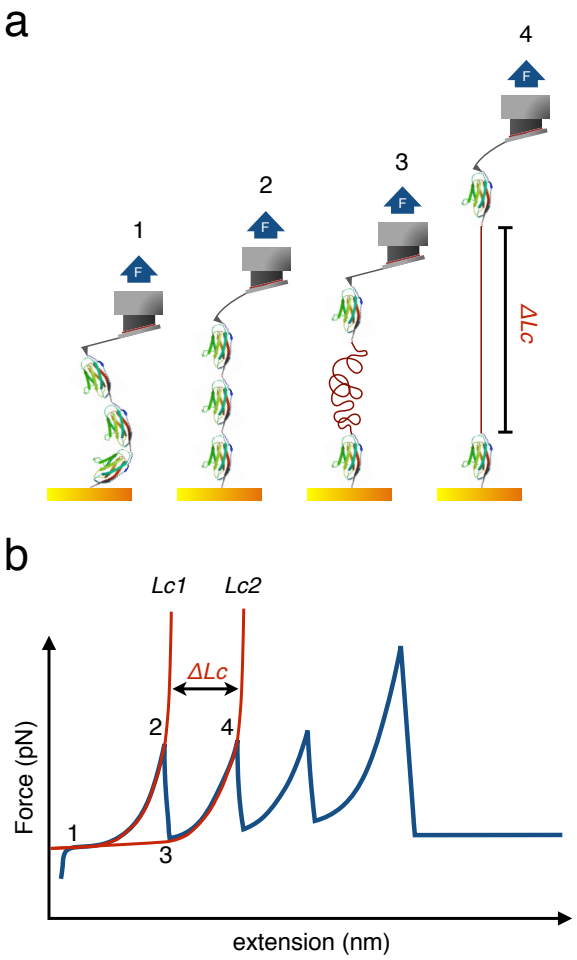

Figure 3.2. Example of SMFS experiment on multi-modular globular protein (a) and typical f-D curve fitted with the WLC model

As the F value is measured by the AFM, the equation can be solved in terms of the contour length (L_c) values, that is the length of the stretched polypeptide. Thus, measuring the ΔLc value between two consecutive forces peaks, the length of the structure that had been unfolded can be calculated, and dividing this value by 0.4 (average length of a single amino acid residue in nm) the number of residues composing the the unfolded structure can be evaluated (Carrion-Vazquez et al., 2000) (Figure 3.2).

Chapter 4

Hyperpolarization-activated and Cyclic Nucleotide-gated (HCN) Channel

4.1 Structure and Function

Hyperpolarization-activated and Cyclic Nucleotide-gated (HCN) channels belong to the superfamily of voltage gated pore loop cation channels, and together with Cyclic Nucleotide-gated Channel (CNG) and Eag-like K^+ channels form the subgroup of the cyclic nucleotide-regulated cation channels (Wahl-Schott and Biel, 2009; Biel et al., 2002; Biel and Michalakis, 2009). HCN channels are primarily involved in the generation and modulation of the rhythmic activity in cardiac pacemaker cells and neuronal network spontaneous firing. They are also claimed to be responsible for the determination of the resting membrane potential, dendritic integration and synaptic transmission (Wahl-Schott and Biel, 2009). HCN channels mediate a depolarizing mixed K^+ and Na^+ current, named I_{h} (hyperpolarization-activated current) or I_{f} (*funny current*), which in contrast with usual voltage gated ion channels, is activated when the membrane voltage is driven towards negative voltages below -50 mV (DiFrancesco and Tortora, 1991; DiFrancesco, 2010; Mannikko et al., 2002; Wainger et al., 2001). Moreover, the voltage dependence of HCN channels is regulated by the direct binding of cyclic nucleotides to a cytosolic C-terminal cyclic nucleotide binding domain (CNBD), inducing a rightward shift in the voltage-dependence activation of the channel (DiFrancesco and Tortora, 1991 Wainger et al., 2001). HCN channels have been cloned from vertebrates and several invertebrates but are missing in *C. elegans*, yeast and prokaryotes. (Ludwig et al., 1998; Santoro et al., 1998; Ishii et al., 1999; Gauss et al., 1998; Marx et al., 1999). Four different isoforms (HCN1-HCN4) have been identified in mammals, differing in the activation kinetics and in their response to the cAMP. In heterologous system of expression, the kinetic exhibited in homotetrameric HCN1 is fast, intermediate in HCN2, and slow in HCN3 and HCN4 (Postea and Biel, 2011). Moreover, HCN2 and HCN4 are strongly responsive to the cyclic adenosine monophosphate (cAMP), showing a shifting in the

activation curve of about +15 mV, and HCN1 and HCN3 are weakly modulated by the cAMP. Evidence suggest etero-tetrameric complexes are also possible in vivo (Much et al., 2003; Chen et al., 2001; Altomare et al., 2003). HCN channels share architectural similarities with other pore loop channels. Each subunit forming the tetramer is composed by a transmembrane core, including six α-helices (S1-S6), with the ionic selectivity filter in the loop between S5 and S6, and a voltage sensor domain positively charged within the S4 helix.

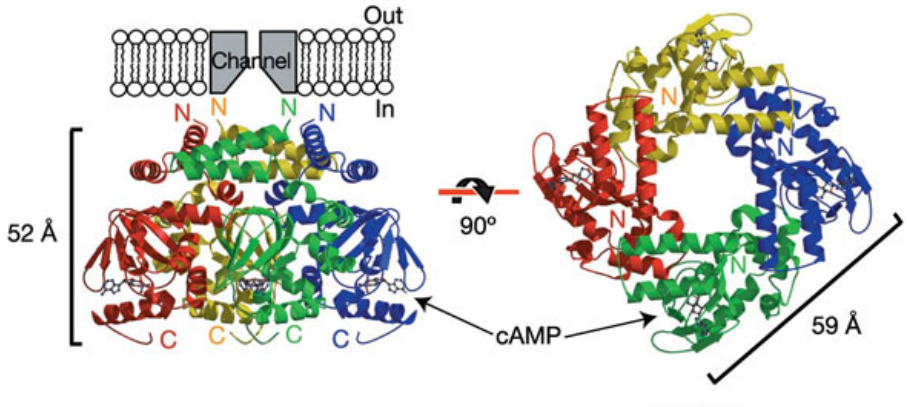

Figure 4.1. HCN channel structure (Zagotta et al., 2003).

The sensitivity of HCN channels to cyclic nucleotide is mediated by the proximal portion of the cytosolic C-terminus. The 80 amino acids long c-linker comprises six α-helices (A'-F') and connect the S6 transmembrane domain the 120 amino acids long CNBD, composed by three α-helices (A-C) and eight β-strands (1-8) forming a β-roll between helices A and B **??** (Zagotta et al., 2003).

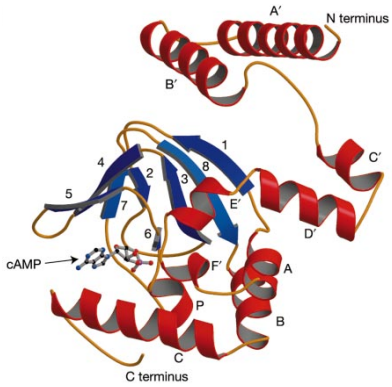

Figure 4.2. Ribbon representation of the C-linker + CNBD structure in the presence of the cAMP. (Zagotta et al., 2003).

Residues corresponding to the β-roll and the C-helix form the binding pocket for cAMP. Four C-linker-CNBDs are assembled together, forming a complex with

a fourfold axis of symmetry consistent with the tetrameric architecture of the transmembrane core. The majority of the inter-subunit interaction are though to be medeiated by amino acid residues in the C-linker (Zhou and Siegelbaum, 2007; Flynn et al., 2007; Zagotta et al., 2003). Recent model suggest in the absence of cAMP the C-linker exhibit a more compact conformation, so that it may exerts an inhibitory effect on the channel opening. Moreover, binding of cAMP are thought to induce changes in folding of C-helix in the CNBD and F' helix in the C-linker. These conformational changes lead to a more loose structural arrangement in the c-linker, affecting the inter-subunit interface between helices of neighboring subunit. The resulting change in the quaternary conformation remove the inhibition of the C-linker, destabilizing the close state and promoting the opening of the channel (Craven and Zagotta, 2004; Taraska et al., 2009; Saponaro et al., 2014). Despite continuous improvement in techniques and new insight into the comprehension of HCN channel's behavior, the molecular mechanism underling the cAMP dependent modification in the c-linker and CNBD and its extent in the regulation of the channel permeability remains not fully understood.

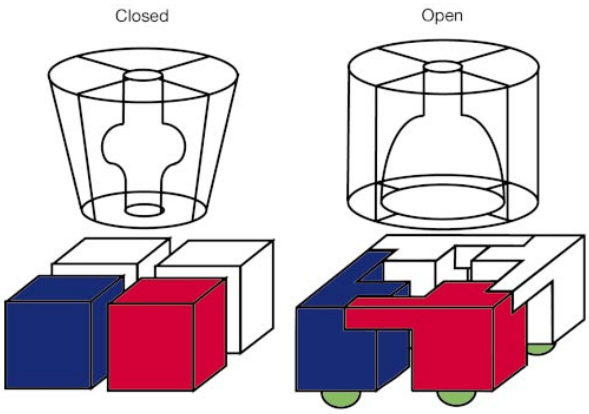

Figure 4.3. Model of cAMP dependent regulation of HCN channel (Zagotta et al., 2003)

Chapter 5

Results

In this section are presented papers in preparation and publications in witch I was involved in during my PhD.

The first work presented concern the investigation of the unfolding behaviour of the purified cytosolic c-linker and CNBD construct by using single molecule force spectroscopy technique. It is the result of several contributions carried out by different people. For what concerns me, I performed all the SMFS experiments and corresponding data analysis. I actively participated in developing of the analytical procedure, in designing and writing this work. The paper is still in preparation.

The second work presented enclosed the methodological work carried out in developing informatic tools for automatic analytic procedure. It present an open-source platform for F-d curves analysis. For what concerns me, I participated in the design and validation of algorithm. A trial version of the software and a dataset are available at this link:
https://www.dropbox.com/sh/jlswyq1r1sgmw6q/AAB4xCY_ZQ9vlZ89lEvLUl5Va?dl=0.
This work is in preparation as a Correspondence in Nature Methods.

The last two work presented do not directly concern with my PhD project but are the results of two collaborations with professor Enrico Cherubini, carried out during the first and the second year of my PhD.

hHCN2 cytoplasmic domain unfolds in a three- and four-state fashion in the presence of cAMP, but not in the absence

Andrea Pedroni[1], Nicola Galvanetto[2], Andrea Alfieri[2], Andrea Perissinotto[1], Anna Moroni[2], and Vincnet Torre[1,*]

[1]Neuroscience Area, Scuola Internazionale Superiore di Studi Avanzati (SISSA), 34136 Trieste, Italy
[2]Department of Biosciences, Universitá degli Studi di Milano, 20133 Milano, Italy
[*]torre@sissa.it

ABSTRACT

During folding and unfolding, complex proteins sample multiple pathways in which different intermediate states are visited. The experimental determination of these intermediate states is a necessary step to unravel the dynamics of the folding/unfolding process. Here we investigate the mechanical unfolding of the C-terminal cytosolic domain of the hHCN2 channel in the presence and in the absence of the cAMP. Our results reveal ligand-depended differences in the unfolding events. In 65% of the traces in the presence of the cAMP we observed a three-state (20%) and four-state (45%) like unfolding. On the contrary, the molecule in the absence of the ligand do not present any defined unfolding pathways but the recurrence of a conserved intermediate suggest an independent and sequential unfolding of the c-linker first and the CNBD than.

Introduction

It is still an open question whether proteins fold into their native state via one single pathway or through multiple distinct pathways (Onuchic et al., 1997; Dill and Chan, 1997; Dill and MacCallum, 2012). Several theoretical studies predict a kinetic partitioning mechanism along a funnel-shaped energy landscape, in which proteins are driven to their Gibbs free energy minimum (native state) via multiple (un)folding trajectories (Baldwin, 1995; Thirumalai et al., 1997; Englander and Mayne, 2014). However, an experimental determination of these multiple trajectories is so far limited (Zaidi et al., 1997; Wright et al., 2003). Single molecule techniques have revealed the stochastic nature of the (un)folding process, and have been applied primarily to globular proteins (Borgia et al., 2008; Neuman and Nagy, 2008) and occasionally to more complex proteins (Peng and Li, 2008; Kotamarthi et al., 2013). Here we used atomic force microscopy (AFM) based single molecule force spectroscopy (SMFS) to investigate the mechanical unfolding of the purified cytoplasmic domain from the human hyperpolarization-activated and cyclic nucleotide-gated (hHCN)2 channel. HCN channels belong to the family of the cyclic nucleotide-regulated cation channels (Wahl-Schott and Biel, 2009; Biel et al., 2002; Biel and Michalakis, 2009). They are primarily involved in the generation and modulation of the rhythmicity in cardiac pacemaker cells and neuronal network spontaneous firing (Wahl-Schott and Biel, 2009; Postea and Biel, 2011). The voltage dependence gating of HCN channels is regulated by the direct bind of cyclic nucleotides to the cytosolic c-terminal cyclic nucleotide binding domain (CNBD). The CNBD is composed by three α-helices (A-C) and eight β-strands (1-8) forming a β-roll between helices A and B, and connected to the transmembrane core of the channel by a c-linker region comprising six α-helices (A'-F') (Fig. 1 A and C). This construct has been widely studied and the crystal structure has been solved in the presence of the ligand (Zagotta et al., 2003). The

purified c-linker and CNBD domain represent an intriguing model to investigate the mechanical unfolding of complex proteins, and the cAMP dependent structural modification of the construct offers a unique system for probing differences in the unfolding behaviour between the apo and holo configuration. Our results provided evidence of ligand-dependent differences in the unfolding of the molecule. In the presence of the cAMP the construct unfolds predominantly in a three-state (20%) or four-state-like (45%) fashion, through conserved unfolding intermediate states. Conversely, in the absence of the ligand the c-linker and CNBD seem to unfold independently following diverse unfolding pathways.

Results

Construct functionalization and incubation

A histidine tag was added at the C-terminus to promote the successful interaction between the nitrilotriacetic acid (NTA) functionalized cantilever (Verbelen et al., 2007; Li et al., 2002; Watanabe et al., 2002) and the protein. Two cysteines were added to the N-terminus to promote the formation of a covalent bond with the gold surface, over which the molecule was deposited before SMFS measurements (Grandbois et al., 1999) (Fig. 1A and B). The stability of the functionalized construct was verified by dynamic light scattering (DLS) measurement and similar behaviour with the WT construct was assessed (data not shown). The protein was incubated on the gold surface for ≈20 minutes at a concentration of 0.5 mg/mL at room temperature as described in Materials and Methods. The efficiency of the incubation procedure was controlled at different concentrations and nanografting measurements were performed to verify the efficiency of the binding between the molecule and the surface (data non shown). Forces versus displacement curves were recorded at a constant speed of 250 nm s^{-1}, by using cantilevers with a declared spring constant of 0.084 Nm^{-1}. Measurements were performed both in the absence and in the presence of 2 mM of cAMP (Fig 1B).

Traces filtering and validation

Both in the presence and in the absence of the cAMP, the majority of the F-d curves came from unsuccessful interactions between the tip and the protein (i.e. empty traces, incomplete unfolding, multimolecule and unspecific adhesion). We developed an automatic procedure to filter F-d curves, based on the following steps: firstly, all the traces with a detachment corresponding to the theoretically length of the fully unfolded protein were selected. The construct comprises 215 amino acid, hence the detachment is expected at a Lc value of ≈ 86 nm (215 aa x 0.4 nm/aa) (Carrion-Vazquez et al., 2000). In this step short (possibly not complete unfolding or unspecific interaction) and long traces (multimolecule or disordered interaction) are discarded. In our SMFS experiments only 0.2-0.8% of collected traces passed this initial filtering step satisfying the ”full-length” condition. Secondly, we removed F-d curves with unspecific adhesion events present at values of the tip sample separation (TSS) larger than 20 nm. The final filtering step retained only F-d curves that were properly with the worm like chain (WLC) model (Materials and Methods). At the end of these filtering steps, 205 F-d curves in the absence of cAMP and 271 F-d curves in the presence of cAMP were obtained (Materials and Methods). These traces were automatically aligned by using a free-reference alignment methods (Bosshart et al., 2012) (Matherials and Methods), and their superimpositions are shown as a density plot in Fig. 2A and B, in the absence and presence of cAMP respectively. Visual inspection of individual traces (Fig. 2C and D) indicates that in the presence of cAMP F-d curves have less force peaks and occurring at more regular values of TSS. The density plots in Fig. 2A and B revealed that force peaks occur within values of Lc in the same range. Each force peak of every trace was fitted with the WLC model and the corresponding Lc values were counted within a binwidth of 1.2 nm (consistent with the length of three amino acid residues) and displayed in histograms (Fig. 3A

and B). Ensemble of peaks were fitted with Gaussian Mixture Model (GMM) (Kawamura et al., 2013) (Materials and Methods) and 8 peaks in the absence and 7 in the presence of cAMP were identified (see Table 1). The last peak represents the detachment and falls at 86.6 $\pm$ 3.0 nm in the absence of cAMP and at 86.3 $\pm$ 3.8 in the presence. After the detachment peak, in the absence of cAMP the most conserved group of events appears at 49.4 nm (peak IV) with a probability of occurrence of 57%. Less conserved group of events are observed before ad after with peak I, II and III at 12.9, 21.9 and 38.7 nm in the 48, 31 and 35% of the trace respectively, and peak V, VI and VII at 60.8, 69.0 and 77.6 nm in the 41, 42 and 39% of the traces. In the presence of the cAMP the most conserved peak falls at 73.0 nm with 64% of occurrence. Less conserved groups of events appear in peaks I, II, III, IV and VI, observed at 14.0, 22.1, 29.9 42.0 and 58.0 nm in 51, 46, 43, 41 and 35% of the traces respectively. Over all traces in the presence of cAMP reveal group of peaks more ordered around certain Lc values. Events in the absence of cAMP appear to be less conserved especially in the range between 20 and 40 nm.

C-linker + CNBD construct unfolding occurs via multiple pathways both in the absence and in the presence of cAMP

In order to identify the unfolding pathways we developed an algorithm, providing clusters of F-d curves with force peaks located at similar values of Lc. We divided the Lc histograms in n intervals, partitioning the Lc coordinates in regions with distinct maxima (Fig. 3A and B). The end points of these intervals (I1,I2,...,I5) corresponded to relative minima of these histograms. In order to reduce the number of clusters we set the value of n equal to 5, slightly less than number of distinct peaks in the histograms. Having partitioned in this way the TSS axis, each F-d curve is coded in a string of 5 digits, with 1 indicating that a force peak occurred in the ith-interval. Having coded F-d traces in these simple binary sequences, its straight forward to find clusters with the same digital coding which are good candidates of distinct unfolding pathways. In Fig. 3C and D each cluster is represented with a broken line with a width proportional to the number of F-D traces present in that cluster and with nodes corresponding to the interval of occurrence of the observed force peak. In the absence of cAMP F-d traces follow 11 main different paths, each of them with less than two dozens of traces. In contrast, F-d traces in the presence of cAMP are grouped in two major paths (the yellow path with 55 traces and the blue path with 53 traces) and additional 4 minor groups with a number of traces ranging between 20 and 27. In the absence of cAMP unfolding force peaks occurred homogeneously in each interval (the percentage ranging between 43 and 64%, see Fig. 3C), whereas in the presence of cAMP 93% of the traces present at least one unfolding event falling within the first intervale, 36 and 38% within the second and third interval respectively and 58% within the forth.

Unfolding in the presence of cAMP occurs predominantly in a three- and for-state like fashion

The path plots (Fig. 3C and D) shows a remarkable difference of the unfolding behaviour in the absence and presence of cAMP: in the presence of cAMP the great majority of F-d curves (65%) unfold in a three or four state like manner. the blue paths (n=53 equal to 20%), have a three-state unfolding process, with an intermediate state at 26 $\pm$ 2 nm (Fig. 4A and B). 45% of the traces in the presence of cAMP have a four-state unfolding behaviour. Three major preferred unfolding pathways were identified (yellow, purple and cyan path in Fig. 4D). The yellow path, 55 traces (20%), have the same intermediate falling at 24 $\pm$ 3 nm and an additional intermediate at 74 $\pm$ 2 nm. The purple path (24 traces, 9%) and cyan path (27 traces, 10%) have a four state like unfolding with a similar intermediate at 23 $\pm$ 3 nm but different intermediate states at 55 $\pm$ 2 and 43 $\pm$ 4 nm respectively (Fig. 4F and E). The recurrence of the first intermediate suggest how crossing this first kinetic barrier laying close to the folded state, is a necessary condition

to access to further different unfolding pathways, regardless to the three- or four-state behaviour. The remaining traces (35%) have a less conserved pathway. Among these two major conserved groups (17%) are presented in SI as possible candidates for multi-states unfolding pathways, nonetheless the variability in the unfolding forces and the positions of evens make not straight forward interpreting the unfolding behaviour, reflecting the intrinsic diversity of more complex unfolding schemes (Materials and Methods).

Unfolding in the absence of cAMP does not occur via conserved pathway

In the absence of cAMP two main different unfolding behaviours were observed: 35% of the traces have a common intermediate state falling at 48 $\pm$ 2 nm (Fig. 5A). Among these, 25 traces (orange group in Fig. 5A) do not have any additional conserved force peaks, while 24 traces (green broken line in Fig. 5B) present an early intermediate at 13 $\pm$ 3 nm and a conserved force peak at 48 $\pm$ 2 nm, underlying the thermodynamic stability of this intermediate. After that some more conserved force peaks appear but there is not well defined unfolding route defined from conserved intermediate. Several traces have an initial flat region with a variable length and force peaks at 39 $\pm$ 2, 53 $\pm$ 2 and 71 $\pm$ 4 nm (Fig. 5D, E and F). The remaining traces (30%) appear to spread into different groups, poorly conserved in number of traces and in peak positions.

Discussion

How complex proteins (un)fold remain one of the most challenging open question in structure biology. Despite numerous contributions in theoretical prediction, experimental counterpart remains difficult to achieve. In the present manuscript we investigated the mechanical unfolding of the c-linker + CNBD construct from hHCN2 channel both in the presence and in the absence of the cAMP. We developed novel approach to handle the intrinsic stochasticity of the process and provided evidences of strong cAMP depended modifications in unfolding behaviour. A large variety of unfolding pathways has been revealed especially in the absence of the cAMP. Conversely, conserved unfolding pathways in the presence of the cAMP suggest a more defined mechanical stability of the construct in the holo configuration respect to the apo one. In the light of the solved structure in the presence of the cAMP (Zagotta et al., 2003) we measured the ΔLc values between consecutive intermediate to assign the structural meaning to the elongation of the molecule accordingly to the theoretical number of amino acid residues composing each folded structure. In the presence of the cAMP, from the analysis of the candidate unfolding pathways occurring both via a three-state and four-state like manner, a conserved intermediate is seen at 25 $\pm$ 2 nm (Fig. 4B, E, G and I). This intermediate force peak could be interpreted as the unfolding of the short α-helices (C' + D' + E' +F') of the c-linker region (fig. 4C). Thus, the ΔLc value of 60 $\pm$ 4 nm is consistent with the expected elongation of the residual A' + B' helices in the c-linker and of the whole CNBD (Fig. 4C). In the four-state like unfolding behaviour we identify three different unfolding pathways, each of them characterized by a different second intermediate. In the first one (Fig. 4E), the ΔLc1 value of 50 $\pm$ 5 nm measured between the first and the second intermediate can be interpreted with the unfolding of all the structures of the protein except for the two final couples of β-sheets, composed by 29 aa for a theoretical length of $\approx$ 12 nm (Fig. 4F). In the second unfolding pathway (Fig. 4G and H) the force peak at 55 $\pm$ 2 nm can be interpreted as the unfolding of all the α-helices (composed by 81 aa, for a theoretical elongation of $\approx$ 33 nm), followed by the opening of the β-roll, composed by 75 aa, equivalent to $\approx$ 30 nm (Fig 4H). In the third pathway the force peak at 43 $\pm$ 4 nm (Fig. 4I an L) suggests a discrete unfolding of the c-linker in two steps, followed by the complete unfolding in a single step of the whole CNBD (Fig. 4L). In the absence of the cAMP the recurrence of the intermediate falling at 48 $\pm$ 2 nm, possibly suggests a discrete unfolding of the c-linker firstly and the CNBD then. Thus, the ΔLc value of 39 $\pm$ 6 nm

is consistent with the complete unfolding of the CNBD minus the C helix (Fig. 5B and C). The groups of traces presenting flat regions variable in length and conserved ensembles of event falling between 39 $\pm$ 2 and 71 $\pm$ 4 nm can be interpreted as the sequential unfolding of residual structure belonging to the CNBD (Fig 5E, F and G), whereas the c-linker region do not show any unfolding intermediates. A not defined independent unfolding of the CNBD respect to the c-linker in the presence of the cAMP can be interpreted as continuum in the mechanical stability along the whole molecule (see three-state like unfolding behaviour). On the other hand, this behaviour may be also related with a rapid loss of affinity of the molecule to the cAMP and a consequent loss of the structure of the binding pocket of the CNBD. In the absence of the cAMP the conserved intermediate at 48 $\pm$ 2 nm suggests an independent mechanical stability of the CNBD respect to the c-linker. The higher variability in the unfolding behaviour of the molecule in the absence of the ligand suggests a lower degree of stable folding but could also be related with a structural variability in the "native" states of the protein. Our results highlight the complex nature of the unfolding behaviour of the c-linker + CNBD domain from the hHCN2 channel, nonetheless the procedure we developed allowed an exploration of the variety of the diverse unfolding pathway. Moreover, we provided some insights regarding how the mechanical stability of the construct, in the presence and in the absence of cAMP, may affect the cyclic nucleotide dependent modulation of the channel permeability.

Materials and Methods

Purified and functionalized c-linker + CNBD construct

In order to obtain a human HCN2 construct amenable to derivatization for immobilization on the mica substrate, a multi-step cloning procedure was engineered (Supplementary Information).

AFM setup and cantilever functionalization

The NanoWizard 3 AFM system (JPK) and an inverted optical microscope (Olympus IX71) were used. All the experiments were performed in liquid condition using Standard solution (containing in mM 110 KCl, 10 HEPES and 0.2 EDTA; pH 7.4 buffered with KOH), with or without 2 mM cAMP. Rectangular silicon nitrite gold-coated cantilevers (HYDRA2R-50NGG from APPNANO) were functionalized and were used to perform SMFS experiments. The declared cantilever spring constant was 0.08 N m^{-1} and each tip was calibrated before the initiation of each experiment by using the equipartition theorem. Tips were initially cleaned in ethanol for 15 min, dried under an N_2 flow and exposed to ultraviolet light for 15 min. Tips were further incubated for 5 min in chloroform and dried again under a N_2 flow. These three steps were repeated two times. Cantilever tip functionalization was based on the thiol and nitrilotriacetic acid-Ni^{2+} (Verbelen et al., 2007). Cleaned cantilevers were incubated for 30 min in 10 mM dithiobis-C2-NTA (Dojingo Technologies, Japan), washed with ethanol and dried in a N_2 flow. The tips were then incubated for 20 min in 100 mM $NiSO_4$ and rinsed with MilliQ water before being dried in a N_2 flow. Finally, the functionalized tips were incubated for 20 min in 10 mM 6-mercapto-1-hexanol to avoid nonspecific adsorption and were dried again under a N_2 flow. Salts and reagents were purchased from Sigma-Aldrich. Cantilever functionalization and activity of NTA was checked performing control SMFS experiment on a polypeptide chain composed of eight modules of I27. The pulling efficiency was almost 10%, but in presence of 50, 100 and 200 mM imidazole the efficiency decreased to 1%, 0.5% and 0%, respectively (Data not shown).

SMFS measurements and data acquisition

The purified c-linker + CNBD construct, both in the absence and in the presence of the cAMP was incubated on the gold surfaces at a concentration of 0.5 mg/mL, at room temperature, for $\approx$ 20 minutes in

Standard solution (containing in mM 110 KCl, 10 HEPES and 0.2 EDTA; pH 7.4 buffered with KOH). After the incubation the surface was gentle washed several times to remove not strongly attached molecules and depositions. AFM imaging in tapping mode was performed to check the goodness of surface and identify a suitable area for SMFS measurements. Using the matrix-scanning mode, the AFM tip was repeatedly pushed into the surface along a defined area (usually 1μm square). The contact force was set at 1 nN and the delay time before the retraction was 0.5 s, to give the protein a chance to be adsorbed on the tip. The tip was retracted at a constant speed of 250 nm s^{-1} and the force exerted between the tip and surface was recorded. Hundred of thousands of traces were obtained in tenths of different experimental session with and without the cAMP. Collected F-d curves by the AFM JPK software were initially filtered to remove unsuitable cases. The filtering procedure was based on the analysis of the approach and retraction curves. Force offset between the retraction and extension curves was compared, and if it was greater than a given threshold related to the type of experiment in the initial part of the curve (at least 30 pN, but usually is greater), the curve was discarded. We then compared crossings between the approach and retraction curves and if the force offset between two crossings was $>$20 pN, the curve was discarded. Variance $\sigma 2$ of the extension curve was computed to estimate the motion of the baseline and if $\sigma 2$ was $>$10 pN^2, the curve was discarded. Initial slope of the extension curve (Sp) and the retraction signal (Sr) then compared and if (1 Sp/Sr) was $>$1, the curve was discarded. The maximum pulling force (F) was calculated and if F was $<$30 pN, the curve was discarded. The extension curve drift was calculated and if the maximum amplitude was $>$35 pN in the ”flat” region, the curve was discarded). Lengths of the TSS (distance or TSS) for the extension and retraction curves were compared and if the length difference was $>$10%, the curve was discarded (Maity et al., 2015).

Traces coding and filtering

First, F-d curves were converted into a plot of force and contour lengths (F, Lc) (Bosshart et al., 2012). WLC model with a persistence length (Lp) of 0.4 nm was used to compute the Lc value for each corresponding tip-sample separation (d or TSS) value, by solving the third order polynomial: $4\lambda 3 + \omega\lambda^2$ - 1 = 0, where λ = 1 - d/Lc and ω = 4F(d,LC)/α - 3 and α = kbT/Lp. This equation had three roots and the root of interest was the real root λ^* such that $0 < \lambda^* < 1$. In this manner, each point of the F-d curve (F, d) was transformed into a corresponding point (F, Lc), and each F-d curve was transformed into an (F, Lc) plot (supplementary). The three roots of the equation were obtained using a MATLAB routine. Owing to this transformation, each portion of the F-d curve that was fitted perfectly by the WLC model was mapped to a perfect vertical segment. The transformation of an F-d curve was therefore a relation (set of point) in the (F, Lc) plane rather than a function in the plane, and it was also not a continuous curve. Given a set of F-d curves, the histogram of the normalized counts/bin of Lc values (normalized histogram of Lc values) was computed. The Lc axis of the (F, Lc) plot was first divided into bins (in the range from 1 to 10 nm). All points with a value of F larger than 30 pN were counted in the corresponding bin and summed over all sets of the F-d curves, and the final histogram of counts/bin was normalized so that its maximal value was equal to 1. This histogram was used to quantify the occurrence of points in the F?D curves that correspond to a given value of Lc. Given an (F, Lc) plot, it was possible to extract an (F, Lc) profile and to compute the local maxima (Histogram of Lc values at force peaks). The Lc axis was divided into fixed intervals of 1-10 nm (typically of 3 nm). We extract the maximum value of F in each interval to obtain the corresponding (F, Lc) profile (if all values of F in an interval were below 30 pN, the value of the force in that interval was set equal to 0 pN) and the local maxima of the (F, Lc) profile were computed. In this manner, it was possible to compute the final histogram from the local maxima of the (F, Lc) profile that was normalized by the total number of F-d curves that were considered. The histogram of the local maxima were used to shows the probability of obtaining F-d curves that had a

force peak with a given value of Lc. The (F, Lc) plot of the pulling curve was computed to identify traces having at least one peak in the range between 20 and 90 nm and the detachment peak falling in the range between 75 and 95 nm. This step allows obtaining only those traces coming form the complete unfolding of the construct. Shorter traces than 75 nm (incomplete unfolding or early detachment), and longer traces than 95 nm (multimolecule interaction), were discarded. Traces with large initial non-specific adhesion (forces >190 pN in the first 20 nm) were filtered out (Fig. S4B). A quality-filtering procedure was used to evaluate the goodness of the WLC fitting for all force peak with force values over 35pN. High quality traces in contour length histogram shows highly defined columns (Fig. S4C and D). We computed the ratio between the number of bin occupied (B) and the total number of points (N) in the histogram. This ratio is interpreted as an estimator of the quality of each unfolding event.

Traces alignment

Bosshart and colleagues developed a reference free alignment method consisting of 3 main steps. Starting from the contour length histogram, they subdivided the traces into groups of homogeneous traces (i.e. traces with the same number of peaks). They recursively aligned traces into the same group with the maximum-correlation principle, building an average contour-length reference for each group. Then they computed a global reference for the alignment of the entire dataset (Bosshart et al., 2012). This procedure is suitable for membrane or identical globular multidomain proteins where force peaks generally occurred within conserved Lc values. In the case of soluble and complex proteins the occurrence of unfolding events may be variable due to the stochastic nature of the process or because of multiple distinct pathways may be accessed by the protein. For this reason, we introduced two additional features to minimize the displacement of the traces from the origin (Fig. S5) and divided traces not only on the base of the number of force peaks in the traces but also accordingly with their sequence of occurrence.

Path Plot

Intervals were defined along the TSS coordinate, in the correspondence with relative minima in the Lc histograms. Each trace was coded as string with n binary elements, to which was assigned 1 if a peak felt into the i-th interval and 0 if not. To each positive element were assigned a Pn value corresponding to the cardinal number of the corresponding interval, and an Nm value corresponding to the ordinal number of the peak within the trace. In this manner traces were divided in the function of the number of force peaks occurring within the single trace, and grouped along the single paths in the function of the sequence of the events. Considering a trace with two peaks, one within the 2nd and the other into the 5th interval, it will be coded as 0 1 0 0 1 string (Fig. S6B, C and D). For the first peak N = 1, P_n = 2 will be assigned, for the second peak N = 2, P_n = 5 will be assigned. Coded traces were plotted as segments in P_n -N space as shown in Fig. 3C and D. The plot provides a division of the traces in 2n, where n is the number of set intervals. Specifically in our case traces are divided in 2n-1 groups because the last peak (detachment) is common in all the traces. This grouping made it feasible an interpretation of an unfolding event within each group on the base of the other unfolding events characterising similar traces.

Bibliography

Baldwin, R.L. (1995). The nature of protein folding pathways: the classical versus the new view. J. Biomol. NMR 5, 103-109.

Biel, M., and Michalakis, S. (2009). Cyclic nucleotide-gated channels. Handb. Exp. Pharmacol. 111-136.

Biel, M., Schneider, A., and Wahl, C. (2002). Cardiac HCN Channels: Structure, Function, and Modulation. Trends Cardiovasc. Med. 12, 206-213.

Borgia, A., Williams, P.M., and Clarke, J. (2008). Single-molecule studies of protein folding. Annu. Rev. Biochem. 77, 101-125.

Bosshart, P.D., Frederix, P.L.T.M., and Engel, A. (2012). Reference-Free Alignment and Sorting of Single-Molecule Force Spectroscopy Data. Biophys. J. 102, 2202-2211.

Carrion-Vazquez, M., Oberhauser, A.F., Fisher, T.E., Marszalek, P.E., Li, H., and Fernandez, J.M. (2000). Mechanical design of proteins studied by single-molecule force spectroscopy and protein engineering. Prog. Biophys. Mol. Biol. 74, 63-91.

Dill, K.A., and Chan, H.S. (1997). From Levinthal to pathways to funnels. Nat. Struct. Biol. 4, 10-19.

Dill, K.A., and MacCallum, J.L. (2012). The Protein-Folding Problem, 50 Years On. Science 338, 1042-1046.

Englander, S.W., and Mayne, L. (2014). The nature of protein folding pathways. Proc. Natl. Acad. Sci. U. S. A. 111, 15873-15880.

Grandbois, M., Beyer, M., Rief, M., Clausen-Schaumann, H., and Gaub, H.E. (1999). How Strong Is a Covalent Bond? Science 283, 1727-1730.

Kawamura, S., Gerstung, M., Colozo, A.T., Helenius, J., Maeda, A., Beerenwinkel, N., Park, P.S.-H., and Müller, D.J. (2013). Kinetic, energetic, and mechanical differences between dark-state rhodopsin and opsin. Struct. Lond. Engl. 1993 21, 426-437.

Kotamarthi, H.C., Sharma, R., Narayan, S., Ray, S., and Ainavarapu, S.R.K. (2013). Multiple Unfolding Pathways of Leucine Binding Protein (LBP) Probed by Single-Molecule Force Spectroscopy (SMFS). J. Am. Chem. Soc. 135, 14768-14774.

Li, H., Linke, W.A., Oberhauser, A.F., Carrion-Vazquez, M., Kerkvliet, J.G., Lu, H., Marszalek, P.E., and Fernandez, J.M. (2002). Reverse engineering of the giant muscle protein titin. Nature 418, 998-1002.

Maity, S., Mazzolini, M., Arcangeletti, M., Valbuena, A., Fabris, P., Lazzarino, M., and Torre, V. (2015). Conformational rearrangements in the transmembrane domain of CNGA1 channels revealed by single-molecule force spectroscopy. Nat. Commun. 6, 7093.

Neuman, K.C., and Nagy, A. (2008). Single-molecule force spectroscopy: optical tweezers, magnetic tweezers and atomic force microscopy. Nat. Methods 5, 491-505.

Onuchic, J.N., Luthey-Schulten, Z., and Wolynes, P.G. (1997). Theory of protein folding: the energy landscape perspective. Annu. Rev. Phys. Chem. 48, 545-600.

Peng, Q., and Li, H. (2008). Atomic force microscopy reveals parallel mechanical unfolding pathways of T4 lysozyme: Evidence for a kinetic partitioning mechanism. Proc. Natl. Acad. Sci. 105, 1885-1890.

Postea, O., and Biel, M. (2011). Exploring HCN channels as novel drug targets. Nat. Rev. Drug Discov. 10, 903-914.

Thirumalai, D., Klimov, D.K., and Woodson, S.A. (1997). Kinetic partitioning mechanism as a unifying theme in the folding of biomolecules. Theor. Chem. Acc. 96, 14-22.

Verbelen, C., Gruber, H.J., and Dufrêne, Y.F. (2007). The NTA-His6 bond is strong enough for AFM single-molecular recognition studies. J. Mol. Recognit. JMR 20, 490-494.

Wahl-Schott, C., and Biel, M. (2009). HCN channels: structure, cellular regulation and physiological function. Cell. Mol. Life Sci. CMLS 66, 470-494.

Watanabe, K., Nair, P., Labeit, D., Kellermayer, M.S.Z., Greaser, M., Labeit, S., and Granzier, H. (2002). Molecular mechanics of cardiac titin?s PEVK and N2B spring elements. J. Biol. Chem. 277, 11549-11558.

Wright, C.F., Lindorff-Larsen, K., Randles, L.G., and Clarke, J. (2003). Parallel protein-unfolding pathways revealed and mapped. Nat. Struct. Mol. Biol. 10, 658-662.

Zagotta, W.N., Olivier, N.B., Black, K.D., Young, E.C., Olson, R., and Gouaux, E. (2003). Structural basis for modulation and agonist specificity of HCN pacemaker channels. Nature 425, 200-205.

Zaidi, F.N., Nath, U., and Udgaonkar, J.B. (1997). Multiple intermediates and transition states during protein unfolding. Nat. Struct. Mol. Biol. 4, 1016-1024.

	absence of cAMP		presence of cAMP (2mM)	
peak	**Mean ± SD (nm)**	**Probability**	**Mean ± SD (nm)**	**Probability**
I	12.9 ± 3.0	0.48	14.0 ± 4.8	0.51
II	21.9 ± 2.1	0.31	22.1 ± 2.0	0.46
III	38.7 ± 2.2	0.35	29.9 ± 2.4	0.43
IV	49.4 ± 4.5	0.57	42.0 ± 5.0	0.41
V	60.8 ± 2.2	0.41	58.0 ± 3.4	0.35
VI	69.0 ± 2.0	0.42	73.0 ± 5.8	0.64
VII	77.6 ± 2.9	0.39	86.3 ± 3.8	1
VIII	86.6 ± 3.0	1		

Table 1. Mean contour length ± standard deviation and probability of occurrence of force peak groups.

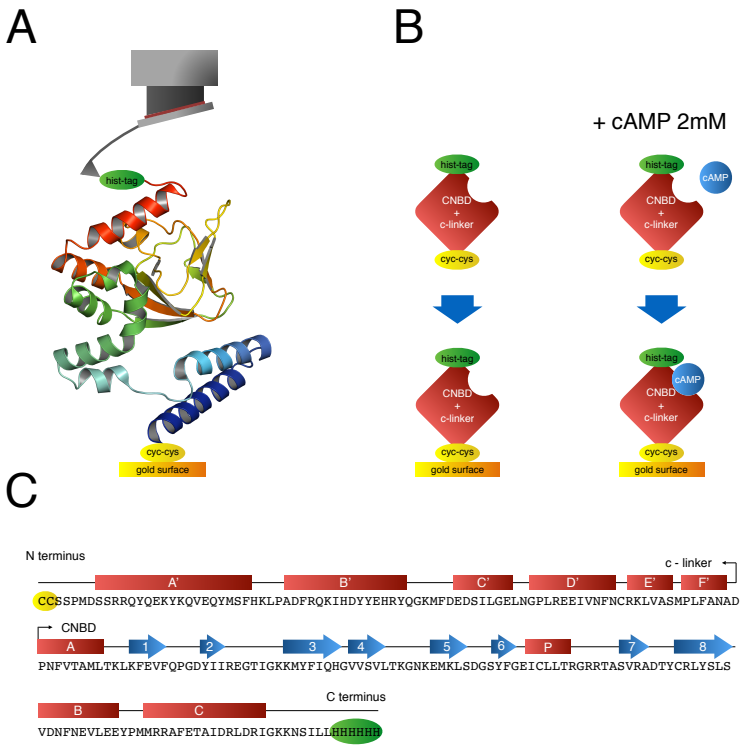

Figure 1. (A) Scheme of a SMFS experiment and ribbon representation of the purified and functionalized c-linker + CNBD construct. (B) Schematic representation of the sample preparation, with the construct bearing an His-tag at the C-terminus and two cysteine at the N-terminus. 2 mM of cAMP was added before the deposition of the protein on the gold surface for SMFS experiment in the presence of the ligand. (C) Amino acids sequence of the construct and representation of the secondary structure accordingly with the crystal structure solved in the presence of cAMP.

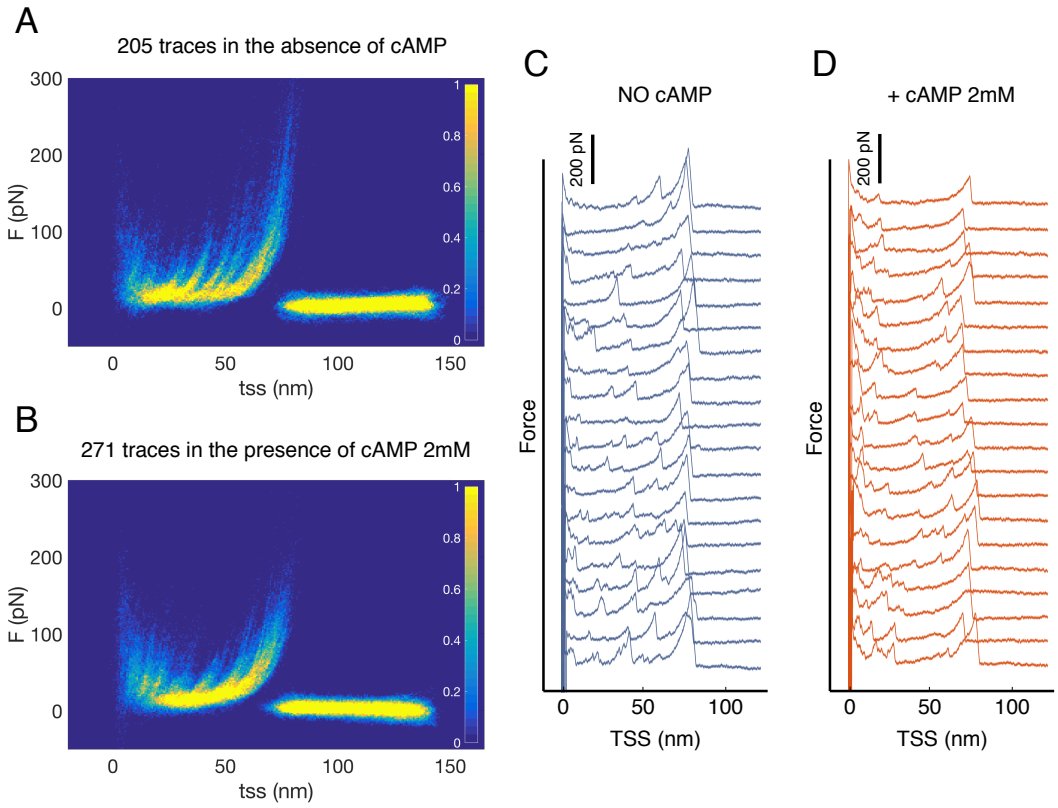

Figure 2. (A) Density plot representing valid traces obtained in the absence of cAMP (n = 205) and (B) in the presence of the cAMP (n = 271). Densification region in the density plot represent groups of unfolding events occurring around the same Lc value. (C and D) Typical examples of valid F-d curves both in the presence and in he absence of the cyclic nucleotide (n = 20).

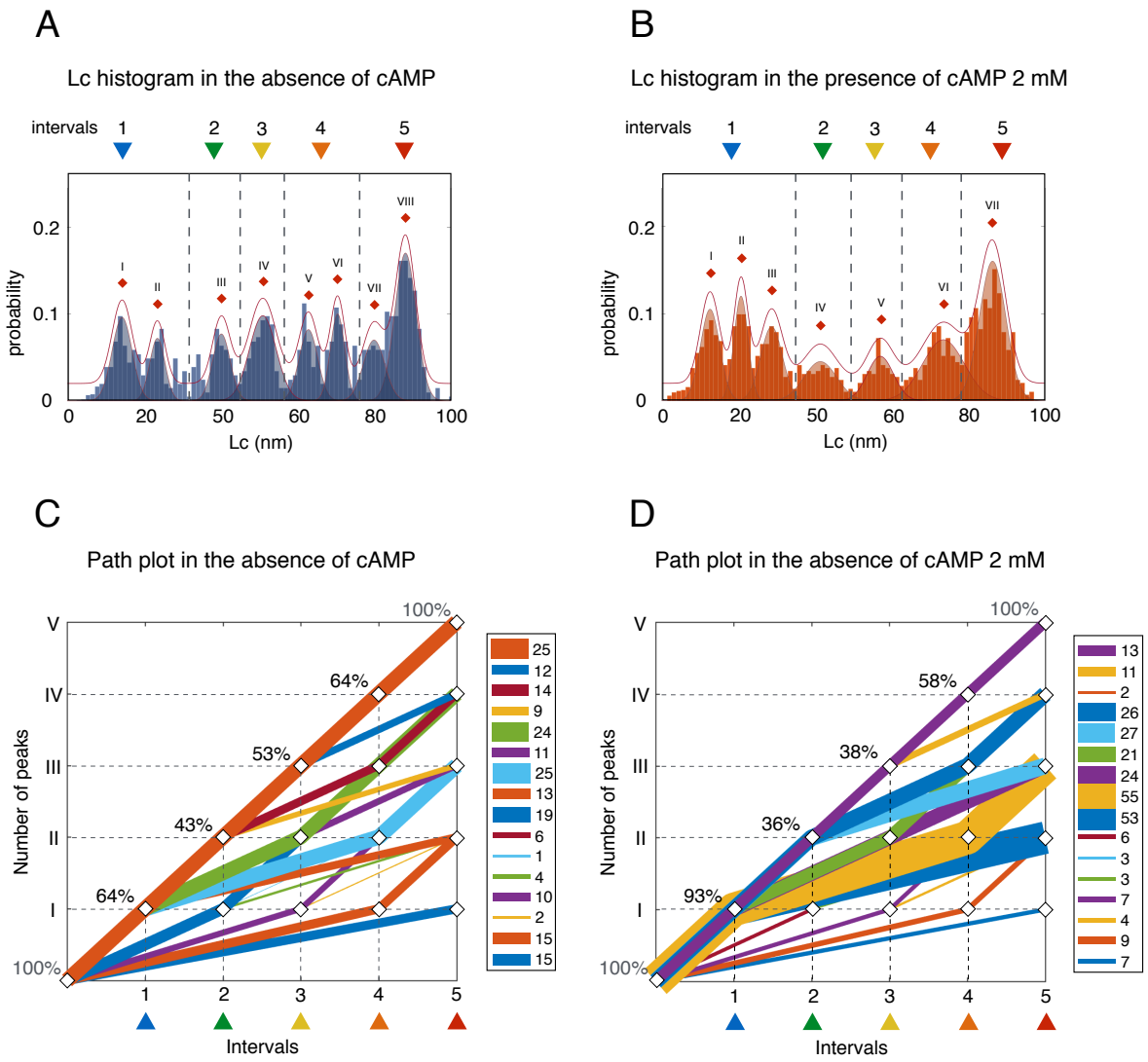

Figure 3. (A and B) Lc histograms in the absence and in the presence of cAMP display the frequency of occurrence of force peaks respect to their position in Lc. Each groups of events was fitted with the Gaussian Mixture Model and Mean Value ± Standard Deviation and corresponding probability of occurrence are reported in table 1. Lc histograms were divided in five intervals (colored triangle) in order to code traces for the path plot representation (C and D). Broken line in the path plot represent group of similar traces divided on the based of the number of force peaks and grouped accordingly to the position of occurrence of those peaks.

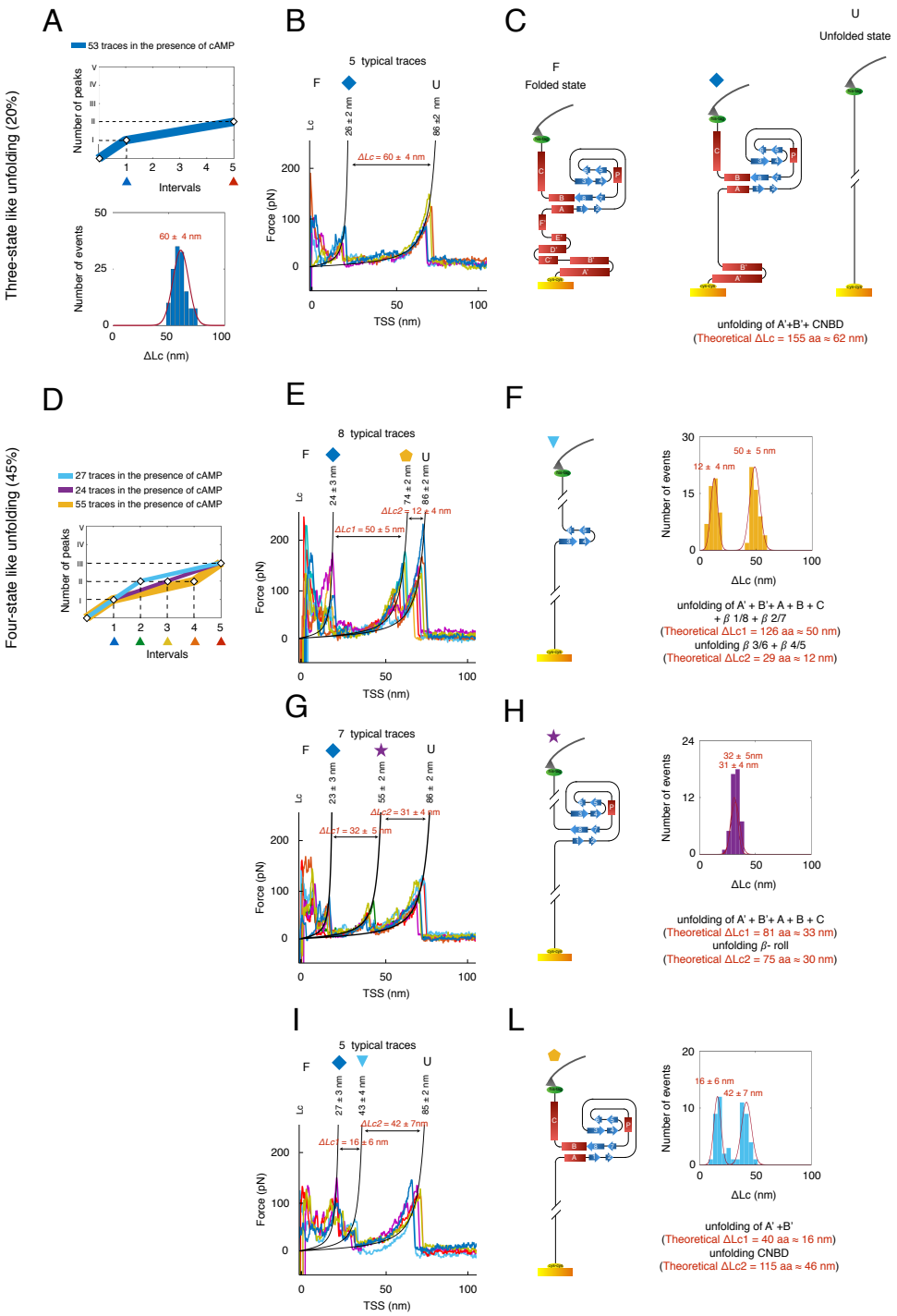

Figure 4. (A) Three-state unfolding behaviour has been observed in 20% of the traces in the presence of cAMP, emerging as the blue broken line in the path plot. Those traces present a conserved intermediate of unfolding falling at 26 ± 2nm (B). (C) possible structural interpretation fro the three-state unfolding behaviour. (D) 45% of the traces present a four-state unfolding behaviour, revealing three major conserved unfolding pathways with different intermediate unfolding states (E, G and I). (F, H and L) possible structural interpretation of the unfolding behaviour of the different unfolding pathways, accordingly with the measured ΔLc and the solved structure of the construct.

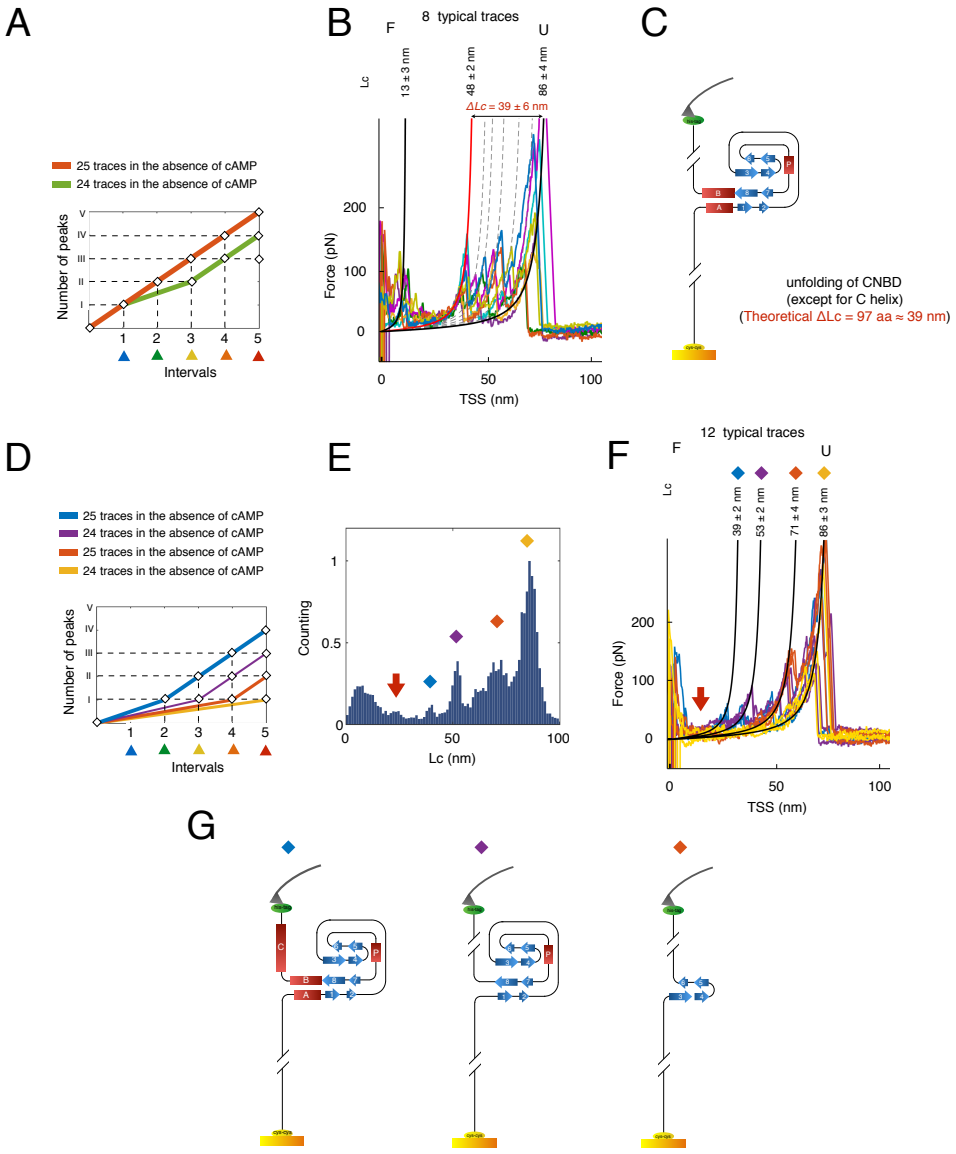

Figure 5. (A) 35% of the traces presenting a recurrent intermediate at 48 ± 2 nm. (B) Eight typical traces belonging to the green cluster in the path plot. (C) Possible structural interpretation of the intermediate at 48 ± 2 nm. (D) Groups of traces characterized by the absence of events within the first interval in the path plot. (E) Normalized Lc histogram revealing recurrent peaks and (F) typical traces extracted from the different groups. (G) Possible interpretation of the corresponding unfolding state of the molecule for each main conserved force peak.

Supplementary Information

Production of pET24bMT: HCN2_CB : H

pET24bHM3C is a modified pET-24b vector (Novagen) available in A.M.'s laboratory (University of Milano) and codifying a 6x histidine tag, a maltose binding protein tag and a human rhinovirus 3C protease cleavage site (LEVLFQ/GP, hereafter '3C') upstream of the insertion site. The DNA construct pET24bHM3C : HCN2_CB available in A.M.'s laboratory harbors a human HCN2 C-linker + cyclic nucleotide binding domain, hereafter HCN2_CB (UniProt entry Q9UL51, residues 470-672), thus encoding the construct 6H-MBP-3C-HCN2_CB (Fig. S1A). This plasmid was subjected to four sequential rounds of site-directed mutagenesis (QuikChange Site-Directed Mutagenesis Kit, Agilent Technologies). In round 1, the LEVLFQ/GP site was mutated to LEVLFQ/CC using the mutagenetic primers 5'-GGAAGTTTTGTTTCAATGTTGCAGCAGCCCCATGGACTC CTCGC-3' and its reverse complement; the obtained construct was then mutated in the second round by the primers 5'-GATGGCGGATCTTTGGAAAATTTGTACTTTCAATGTTGCAGCAG-3' and its reverse complement to obtain the ENLYFQ/CC site ('T'), which is a sub-optimal consensus for the tobacco etch virus (TEV) protease target site ENLYFQ/G (Kapust et al., 2002; Kostallas et al., 2011). In round 3, the N-terminal histidine tag of pET24bHM3C construct was removed by the primers 5'- TACATATGGGTTCTTCTG GTTCTTCTATGAAAATCG-3' and its reverse complement. Finally, in round 4, a 5x histidine tag was inserted after the C-terminal His of HCN2_CB by the primers 5'-AATTCCATCCTCCTGCACCACC ATCACCATCACTAATAAGGGTTG-3' and its reverse complement, to obtain the final plasmid pET24bMT : HCN2_CB : H encoding the construct MBP-T-HCN2_CB-5H (Fig. S1B). After removal of the MBP tag by the use of TEV protease, the construct CC-HCN2_CB-5H (where CC indicates the N-terminal double cysteine for immobilization on the mica substrate) will be generated (Fig. S1C). The DNA sequence was verified at each step and at the end of the cloning procedure.

Production of pET24bM3C : TEVp

The cDNA encoding TEV protease, hereafter TEVp (kind gift of C. Binda, University of Pavia), necessary for the production of the final construct was cloned into pET24bHM3C. One round of site-directed mutagenesis was performed to remove the N-terminal histidine tag in order to obtain pET24bM3C: TEVp encoding the construct MBP-3C-TEVp (Fig. S1D); for this purpose, the same primers described above in round 3 were exploited. The removal of the N-terminal histidine tag was intended to avoid the presence of contaminating histidine-tagged TEV protease in the final product for atomic force microscopy experiments. The final plasmid was sequence-verified.

Production and purification of protein constructs

MBP-3C-TEVp

The plasmid pET24bM3C : TEVp was transformed into competent E.coli BL21(DE3) cells. Cell cultures were grown at 37 °C in Luria-Bertani broth up to $Abs_{600nm} \approx 0.6$, induced with IPTG 0.4mM and shaken at 25°C for 20h. The cells were centrifuged and resuspended in lysis buffer (TrisCl 50mM pH 7.4, NaCl 500mM, glycerol 10%(v/v), EDTA 0.5mM) supplemented with β-mercaptoethanol 1mM, PMSF 0.1mM, pepstatin A 4μg/mL, DNaseI 10μg/mL, lysozyme 0.5mg/mL. The cell suspension was sonicated on ice and the lysate was cleared by centrifugation. The resulting supernatant was loaded onto a manually-packed amylose resin and the construct eluted by a buffer containing maltose 10mM and concentrated. Protein concentrations were monitored by spectrophotometry and SDS polyacrylamide gel electrophoresis was used to visualize the final construct MBP-3C-TEVp (Fig. S2). The protein displayed full proteolytic activity when mixed with the target construct MBP-T-HCN2_CB-5H (Fig. S3).

MBP-T-HCN2_CB-5H

The plasmid pET24bMT : HCN2_CB : H was transformed into competent E.coli Rosetta cells. Cell cultures were grown at 37 °C in Luria-Bertani broth up to $Abs_{600nm} \approx 0.6$, induced with IPTG 0.4mM and shaken at 20 °C for 20h. The cells were collected by centrifugation and resuspended in lysis buffer (TrisCl 50mM pH 7.4, NaCl 500mM, glycerol 10%(v/v), imidazole 10mM) supplemented with β-mercaptoethanol 1mM, protease inhibitor cocktail, DNaseI 10μg/mL, and lysozyme 0.5mg/mL. The cell suspension was sonicated on ice and the lysate was cleared by centrifugation. The resulting supernatant was loaded onto a nickel-charged affinity chromatography column (HiTrap IMAC HP, GE Healthcare) and the construct eluted with imidazole 300mM. The protein solution was supplemented with the previously produced MBP-3C-TEVp in a 1:10 protease: target molar ratio, additioned with DTT 10mM to ensure reducing conditions, diluted and dialyzed overnight at 4 °C. Additions of DTT 10mM were repeated along the purification to maintain reducing conditions. The following morning, the sample was checked for protease cleavage efficiency and flown through a manually-packed amylose resin to remove cleaved MBP and MBP-3C-TEV and isolate the construct CC-HCN2_CB-5H. Subsequently, a size-exclusion chromatography column (Superdex75 10/300 GL, GE Healthcare) was exploited for final cleaning. The yield was approximately 7 mg purified construct from 1L culture (Fig. S3).

Bibliography

Kostallas G, Löfdahl PÅ, Samuelson P. Substrate profiling of tobacco etch virus protease using a novel fluorescence-assisted whole-cell assay. PLoS One. 2011 Jan 18;6(1):e16136. doi: 10.1371/journal.pone.0016136. PubMed PMID:21267463; PubMed Central PMCID: PMC3022733.

Kapust RB, Tözsér J, Copeland TD, Waugh DS. The P1' specificity of tobacco etch virus protease. Biochem Biophys Res Commun. 2002 Jun 28;294(5):949-55. PubMed PMID: 12074568. The Discussion should be succinct and must not contain subheadings.

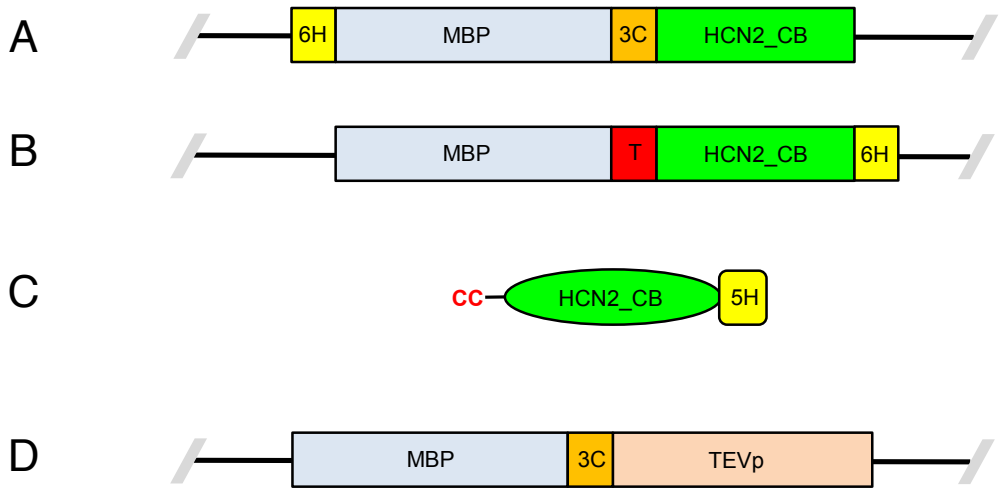

Figure 1. Supplementary. Scheme of the plasmids and the construct involved in the procedure. (A) Scheme of the initial plasmid pET24bHM3C : HCN2_CB. (B) Scheme of the final plasmid pET24bMT : HCN2_CB : H. (C) Scheme of the final protein construct CC-HCN2_CB-5H to be produced at the end of the purification. (D) Scheme of the final plasmid pET24bM3C : TEVp.

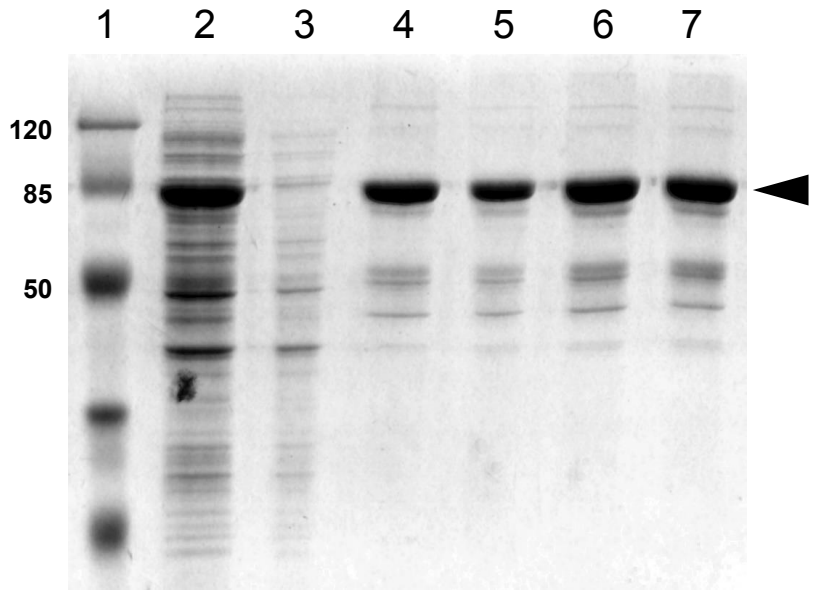

Figure 2. Supplementary. SDS-PAGE of samples MBP-3C-TEVp purification. Lane 1, molecular weight marker (kDa aside); lane 2, total cell extract; lane 3, flowthrough of amylose resin; lanes 4-7, elution fractions from amylose resin. MBP-3C-TEVp (71 kDa) is indicated by an arrow.

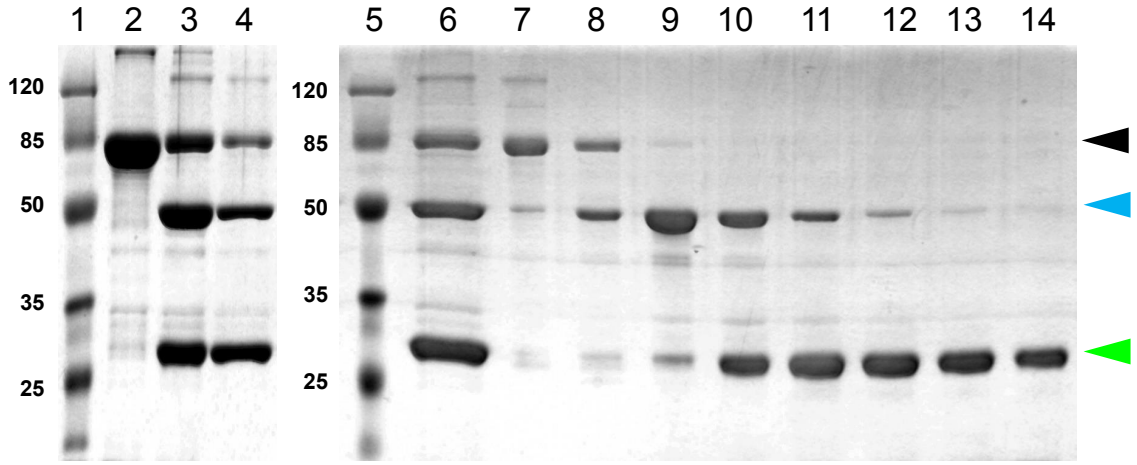

Figure 3. Supplementary. SDS-PAGE of samples from the purification of the construct MBP-T-HCN2_CB-5H. Lanes 1 and 5, molecular weight marker (kDa aside); lane 2, sample before overnight dialysis + cleavage; lane 3, sample after overnight dialysis + cleavage; lanes 4 and 6, sample eluted out of amylose resin, note the presence of contaminants; lanes 7-14, fractions of elution from the final size-exclusion chromatography. Black arrow: MBP-T-HCN2_CB-5H (69 kDa) and MBP-3C-TEVp (71 kDa); blue arrow: cleaved MBP (45 kDa); green arrow: CC-HCN2_CB-5H (25 kDa).

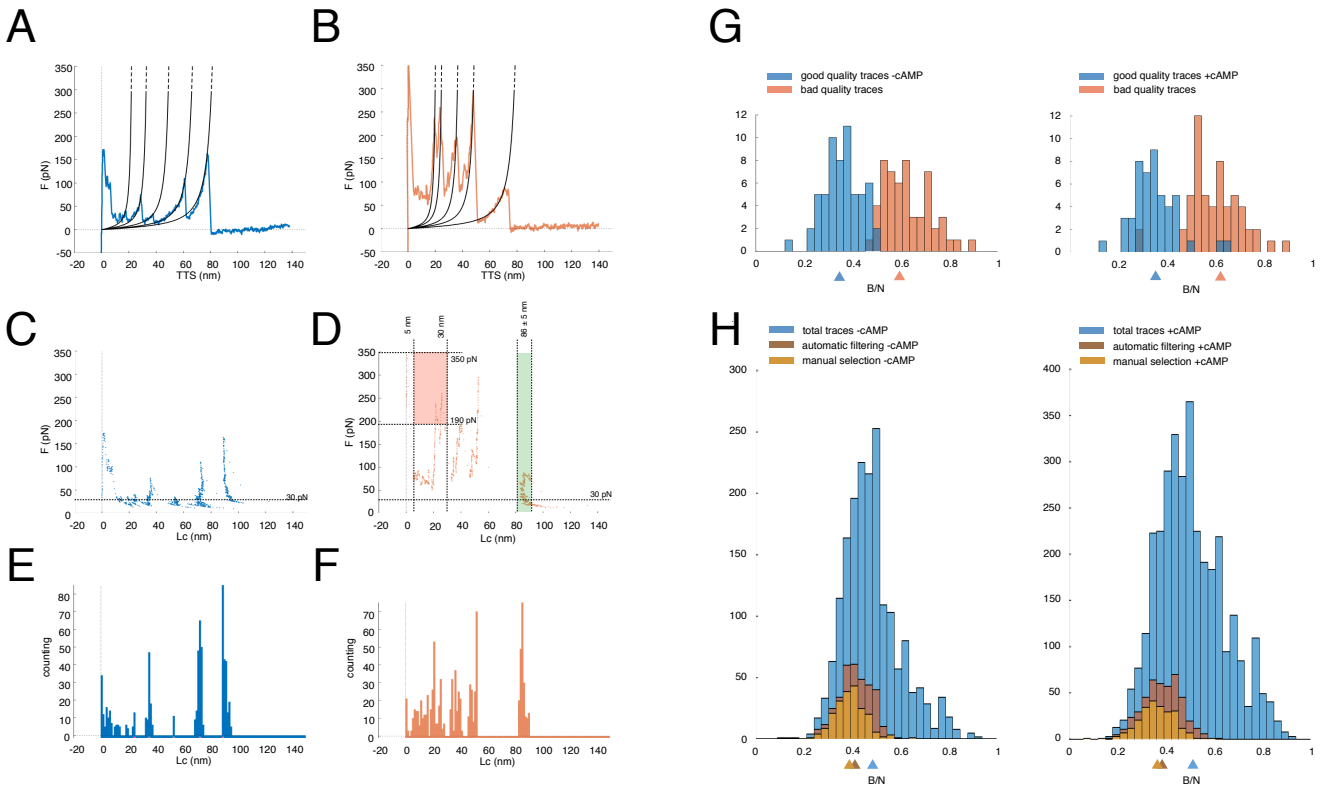

Figure 4. Supplementary. Traces were initially selected on the theoretical length of the fully stretched protein comprises 215 amino acid, so that the detachment is expected at a Lc value of ? 86 nm (215 aa x 0.4 nm/aa) This step provides the discarding of empty trace, shorter traces and longer traces. Several traces exhibit an initial huge unspecific adhesion and a window filtering procedure was developed to automatically discard those traces. (A) Example of a good quality trace (A) and a poor quality one (B). (C) Traces are transformed into an F-Lc space by solving the WLC model for each point. (D) ”Windows” were designed to evaluate the occurrence points of traces within certain values ranges of force and Lc. (E and F) represent the transformation of traces in Lc histograms to compute the B/N ratios, where B is the number of bin occupied and N is the total number of points into the histogram. (G) B/N comparison between 55 manually selected good traces and 61 manually selected bad ones in the absence of cAMP and 57 good and 59 bad in the presence. Traces selections appear clearly separated in the B/N dimension. (H) B/N ratio of 3897 traces in the absence and 3582 traces in the presence of cAMP before windows filtering procedure (light blue histograms), 616 in the absence of cAMP and 623 in the presence after the window filtering procedure (brown histograms) and the final selection of 205 traces in the absence 271 traces in the presence of cAMP after a further manual selection. Triangles along the B/N coordinate represent the mean value of the distributions. See the decrement in the B/N ratio indicating that every filtering step provided an improvement in the quality of the trace selection.

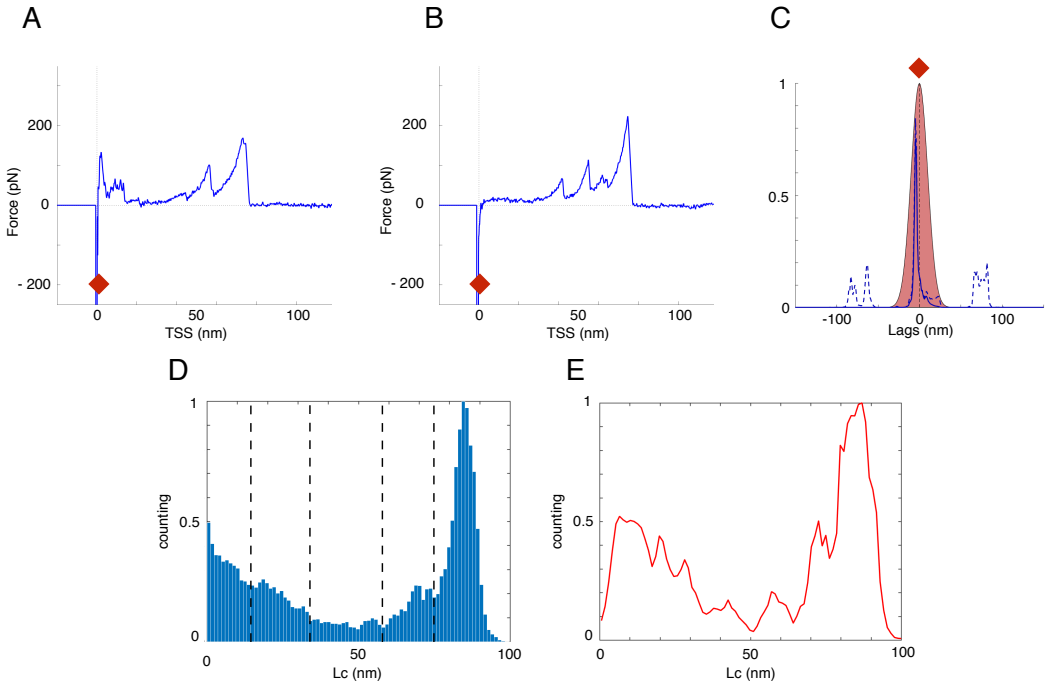

Figure 5. Supplementary. (A and B) Two typical traces. The point of the retraction curve corresponding to -200 pN is moved to 0 nm to aligned all the traces at a relative zero point. (C) Dotted line represent the correlation between the to traces in panel A and B. The gaussian centered in 0 is multiplied for the correlation between the traces (continuos line under the gaussian) in order to minimize the displacement of the F-d curves from the origin. (D) Normalized contour length histogram from the selection of traces in the presence of cAMP aligned on 0 and intervals defined along Lc coordinates (dotted vertical lines). (E) Normalized contour length histogram of the selection of traces in the presence of cAMP after the automatic alignment procedure.

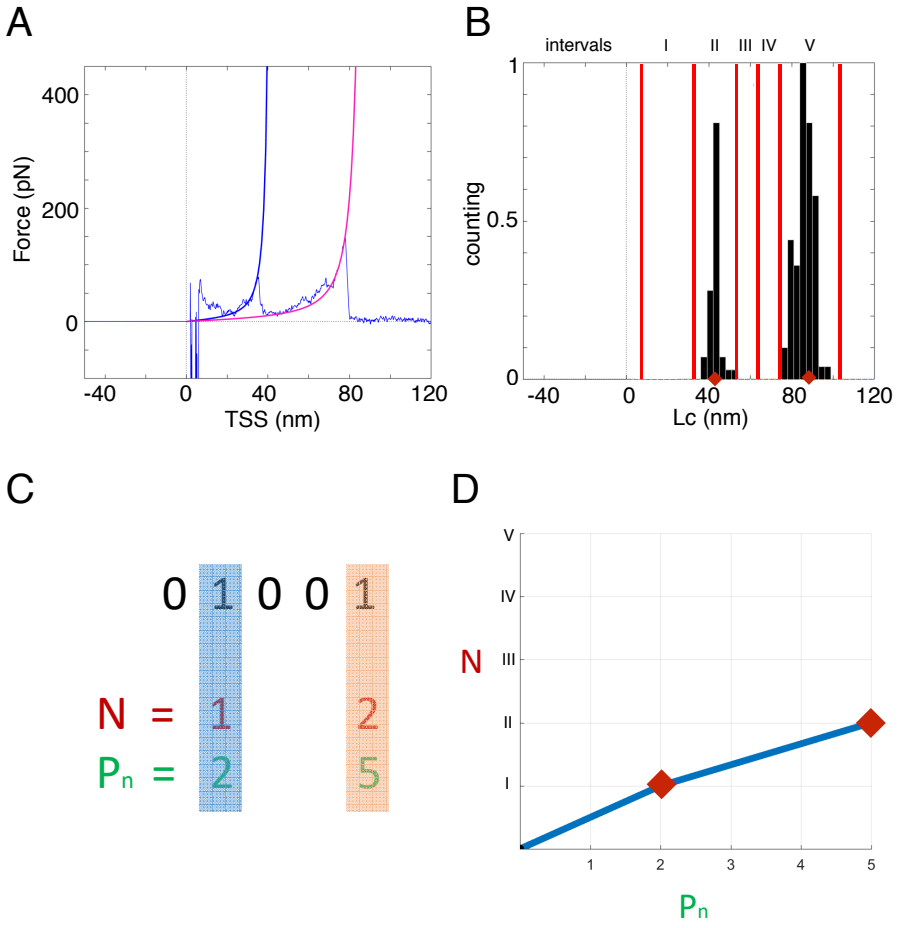

Figure 6. Supplementary. In a typical trace each force peak is fitted with the WLC model and corresponding Lc histogram is computated (A and B). (C)The histogram is coded on the base of the Lc intervals defined, so that each trace can be coded as a binary string of values; 1 is assigned if an event occur within the it-interval and 0 if not. To each positive value of the string two parameters are assigned as represented. (D) traces are represented as broken line in a N/Pn space.

Nicola Galvanetto[1,+], Andrea Pedroni[1,+], Andrea Perissinotto[1], Sourav Maity[1], and Vincent Torre[1,*]

[1]Neuroscience Area, Scuola Internazionale Superiore di Studi Avanzati (SISSA), 34136 Trieste, Italy
[*]torre@sissa.it

To the editor:

The mechanical unfolding and structural stability of single proteins can be successfully investigated with atomic force microscopy (AFM)-based single molecule force spectroscopy (SMFS) experiments[1]. Recent experimental improvements are going to redefine the quantity and the quality of collected data[2]; however, the analysis of Force vs distance (F-d) curves still requires highly operator-dependent procedures, in direct contrast with the current need of reproducibility and automation. Although, algorithms to reduce manual intervention have been published[3], there is no universal ready-to-use platform for F-d curves analysis, and often investigators must develop their own custom software.

We developed an open-source software (FaceTheWind (FTW); **Supplementary Software**), providing an all-in-one environment for F-d curves analysis, from experimental output to meaningful data representations. It contains both widely accepted statistical features **(Fig. 1 I-L;)** and advanced algorithms for clustering, alignment and unfolding pathways determination **(Fig. 1 E-H and M-O; Supplementary Fig. 2 and 3)**. FTW can open multiple raw data format from the most diffuse AFM manufacturer (JPK and Bruker Instruments), but to facilitate a general usage it can imports also ASCII matrices of F-d curves. The software is designed to assist the user in the most common critical analytical steps, like data filtering, trace selection, statistical behavior evaluation of force peaks etc., with a reversible workflow to not lose original information. Working sessions can be saved, data selections can be exported and any graphical representation can be extracted. FTW source code is fully available and modifiable to guarantee validation of existing algorithms and any further improvement.

To demonstrate the capabilities of FTW we processed F-d curves obtained from pulling experiments on oocyte membranes after the overexpression of cyclic nucleotide-gated (CNG)A1 channel[3] **(Supplementary data)**. The identification of traces of interest among the large variety of recorded spectra (hundred of thousands of curves in a typical SMFS dataset) is a crucial step. Considering that less than 0.3% of recorded traces carry useful information, it is necessary a fast and versatile filter compound. On a typical notebook computer (4 GB memory, 2.0 GHz CPU), FTW can load 1000 traces in 15 seconds and perform a filtering routine in less than 30 seconds. FTW allows obtaining final selection of valid traces through a gradual refinement of multiple parameters. In our case, CNGA1 final selection was obtained in three main filtering steps **(Fig. 1 B-D; Supplementary Fig. 4)**: i) discarding empty traces or traces with large non-specific adhesion, ii) identifying traces with peaks in a range consistent with the amino acid sequence, iii) comparing the cross-correlation matrix that highlights common features of the obtained population of curves. After that, trace selections can be both manually and automatically aligned with a free-reference procedure[4] **(Fig. 1 E-H; Supplementary Fig. 3)**. To quantitatively estimate relevant information, traces can be coded into a Global Matrix (GM) on the base of the contour length (Lc) values for each force peak automatically detected **(Fig. 1 I)**. From GM coding, several different statistical analysis and graphical representations can be generated, and possibly new ones implemented. In **Fig. 1 J** we present the Global Peaks Histogram (GPH), which counts the frequency of occurrence of force peaks respect to their position in Lc values. The GPH can be fitted by a multi Gaussian distribution to identify the most probable Lc positions of recurrent unfolding events. In FTW, we introduced a novel method for identifying different protein unfolding pathways (Path Plot: **Fig. 1 M-O; Supplementary Figure 3)**, by coding traces on the base of the number of force peaks and their position of occurrence. This method, applied to our dataset, provided evidence of recurrence in the unfolding behaviour of the transmembrane domain, but variable unfolding pathways in the the cytosolic domain of the CNG channel **(Fig. 1 N, O)**.

FTW would be a substrate on which to build a community of AFM users, with the goal of developing and sharing novel and valuable analytical approaches, and bringing them together in an all-in-one open-source software.

References

1. Kawamura, S. et al. Kinetic, Energetic, and Mechanical Differences between Dark-State Rhodopsin and Opsin. Structure 21, 426-437 (2013).

2. Otten, M. et al. From genes to protein mechanics on a chip. Nat Meth 11, 1127-1130 (2014).

3. Maity, S. et al. Conformational rearrangements in the transmembrane domain of CNGA1 channels revealed by single-molecule force spectroscopy. Nature Communications 6, 7093 (2015).

3. Bosshart, P. D., Frederix, P. L. T. M. and Engel, A. Reference-Free Alignment and Sorting of Single-Molecule Force Spectroscopy Data. Biophysical Journal 102, 2202-2211 (2012).

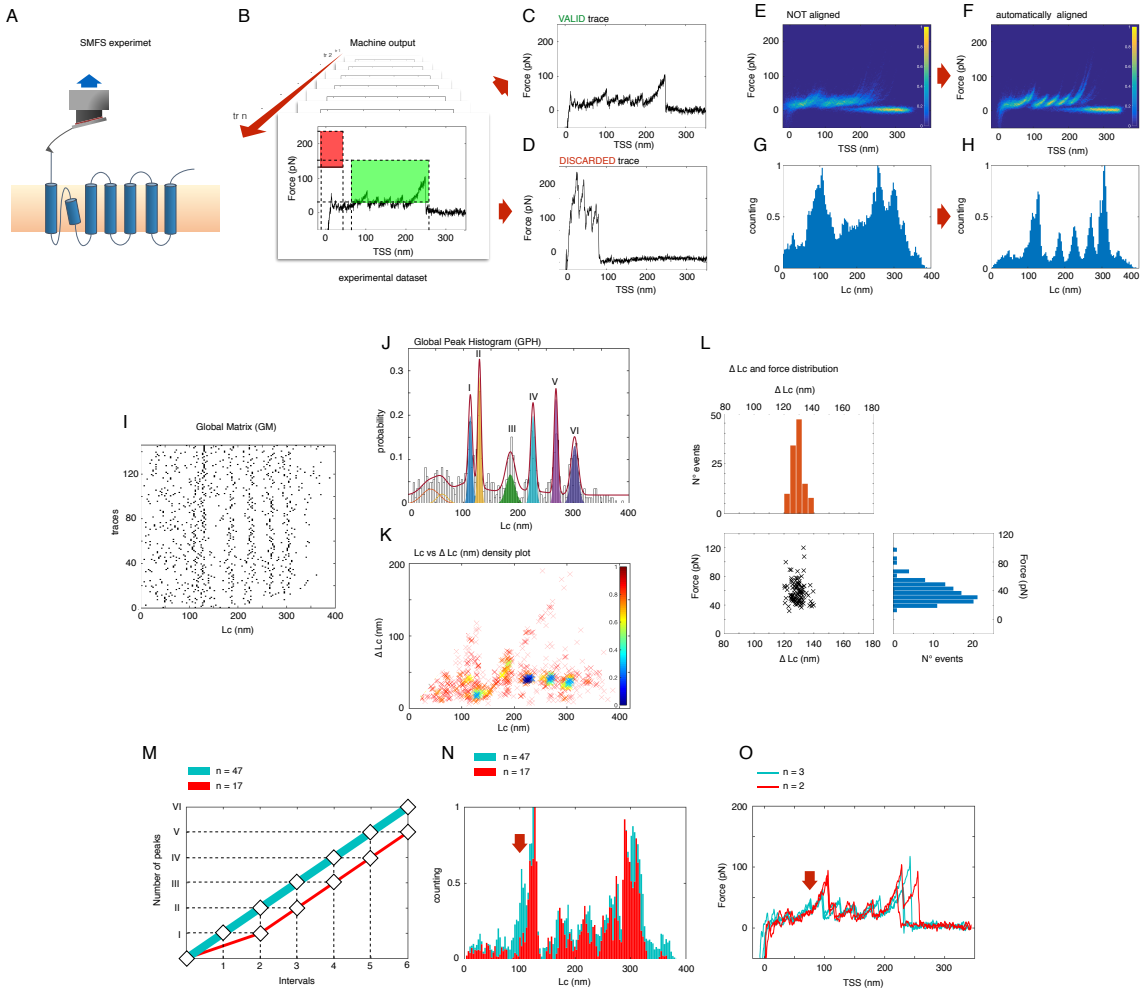

Figure 1. (A) Schematic representation of a SMFS experiment. (B) The whole dataset containing hundred of thousands of traces is filtered to find out traces of interest (C) and discard F-d curves without reliable information (D). (E, F) Superimposition of 146 F-d curves as density plot before and after automatic alignment procedure with relative normalized Lc histograms (G, H). (I) Global Matrix representation of the automatically detected maxima of each force peaks in the function of the Lc values. (J) Global Peak histogram representing the frequency of occurrence of force peaks respect to their position along Lc coordinates and multi Gaussian distribution. (K) Lc vs ΔLc plot of 146 traces superimposed as density plot. (L) Statistical evaluation of F and ΔLc for the II force peak in panel J. (M) Path plot representation of two distinct unfolding pathways (n = 47 red broken line and n = 17 cyan broken line) differing for the occurrence of the force peak at 98 nm (red arrow in panel N and P). (N) Superimposition of Global Peak histograms from traces belonging to the different unfolding pathways and (O) relative examples of F-d curves.

Supplementary Information

Software and Data

FTW software is available at this link: https://www.dropbox.com/sh/jlswyq1r1sgmw6q/AAB4xCY_ZQ9vlZ89lEvLUl5Va?dl=0 with a set of data from the CNG channel.

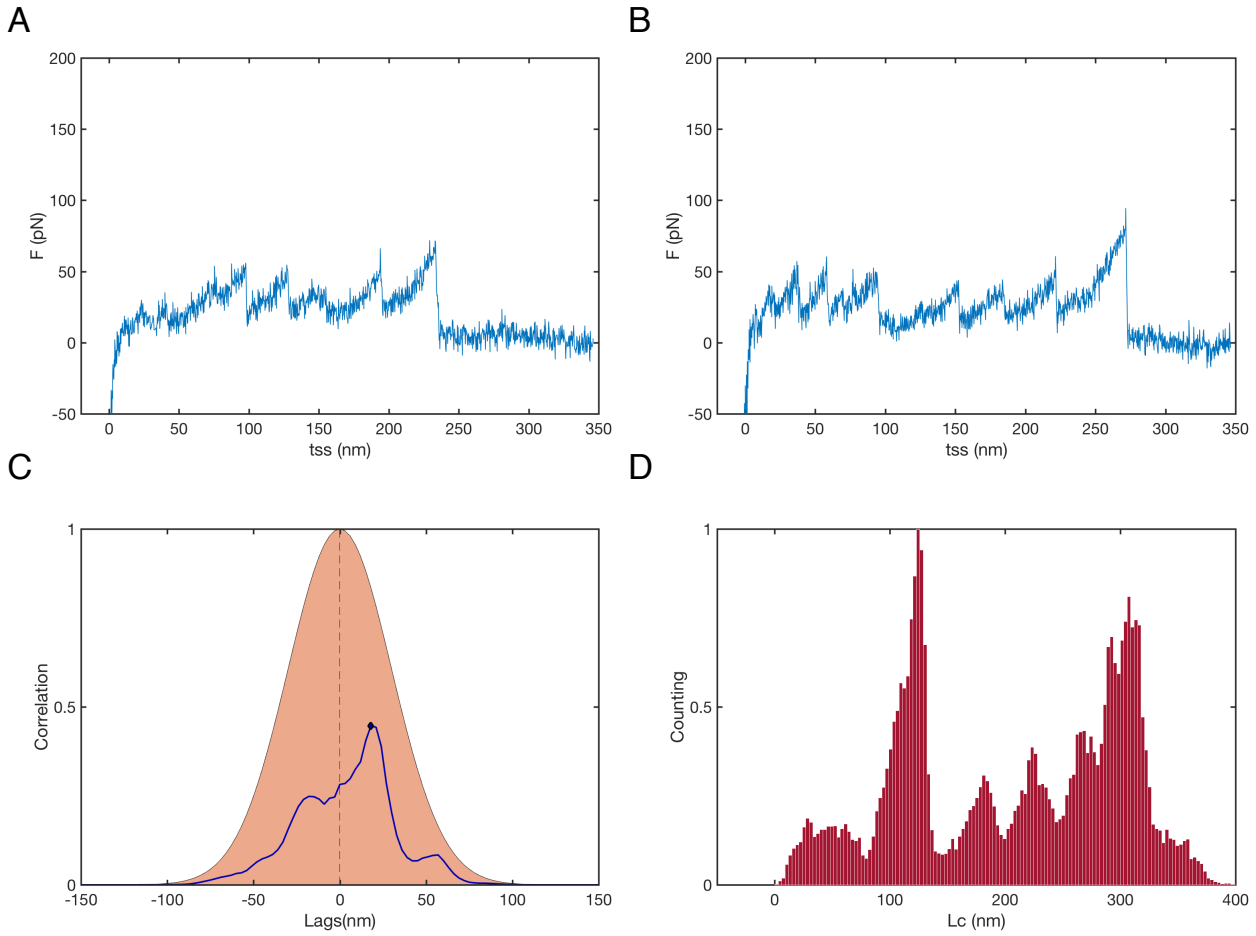

Figure 1. A free alignment procedure was successfully developed from Bosshart and colleagues, and it consists in three main steps. Firstly, the whole selection of valid traces is subdivided into groups of homogeneous traces (i.e. traces with the same number of peaks). Than traces in each groups are recursively aligned with the maximum-correlation principle, obtaining an average contour-length reference. The average contour-length reference for each group is aligned obtaining a global reference on which all the traces are newly aligned[1]. To extent the applicability of this remarkable procedure to those traces do not display constant occurrence of force peaks (i.e. different unfolding pathways or complex soluble proteins), we develop two additional intermediate steps. Firstly, we introduce a group division based on the coding method explained in path plot supplementary section (Fig. S4). In this way we imposed two constrains to each trace, dividing them on the base of the number of force peaks and grouping them accordingly to the position of occurrence of those force peaks. In the second improvement, after the contour-length histogram coding, we assign a zero-point to each trace, and set a Gaussian cantered into the zero point. Than, given the correlation curve between two traces (A and B), it can be multiply with the Gaussian obtaining an estimator of the displacement of the curves from the zero-point (blue line under the Gaussian in C). (D) Lc histogram of 146 valid traces automatically aligned with this procedure.

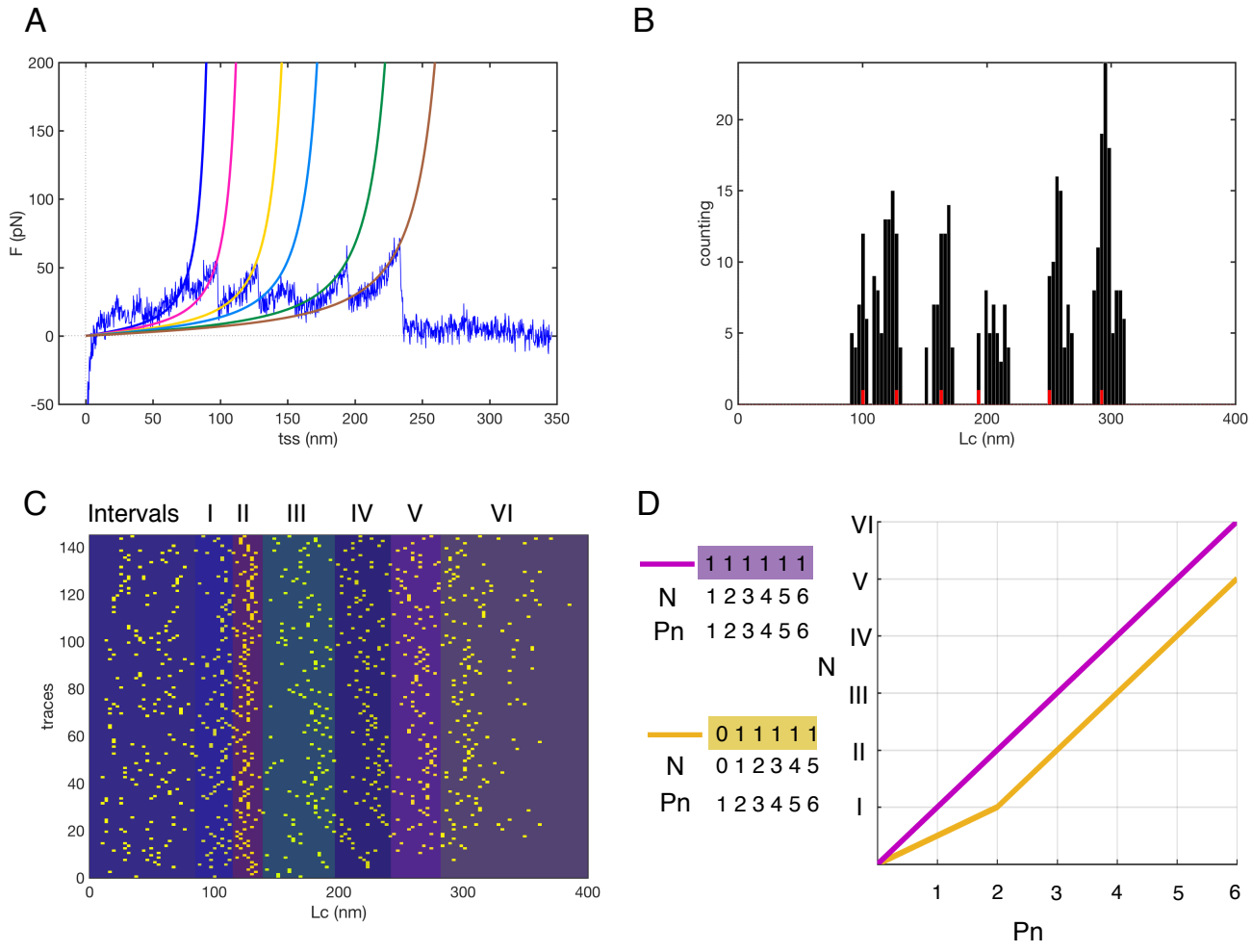

Figure 2. A typical F-d trace fitted with the WLC model (A) is coded in corresponding Lc histogram (B). (C) Each traces is computed into the Global Matrix histogram. On the histogram n intervals are defined and each traces is coded in n digits as presented in D. 1 is assigned if an event occur within the it-interval and 0 if not. (D) To each positive value of the string two parameters are assigned as represented so that coded traces can be represented as broken line in a N/Pn space.

frontiers in
CELLULAR NEUROSCIENCE

ORIGINAL RESEARCH ARTICLE
published: 14 February 2014
doi: 10.3389/fncel.2014.00044

Electrophysiological characterization of granule cells in the dentate gyrus immediately after birth

Andrea Pedroni[1], Do Duc Minh[1], Antonello Mallamaci[1] and Enrico Cherubini[1,2]*

[1] *Department of Neuroscience, Scuola Internazionale Superiore di Studi Avanzati, Trieste, Italy*
[2] *European Brain Research Institute, Rome, Italy*

Edited by:
Richard Miles, Institut pour le Cerveau et la Moëlle Epinière, France

Reviewed by:
Claudia Lodovichi, Venetian Institute of Molecular Medicine, Italy
Carolina Hoyo-Becerra, Clinic Hospital Essen, Germany

***Correspondence:**
Enrico Cherubini, Department of Neuroscience, Scuola Internazionale Superiore di Studi Avanzati, Via Bonomea 265, 34136 Trieste, Italy
e-mail: cher@sissa.it

Granule cells (GCs) in the dentate gyrus are generated mainly postnatally. Between embryonic day 10 and 14, neural precursors migrate from the primary dentate matrix to the dentate gyrus where they differentiate into neurons. Neurogenesis reaches a peak at the end of the first postnatal week and it is completed at the end of the first postnatal month. This process continues at a reduced rate throughout life. Interestingly, immediately after birth, GCs exhibit a clear GABAergic phenotype. Only later they integrate the classical glutamatergic trisynaptic hippocampal circuit. Here, whole cell patch clamp recordings, in current clamp mode, were performed from immature GCs, intracellularly loaded with biocytin (in hippocampal slices from P0 to P3 old rats) in order to compare their morphological characteristics with their electrophysiological properties. The vast majority of GCs were very immature with small somata, few dendritic branches terminating with small varicosities and growth cones. In spite of their immaturity their axons reached often the cornu ammonis 3 area. Immature GCs generated, upon membrane depolarization, either rudimentary sodium spikes or more clear overshooting action potentials that fired repetitively. They exhibited also low threshold calcium spikes. In addition, most spiking neurons showed spontaneous synchronized network activity, reminiscent of giant depolarizing potentials (GDPs) generated in the hippocampus by the synergistic action of glutamate and GABA, both depolarizing and excitatory. This early synchronized activity, absent during adult neurogenesis, may play a crucial role in the refinement of local neuronal circuits within the developing dentate gyrus.

Keywords: dentate gyrus granule cells, immature hippocampus, postnatal development, sodium spikes, low threshold calcium spikes, synchronized network activity, neurogenesis, giant depolarizing potentials

INTRODUCTION

Granule cells (GCs) in the dentate gyrus are crucial for transferring information from the entorhinal cortex to the hippocampus proper where they integrate the classical excitatory trisynaptic circuit (McBain, 2008). Although primarily glutamatergic, the axons of GCs, the mossy fibers (MFs), contain GABA, its synthesizing enzyme glutamic acid decarboxylase (Schwarzer and Sperk, 1995; Sloviter et al., 1996) and the vesicular GABA transporter VIAAT (Zander et al., 2010). In addition, immunogold experiments have demonstrated the presence of both AMPA and $GABA_A$ receptors, co-localized on MF terminals in close spatial relation with synaptic vesicles (Bergersen et al., 2003). All these pieces of evidence suggest that MF-cornu ammon (CA3) synapses can use GABA as a neurotransmitter since they posses all the machinery for synthesizing, storing, releasing, and sensing it.

Indeed, electrophysiological experiments from juvenile animals have revealed the presence of mixed GABAergic and glutamatergic monosynaptic currents in CA3 principal cells upon stimulation of GCs in the dentate gyrus (Walker et al., 2001; Gutierrez et al., 2003). Furthermore, in line with the sequential formation of GABAergic and glutamatergic synapses in the immature hippocampus (Hennou et al., 2002), GABA appears to be the only neurotransmitter released from MF terminals during the first few days of postnatal life (Kasyanov et al., 2004; Safiulina et al., 2006, 2010; Sivakumaran et al., 2009) while AMPA/kainate receptor mediated synaptic currents start appearing only after postnatal (P) day 3 (Marchal and Mulle, 2004).

Granule cells are characterized by their peculiar delayed and heterogeneous maturation. Most of them (85%) are generated postnatally. From the primary dentate matrix, neural precursors migrate to the dentate gyrus between embryonic day 10 and 14 where they differentiate into neurons (Altman and Bayer, 1990a,b). Neurogenesis reaches a peak at the end of the first postnatal week and is largely completed toward the end of the first postnatal month (Schlessinger et al., 1975). Interestingly, the dentate gyrus retains the capability to give rise to new neurons throughout life, although at a reduced rate (Duan et al., 2008). In adulthood, after being generated in the subgranular zone, immature GCs are incorporated into pre-existing circuits, thus contributing to improve several brain functions including learning and memory processes (Deng et al., 2010).

The maturation of GCs during postnatal development has been extensively investigated (Liu et al., 1996; Liu et al., 2000; Ye et al., 2000; Ambrogini et al., 2004; Overstreet et al., 2004; Espósito et al., 2005; Overstreet-Wadiche and Westbrook, 2006; Overstreet-Wadiche et al., 2006). However, only few studies, have

tried to compare the morphological characteristics of immature GCs with their functional properties before P7, when neurogenesis in the dentate gyrus is very active and GCs exhibit immature-like features (Liu et al., 1996, 2000; Ambrogini et al., 2004).

Therefore, in the present study, whole-cell patch clamp recordings were performed from biocytin-labeled GCs in the immediate postnatal period, between P0 and P3, when GCs convey exclusively monosynaptic GABAergic signals to CA3 pyramidal cells (Safiulina et al., 2006).

MATERIALS AND METHODS

ETHICAL APPROVAL

All experiments were performed in accordance with the European Community Council Directive of November 24, 1986 (86/609EEC) and were approved by the local authority veterinary service and by SISSA ethical committee. All efforts were made to minimize animal suffering and to reduce the number of animals used.

HIPPOCAMPAL SLICES PREPARATION

Wistar rats of both sexes were decapitated after being anesthetized with CO_2. Hippocampal slices were obtained from neonatal animals at postnatal (P) days P0–P3 (the day 0 was considered as the day of birth) as previously described (Caiati et al., 2010). Briefly, the brain was quickly removed from the skull and placed in ice-cold ACSF containing (in mM): NaCl 130, KCl 3.5, NaH_2PO_4 1.2, $MgCl_2$ 1.3, $CaCl_2$ 2, Glucose 24, $NaHCO_3$ 27 (pH 7.3), saturated with 95% O_2 and 5% CO_2 (pH 7.3–7.4)

Transverse hippocampal slices (400 μm thick) were cut with a vibratome and stored at room temperature (20–24°C) in a holding bath containing the same solution as above. After a recovery period of at least 1 h, an individual slice was transferred to the recording chamber where it was continuously superfused with oxygenated ACSF at 31–33°C at the rate of 3–4 ml min^{-1}.

ELECTROPHYSIOLOGICAL RECORDINGS

Whole-cell patch clamp recordings (mainly in current clamp mode) were obtained from visually identified GCs in the dentate gyrus, using the Multiclamp 700A amplifier (Axon Instrument, USA).

Patched electrodes were pulled from borosilicate glass capillaries (Hingelberg, Malsfeld, Germany). They had a resistance of 5–8 MΩ when filled with an intracellular solution containing (in mM): KCl 140, $MgCl_2$ 1, EGTA 0.5, HEPES 10, Mg ATP 4 (pH 7.3; the osmolarity was adjusted to 280 mOsmol).

The stability of the patch was checked by repetitively monitoring the input and series resistance during the experiment. Cells exhibiting > 15 changes in series resistance were excluded from the analysis. The series resistance was <20 MΩ and was not compensated.

Spontaneously occurring giant depolarizing potentials (GDPs) were routinely recorded from a holding potential of −70 mV.

DRUGS

Drugs used were: tetrodotoxin (TTX, purchased from Latoxan, Valence, France), 6,7-dinitroquinoxaline-2,3-dione (DNQX), bicuculline methiodide (purchased from Tocris Cookson Inc., UK), and biocytin (purchased from Sigma-Aldrich Milano, Italy). All drugs were dissolved in ACSF except DNQX that was dissolved in DMSO. The final concentration of DMSO in the bathing solution was 0.1%. At this concentration, DMSO alone did not modify the shape or the kinetics of synaptic currents. Drugs were applied in the bath via a three-way tap system, by changing the superfusion solution to one differing only in its drug(s) content. The ratio of flow rate to bath volume ensured complete exchange within 2 min.

DATA ACQUISITION AND ANALYSIS

Data were acquired and digitized with an A/D converter (Digidata 1200, Molecular Devices) and stored on a computer hard disk. Acquisition and analysis were performed with Clampfit 9 (Axon Instruments, USA). Data were sampled at 20 kHz and filtered with a cut off frequency of 2 kHz. The resting membrane potential (RMP) was measured immediately after break-in and establishing whole-cell recording. The input resistance (R_{in}) was calculated by the slope of the linear portion of the I/V relationship obtained by measuring the steady-state potential changes in response to hyperpolarizing current steps of increasing intensity (from −60 to +120 pA, 20 pA increments, 500 ms duration) using the Clampfit program (pClamp 9.0 software, Axon Instrument, USA). The membrane surface was estimated in voltage clamp mode by integrating the area under the average of four uncompensated and unfiltered charging transients in response to hyperpolarizing steps from a holding potential of −60 mV.

Action potentials were evoked in current clamp mode from a holding potential of −60 mV by 500 ms depolarizing current pulses. Spike width was measured at the base of action potentials and spike amplitude from the baseline to the peak. Spike threshold was determined at the beginning of the fast up rise of an action potential. Possible sag in electrotonic potentials were identified by injecting hyperpolarizing current pulses of different intensities through the recording pipette.

Unless otherwise stated, data are presented as mean ± SEM. Quantitative comparisons were based on students paired or unpaired *t*-test, as required and a p value < 0.05 was considered as significant.

CELL STAINING

Post hoc identification of recorded cells was achieved by injecting biocytin (1–2%, from Sigma Aldrich, Milano, Italy, dissolved in the internal solution) throughout the recording electrode for at least 40–60 min. After electrode removal slices were kept in the recording chamber, continuously superfused for at least 15–20 min. to optimize the complete diffusion of biocytin. Slices were then removed from recording chamber, thoroughly washed with phosphate buffered saline (PBS) 1X and fixed with parafolmaldehyde 4% for 20 min. at room temperature and stored at 4°C. Slices were incubated with Alexa Flour 647-labeled streptavidin, 1:500 for 1 h at room temperature, sheltered from the light. They were washed, thoroughly rinsed with 1x PBS, mounted onto slides, embedded with Vectashield (Vector Laboratories), and coverslipped. Individual pictures of biocytin-filled cells were acquired with a Nikon microscope (Eclipse Series TiE, equipped with a C1 confocal system) along progressive focal planes to fully cover their volume (including their dendritic and axonal projections).

IMMUNOCYTOCHEMISTRY

Free-floating recorded slices were rinsed several times with 1x PBS and incubated in a blocking solution containing 5% FBS (fetal bovine serum) and 0.3% Triton X-100 in PBS, for 30 min. Primary antibodies (anti-Prox1, ab37128, rabbit polyclonal, Abcam, Cambridge, MA, USA 1:500; anti-NeuN, MAB377, mouse monoclonal, Millipore, Billerica, MA, USA, 1:500), diluted in 95% PBS-5% FBS solution, were applied and incubated at room temperature for 2 h. Then, slices were washed several times with 1x PBS and incubated with secondary antibody (Alexa 488-conjugated goat anti-mouse immunoglobulin G [IgG], 1:500, 594-conjugated goat anti-rabbit IgG, 1:500, Alexa Flour 647-labeled streptavidin, 1:500 and 4,6′-diamidino-2-phenylindole [DAPI], 1:1000) for 1 h at room temperature, sheltered from the light. Finally, slices were washed, thoroughly rinsed with 1x PBS, mounted onto slides, embedded with Vectashield (Vector Laboratories), and coverslipped.

RESULTS

IDENTIFICATION OF GRANULE CELLS

Granule cells were identified thanks to their immunoreactivity for Prox1. This is a homeoprotein expressed in several brain regions including the dentate gyrus, where it is present throughout development and in adulthood (Lavado and Oliver, 2007). Mature GCs were further distinguished as immunoreactive for NeuN. This is a nuclear antigen expressed in most neuronal cell types throughout the adult nervous system (Mullen et al., 1992), which is specifically activated in GCs by the end of their maturation (Ming and Song, 2011; Hsieh, 2012; Iwano et al., 2012). The spatio-temporal distribution of immature GCs in the dentate area was investigated at three postnatal stages: P2, P6, and P28. As shown in **Figure 1**, at P2, NeuN-positive cells were mainly clustered in the pyramidal layer of the CA3 region and scattered throughout the hilus. At this age, only a few NeuN-positive cells where found in the coalescing Prox1-positive dentate gyrus, where NeuN co-localized with Prox1. At P6, comparable numbers of Prox1-positive/NeuN-negative and Prox1-positive /NeuN-positive cells were detectable within the inner layer and the outer layer of the granule cell layer (GCL), respectively, Finally, at P28, almost all Prox1-positive neurons expressed NeuN, except a few NeuN- elements close to the subgranular zone. In a few words, immature GCs, largely prominent at P2, coexist with similar numbers of mature elements at P6 and become a minority by P28.

BIOCYTIN-LABELED GCs EXHIBIT AN IMMATURE PHENOTYPE

Immunocytochemical data have clearly demonstrated that at P2 GCs exhibit a typical immature phenotype. To fully characterize the functional properties of these cells, stable whole-cell recordings (mainly in current clamp configuration), lasting more than 30 min, were obtained from 63 putative GCs in slices obtained from P0 to P3 old rats. Some of these cells (11/63), were intracellularly labeled with biocytin. Cells were identified as GCs on the basis of their cell bodies localized in the GC layer and dendrites oriented toward the molecular layer. The vast majority of labeled cells exhibited small bodies and few short dendrites emerging mainly from the top or sides of cell bodies, oriented toward the molecular layer or running tangentially to the GC layer (**Figure 2**). In comparison with more mature GCs (see Liu et al., 2000; Overstreet et al., 2004; Markwardt et al., 2009) dendrites never penetrated deeply into the molecular layer or reached the top (**Figures 2A–C**). They were short, thick and spineless with limited branching. They often displayed small varicosities, filopodia and growth cones (**Figures 2A–C,E**). Presumed GC axons with initial extension toward the hilus could be visualized. In four cases, these could be followed up to stratum

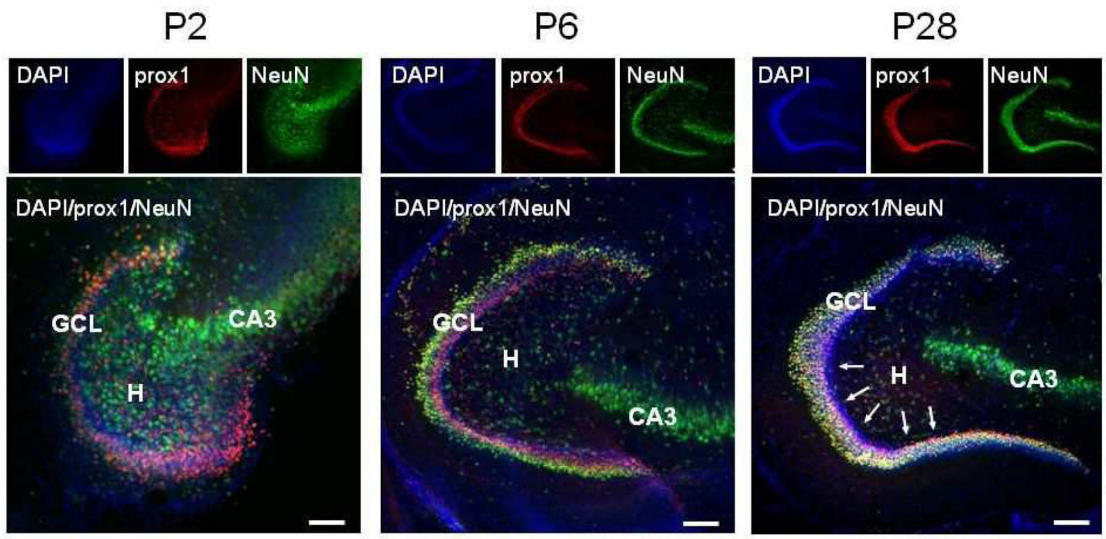

FIGURE 1 | Representative confocal images of immunostained P2, P6, and P28 horizontal sections of the hippocampus. DAPI staining, Prox1 and NeuN immunoreactivity are in blue, red, and green, respectively. Pink (DAPI+, Prox1+, NeuN−), immature granule cells predominate in the coalescing P2 GCL, they occupy the inner half of the P6 GCL and are rare in the P28 GCL, where they are confined to a row close to the subgranular zone (arrows). GCL, granule cell layer; H, hilus; CA3, cornu ammonis 3 field.

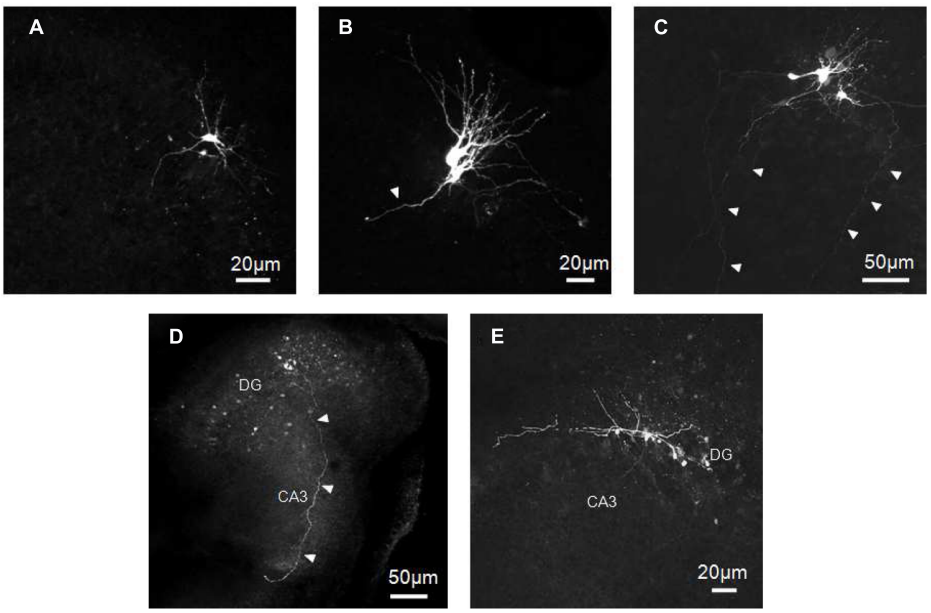

FIGURE 2 | Biocytin-labeled GCs at P0–P2. GCs exhibit small cell bodies with few short and tick dendrites oriented toward the molecular layer **(A–C)** and/or running tangentially to the GC layer **(C,E)**. Dendrites often display small varicosities, filopodia and growth cones **(B,C,E)**. Presumed GC axons projecting through the hilus toward stratum lucidum can be seen in **C,D**. Arrowheads indicate presumable axons.

lucidum in the CA3 subfield (**Figures 2C,D**). The axons expressed varicosities but lacked mature MF boutons and often gave rise to collateral branches that terminated with growth cones. Although care was used to pull out the patch pipette from the recorded neuron at the end of the experiments, more than one GC was often labeled, suggesting dye-coupling (**Figures 2** and **7A**). However, due to their small diameter, we failed to patch two adjacent neurons to verify whether dye-coupled cells were also electrically coupled.

ELECTROPHYSIOLOGICAL CHARACTERISTICS OF IMMATURE GCs

Immature GCs were identified as neurons by their capacity to generate action potentials. We examined firstly the passive membrane properties ($n = 63$). On average, the RMP was -39 ± 1 mV (ranging from -58 to -23 mV); the input resistance (R_{in}) 1.2 ± 0.1 GΩ (ranging from 0.3 to 2.9 GΩ), the membrane capacitance (C) 15.4 ± 0.7 pF (ranging from 8 to 31 pF) and the membrane time constant (τ) 285 ± 17 ms.

A large variability of individual RMP, C, and R_{in} values occurred between P0 and P3 (**Figure 3**). A large variability was also observed within the same postnatal group and between different cells recorded from the same slice. In spite of similar values of RMP, R_{in}, capacitance and membrane time constant, immature GCs exhibited marked changes in their excitability as assessed by the large variability in spike detection. Four cells, exhibiting relatively low R_{in} (0.8 ± 1 MΩ), more depolarized RMP (-35 ± 1 mV) and low capacitance values (8 ± 1 pF) were unable to generate action potentials in response to depolarizing currents pulses (non-spiking cells). These cells could be non-differentiated progenitors, astrocytes, oligodendrocytes and/or very immature neurons. Therefore, they were excluded from the present analysis.

Spiking neurons were divided in two groups on the basis of their ability to generate over-shooting action potentials or not (**Table 1**).

The first group ($n = 36$) comprised more immature cells with rudimentary short and wide TTX-sensitive sodium spikes. Often in the presence of TTX, low threshold calcium spikes appeared and these were blocked by low concentrations of nickel (100 μM; **Figure 4**). The second group of cells ($n = 27$) was characterized by clear overshooting action potentials, which in some cases fired repetitively (**Figure 5**).

In comparison with more immature cells, these exhibited a lower threshold for action potential generation, and a reduced spike half-width value (**Table 1**).

In the presence of TTX, low threshold calcium spike could be sometimes evoked from a more hyperpolarized holding potential (-80 mV; **Figure 4**).

Both groups exhibited electrotonic potentials that strongly rectified in the depolarizing direction, probably due to the activation of voltage-gated potassium conductances. In 23 GCs exhibiting both rudimentary and more mature spikes, a prominent time-dependent sag in the electrotonic potentials could be elicited by hyperpolarizing current steps. The sag accounted for most of the rectification in the hyperpolarizing range and had the characteristics of the time-dependent inward rectifier cationic current I_Q, described in the hippocampus (Halliwell and Adams, 1982; data not shown).

CORRELATED NETWORK ACTIVITY

Most (58/63) spiking neurons, recorded from P0 to P3, exhibited patterns of coherent activity reminiscent of that found in the developing Ammon's horn (Ben-Ari et al., 1989) and described as GDPs. As in the CA1 and CA3 hippocampal regions, GDPs

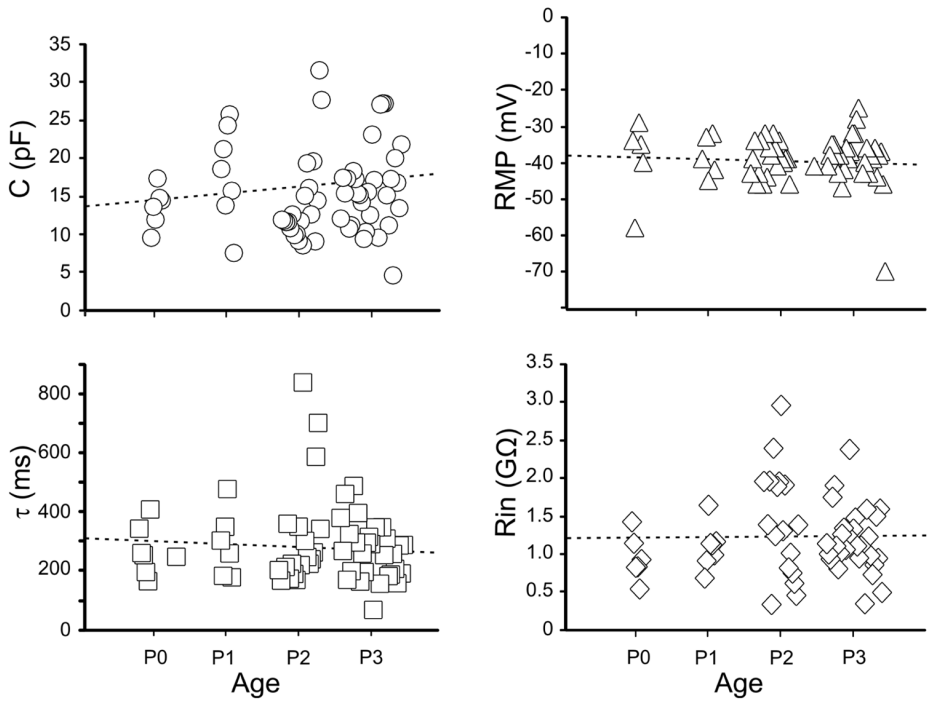

FIGURE 3 | Passive membrane properties of immature granule cells. Individual values of capacitance (C, open circles), resting membrane potential (RMP, open triangles), decay time constant (τ, open squares) and membrane input resistance (R_{in}, open diamonds), detected between P0 and P3.

were either grouped in clusters of 2–5 (**Figure 6B**) or occurred at more or less regular intervals (**Figure 6C**) at the frequency of 0.1 ± 0.3 Hz, often preceded by a barrage of synaptic events. Few spiking neurons did not exhibit GDPs but only spontaneous activity either isolated or in bursts that often reached the threshold for action potential generation (**Figure 6A**).

Giant depolarizing potentials were characterized by long-lasting recurrent membrane depolarizations (up to 30 mV in amplitude) giving rise to action potentials often grouped in bursts and separated by silent periods. GDPs were network-driven events since their frequency, but not their amplitude, was unaffected by changing the membrane potential to more depolarized or hyperpolarized values.

Although reduced in frequency, GDPs were still present in DNQX (20 μM; **Figure 7**) suggesting that, in the absence of a glutamatergic drive, the depolarizing action of GABA was still able to exert an excitatory action at the network level. In two cases, in the presence of DNQX long-lasting (13 and 19 s duration) plateau potentials could be unveiled.

These were probably generated by the activation of intrinsic membrane conductances, known to involve small groups of neurons coupled by gap-junctions (**Figure 7**; Crépel et al., 2007). However, the rare occurrence of these events did not allow testing whether they were sensitive to gap junction uncouplers or could be blocked by hyperpolarizing the membrane toward more negative values. GDPs were completely abolished by DNQX plus bicuculline (20 μM), indicating that they were triggered by the synergistic action of both glutamate and GABA. As in immature CA3 principal cells (Ben-Ari et al., 1989), synchronized activity was blocked by TTX (1 μM) further supporting their network origin (data not shown).

Table 1 | Passive and active membrane properties of granule cells at P0–P3 (*$p < 0.05$; **$p < 0.01$).

	Immature neurons with rudimentary spikes	More mature neurons with overshooting action potentials and repetitive firing
n	36	27
C (pF)	14 ± 1	17 ± 1*
RMP (mV)	−38 ± 1	−40 ± 1
R_{in} (GΩ)	1.4 ± 0.1	1 ± 0.1**
τ (ms)	283 ± 23	285 ± 25
Spike threshold (mV)	−26 ± 1	−34 ± 1**
Spike amplitude (mV)	13 ± 1	22 ± 2**
Spike half-width (ms)	6.1 ± 0.6	3.8 ± 0.2**

DISCUSSION

The present data clearly show that, immediately after birth, GCs in the dentate gyrus exhibit different degrees of immaturity as revealed by immunocytochemical experiments and *post hoc* morphological reconstruction of biocytin-labeled cells.

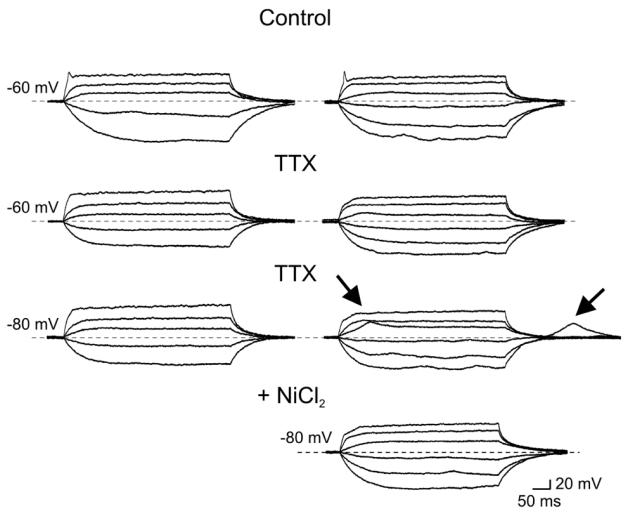

FIGURE 4 | Immature granule cells exhibit rudimentary sodium spikes and low threshold calcium spikes. Voltage responses obtained in two GCs (at P2) exhibiting sodium (right and left columns) and low threshold calcium currents (right). In control, both GCs exhibited small amplitude rudimentary spikes (at −60 mV, upper traces) that were blocked by TTX (1 μM). In the presence of TTX, depolarizing current pulses from −80 mV evoked only in the cell to the right a low threshold calcium spike. This was also present upon membrane re-polarization following an hyperpolarizing current step. Low threshold calcium spikes (marked by arrows) were blocked by nickel (100 μM, lower trace on the right).

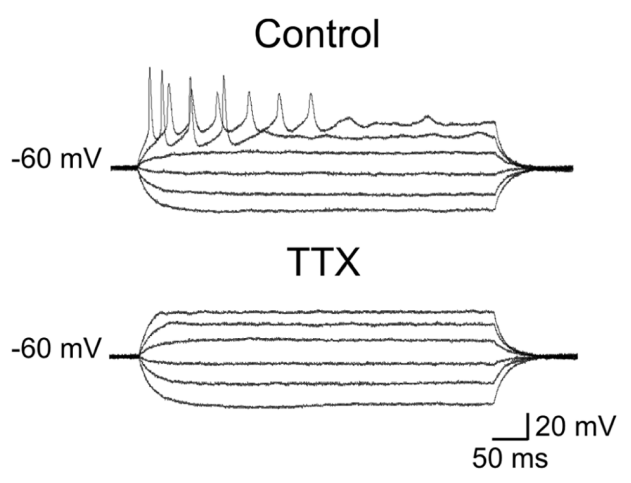

FIGURE 5 | Repetitive firing evoked in more mature granule cells. Voltage responses to depolarizing and hyperpolarizing currents steps of increasing intensity. Note clear overshooting spikes firing repetitively during depolarizing current pulses. Action potentials were readily blocked by TTX.

Thus, at P2, only a small percentage of Prox1-positive GCs were labeled with NeuN, which is specifically activated near the end of their differentiation process (Ming and Song, 2011). In keeping with a mixed GABAergic and glutamatergic neurotransmission of immature MF (Münster-Wandowski et al., 2013), a recent study has unveiled that Prox1-positive GCs transiently express the GABA synthesizing enzyme GAD67, thus supporting

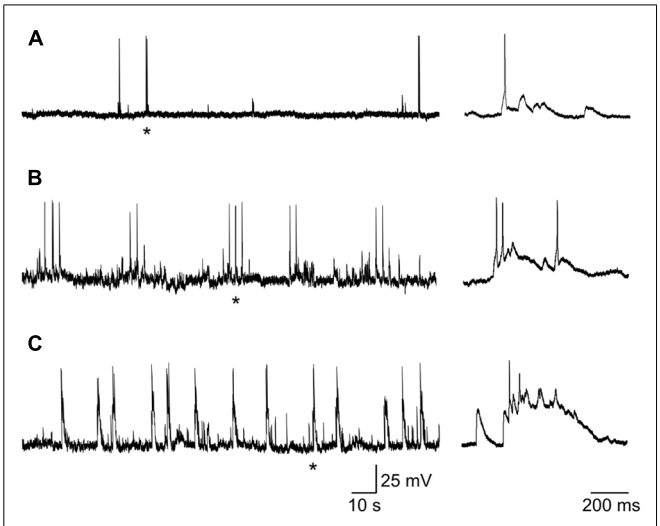

FIGURE 6 | Different patterns of coherent activities in neonatal GCs. **(A)** neuron (at P1) exhibiting sporadic depolarizing synaptic potentials that in few cases reached the threshold for action potential generation. **(B)** GDPs occurring in clusters of 2–3. **(C)** GDPs occurring at more regular intervals. Single action potentials or GDPs marked with * are shown on the right on an expanded time scale.

the view that, immediately after birth, GCs are able to synthesize GABA in addition to glutamate (Cabezas et al., 2013). GABA released from MF terminals may activate pre (Cabezas et al., 2012) and/or postsynaptic $GABA_A$ receptors (Safiulina et al., 2006, 2010) to modulate MF excitability and to generate $GABA_A$ mediated postsynaptic currents in targeted neurons, respectively.

Biocytin-labeled GCs express different degrees of immaturity. In general, they revealed few dendritic branches with short dendrites barely penetrating into the molecular layer and exhibiting varicosities and filopodia. In contrast with their dendritic arborization the axons of immature GCs, the MF, were able to reach the CA3 pyramidal layer already at P1. Although we don't know whether GCs axons made synaptic contacts with principal cells, it is likely that, similarly to the visual system (Kasper et al., 1994), the maturation of the dendritic tree takes place after GC axons have reached the CA3 subfield, supporting the view that this process is influenced by retrograde signals (Jones et al., 2003). Previous studies have shown that mature adult-like GCs, characterized by elongated dendrites (with spines) penetrating into the molecular layer, start appearing toward the end of the first postnatal week (Jones et al., 2003).

Our electrophysiological data obtained from P0 to P3 old rats unveiled passive membrane properties similar to those obtained from older rats at P5–P8 (Liu et al., 1996; Liu et al., 2000; Ye et al., 2000; Ambrogini et al., 2004), indicating that a certain degree of immaturity persists at late developmental stages. Usually, maturity is characterized by progressive more hyperpolarized values of RMP, decrease in membrane time constant, in R_{in} and increase in membrane capacitance (Spigelman et al., 1992). However, in the present case, these values were rather scattered and no significant differences were observed between GCs recorded at P0

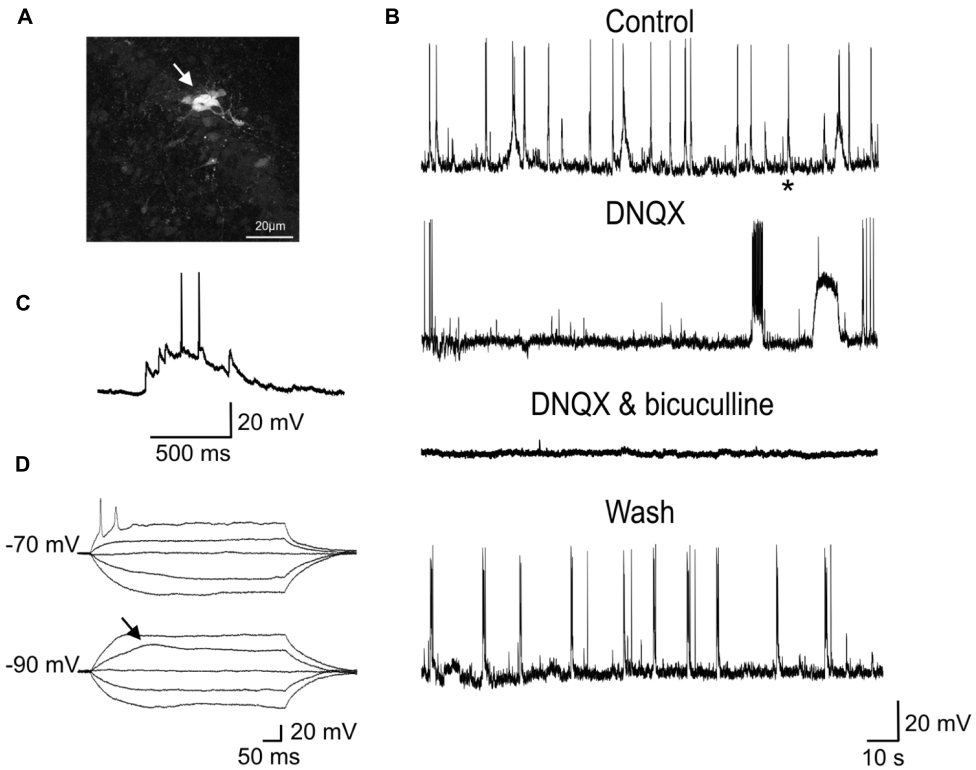

FIGURE 7 | Network-driven GDPs were reduced in frequency by DNQX and blocked by DNQX plus bicuculline. (A) Whole-cell recording of a P2 GC with biocytin revealed a cluster of several dye-coupled neurons. **(B)** Sample traces of spontaneous activity (GDPs) recorded from the same neuron in control conditions, in DNQX (20 μM), in DNQX and bicuculline (20 μM) and after wash. In the presence of DNQX, GDPs occurred at lower frequency. In DNQX it is visible also a plateau potential. **(C)** The GDP marked with an asterisk in the control trace is shown on an expanded time scale. **(D)** Voltage responses to depolarizing and hyperpolarizing currents steps of increasing intensity obtained from the same neuron. Note sodium and low threshold calcium spikes.

and P3. All patched cells exhibited high values of R_{in}. However, respect to more mature cells, immature neurons with rudimentary spikes displayed higher R_{in} values associated with lower capacitance. These factors, combined with the compact size of immature GCs, likely contribute to their high degree of excitability, such that even small fluctuations in membrane conductance may produce large voltage responses. This can be attributed to changes in the expression of intracellular anions and potassium efflux. Moreover, a developmentally regulated expression of voltage-gated sodium, calcium and potassium channels (Spigelman et al., 1992) may account for differences in active membrane properties such as spike amplitude and duration. The fact that rudimentary spikes were blocked by TTX suggests that voltage-dependent sodium channels are responsible for spike genesis. Interestingly, rudimentary sodium spikes were accompanied with low threshold calcium spikes. T-type Ca^{2+} currents underling low threshold calcium spikes have been originally described in sensory neurons where they are developmentally regulated since they disappear during the first few weeks of postnatal life, suggesting a major role in the generation of oscillatory activities (Huguenard, 1996). In the cerebellum, the developmental expression of low threshold calcium spikes parallels that of the dendritic tree, indicating a possible dendritic localization of this conductance (Gruol et al., 1992). In the present experiments we cannot exclude the involvement of calcium conductances localized on dendrites. However, this hypothesis seems unlikely since maturation of GC dendrites is usually associated with the loss of low threshold calcium spikes. Although the functional role of low threshold calcium channels in immature GCs is still unclear, these may boost calcium entry *via* high threshold calcium channels and/or NMDA receptors following the depolarizing action of GABA thus contributing to GDPs generation. The transient elevation in intracellular calcium level during GDPs activates signaling pathways known to control several developmental processes, including DNA synthesis, neuronal migration, differentiation, and synaptogenesis (Cherubini et al., 2011). It is worth mentioning that in adult-born GCs low threshold calcium currents were present only in cells with synaptic inputs, suggesting that T-type of channels may play a crucial role in cell differentiation and in synaptic plasticity processes (Ambrogini et al., 2004; Schmidt-Hieber et al., 2004).

Although the present experiments clearly show that immature GCs are in several aspects similar to adult-born neurons in the inner GC layer (Laplagne et al., 2006, 2007; Overstreet-Wadiche and Westbrook, 2006; Overstreet-Wadiche et al., 2006; Zhao et al., 2010), they are functionally different since, unlike adult-born GCs, immature GCs display network-driven GDPs. This can be

attributed to the depolarizing and excitatory action of GABA that, compared with the adult hippocampus, early in postnatal life is very pronounced. GABA-induced membrane depolarization may act in synergy with glutamate to synchronize neuronal networks. GDPs have been already described in the fascia dentata of immature rabbits (Menendez de la Prida et al., 1998) and rats (Hollrigel et al., 1998). In rabbits GDPs persisted when the dentate gyrus was isolated from the Ammon's horn indicating that the entire hippocampal network possesses the capacity to generate them.

Here, the observation that GDPs persisted at lower frequency in the presence of the AMPA/kainate receptor antagonist DNQX strongly suggests the depolarizing and excitatory action of GABA is crucial for network synchronization. In addition, in immature GCs, oscillatory activity can be facilitated by the slow kinetics of $GABA_A$-mediated synaptic currents that may contribute to integrate incoming excitatory inputs (both GABAergic and glutamatergic) over a large time window (Draguhn and Heinemann, 1996; Hollrigel and Soltesz, 1997). In analogy with the synchronized activity generated in the disinhibited hippocampus (de la Prida et al., 2006), GDPs emerge when a sufficient number of cells fire and the excitability of the network attains a certain threshold within a restricted time window. Dye-coupling between immature GCs would facilitate this task.

Although neonatal and adult neurogenesis in the dentate gyrus seem to follow similar steps, the possibility that early synchronized activity early in postnatal development may play a role in synaptic wiring, thus contributing to refine local neuronal circuits according to aphorism "neurons that fire together wire together," cannot be excluded. Therefore, it is likely that changes in the environmental factors such as activity may determine the different phenotype of neonatal or adult GCs progenitors.

AUTHOR CONTRIBUTIONS

Andrea Pedroni, Antonello Mallamaci and Enrico Cherubini conceived and designed the experiments. Andrea Pedroni performed most of the electrophysiological and immunocytochemical experiments and analyzed the data. Do Duc Minh performed some immunocytochemical experiments. Enrico Cherubini wrote the paper with the approval of all the authors.

ACKNOWLEDGMENTS

The authors are particularly grateful to Drs R. Rauti and L. Ballerini for advice on biocytin morphological reconstruction; to Drs. R. Antonelli and F. Ruggeri for helpful comments and suggestions. This study was partially supported by a grant from Ministero dell'Istruzione, dell'Universita' e della Ricerca (PRIN 2011) to Enrico Cherubini.

REFERENCES

Altman, J., and Bayer, S. A. (1990a). Migration and distribution of two populations of hippocampal granule cell precursors during the perinatal and postnatal periods. *J. Comp. Neurol.* 301, 365–381. doi: 10.1002/cne.903010304

Altman, J., and Bayer, S. A. (1990b). Mosaic organization of the hippocampal neuroepithelium and the multiple germinal sources of dentate granule cells. *J. Comp. Neurol.* 301, 325–342. doi: 10.1002/cne.903010302

Ambrogini, P., Lattanzi, D., Ciuffoli, S., Agostini, D., Bertini, L., Stocchi, V., et al. (2004). Morpho-functional characterization of neuronal cells at different stages of maturation in granule cell layer of adult rat dentate gyrus. *Brain Res.* 1017, 21–31. doi: 10.1016/j.brainres.2004.05.039

Ben-Ari, Y., Cherubini, E., Corradetti, R., and Gaiarsa, J. L. (1989). Giant synaptic potentials in immature rat CA3 hippocampal neurones. *J. Physiol.* 416, 303–325.

Bergersen, L., Ruiz, A., Bjaalie, J. G., Kullmann, D. M., and Gundersen, V. (2003). GABA and GABAA receptors at hippocampal mossy fibre synapses. *Eur. J. Neurosci.* 18, 931–941. doi: 10.1046/j.1460-9568.2003.02828.x

Cabezas, C., Irinopoulou, T., Cauli, B., and Poncer, J. C. (2013). Molecular and functional characterization of GAD67-expressing, newborn granule cells in mouse dentate gyrus. *Front. Neural Circuits* 7:60. doi: 10.3389/fncir.2013.00060

Cabezas, C., Irinopoulou, T., Gauvain, G., and Poncer, J. C. (2012). Presynaptic but not postsynaptic GABA signaling at unitary mossy fiber synapses. *J. Neurosci.* 32, 11835–11840. doi: 10.1523/JNEUROSCI.5543-11.2012

Caiati, M. D., Sivakumaran, S., and Cherubini, E. (2010). In the developing rat hippocampus, endogenous activation of presynaptic kainate receptors reduces GABA release from mossy fiber terminals. *J. Neurosci.* 30, 1750–1759. doi: 10.1523/JNEUROSCI.4566-09.2010

Cherubini, E., Griguoli, M., Safiulina, V., and Lagostena, L. (2011). The depolarizing action of GABA controls early network activity in the developing hippocampus. *Mol. Neurobiol.* 43, 97–106 doi: 10.1007/s12035-010-8147-z

Crépel, V., Aronov, D., Jorquera, I., Represa, A., Ben-Ari, Y., and Cossart, R. (2007). A parturition-associated nonsynaptic coherent activity pattern in the developing hippocampus. *Neuron* 54, 105–120. doi: 10.1016/j.neuron.2007.03.007

de la Prida, L. M., Huberfeld, G., Cohen, I., and Miles, R. (2006). Threshold behavior in the initiation of hippocampal population bursts. *Neuron* 49, 131–142. doi: 10.1016/j.neuron.2005.10.034

Deng, W., Aimone, J. B., and Gage, F. H. (2010). New neurons and new memories: how does adult hippocampal neurogenesis affect learning and memory? *Nat. Rev. Neurosci.* 11, 339–350. doi: 10.1038/nrn2822

Draguhn, A., and Heinemann, U. (1996). Different mechanisms regulate IPSC kinetics in early postnatal and juvenile hippocampal granule cells. *J. Neurophysiol.* 76, 3983–3993.

Duan, X., Kang, E., Liu, C. Y., Ming, G. L., and Song, H. (2008). Development of neural stem cell in the adult brain. *Curr. Opin. Neurobiol.* 18, 108–115. doi: 10.1016/j.conb.2008.04.001

Espósito, M. S., Piatti, V. C., Laplagne, D. A., Morgenstern, N. A., Ferrari, C. C., Pitossi, F. J., et al. (2005). Neuronal differentiation in the adult hippocampus recapitulates embryonic development. *J. Neurosci.* 25, 10074–10086. doi: 10.1523/JNEUROSCI.3114-05.2005

Gruol, D. L., Deal, C. R., and Yool, A. J. (1992). Developmental changes in calcium conductances contribute to the physiological maturation of cerebellar Purkinje neurons in culture. *J. Neurosci.* 12, 2838–2848.

Gutierrez, R., Romo-Parra, H., Maqueda, J., Vivar, C., Ramìrez, M., Morales, M. A., et al. (2003). Plasticity of the GABAergic phenotype of the "glutamatergic" granule cells of the rat dentate gyrus. *J. Neurosci.* 23, 5594–5598.

Halliwell, J. V., and Adams, P. R. (1982). Voltage-clamp analysis of muscarinic excitation in hippocampal neurons. *Brain Res.* 250, 71–92. doi: 10.1016/0006-8993(82)90954-4

Hennou, S., Khalilov, I., Diabira, D., Ben-Ari, Y., and Gozlan, H. (2002). Early sequential formation of functional $GABA_A$ and glutamatergic synapses on CA1 interneurons of the rat foetal hippocampus. *Eur. J. Neurosci.* 16, 197–208. doi: 10.1046/j.1460-9568.2002.02073.x

Hollrigel, G. S., Ross, S. T., and Soltesz, I. (1998). Temporal patterns and depolarizing actions of spontaneous GABAA receptor activation in granule cells of the early postnatal dentate gyrus. *J. Neurophysiol.* 80, 2340–2351.

Hollrigel, G. S., and Soltesz, I. (1997). Slow kinetics of miniature IPSCs during early postnatal development in granule cells of the dentate gyrus. *J. Neurosci.* 17, 5119–5128.

Hsieh, J. (2012). Orchestrating transcriptional control of adult neurogenesis. *Genes Dev.* 26, 1010–1021. doi: 10.1101/gad.187336.112

Huguenard, J. R. (1996). Low-threshold calcium currents in central nervous system neurons. *Annu. Rev. Physiol.* 58, 329–348. doi: 10.1146/annurev.ph.58.030196.001553

Iwano, T., Masuda, A., Kiyonari, H., Enomoto, H., and Matsuzaki, F. (2012). Prox1 postmitotically defines dentate gyrus cells by specifying granule cell identity over CA3 pyramidal cell fate in the hippocampus. *Development* 139, 3051–3062. doi: 10.1242/dev.080002

Jones, S. P., Rahimi, O., O'Boyle, M. P., Diaz, D. L., and Claiborne, B. J. (2003). Maturation of granule cell dendrites after mossy fiber arrival in hippocampal field CA3. *Hippocampus* 13, 413–427. doi: 10.1002/hipo.10121

Kasper, E. M., Lübke, J., Larkman, A. U., and Blakemore, C. (1994). Pyramidal neurons in layer 5 of the rat visual cortex. III. Differential maturation of axon targeting, dendritic morphology, and electrophysiological properties. *J. Comp. Neurol.* 339, 495–518. doi: 10.1002/cne.903390404

Kasyanov, A. M., Safiulina, V. F., Voronin, L. L., and Cherubini, E. (2004). GABA-mediated giant depolarizing potentials as coincidence detectors for enhancing synaptic efficacy in the developing hippocampus. *Proc. Natl. Acad. Sci. U.S.A.* 101, 3967–3972. doi: 10.1073/pnas.0305974101

Laplagne, D. A., Espósito, M. S., Piatti, V. C., Morgenstern, N. A., Zhao, C., van Praag, H., et al. (2006). Functional convergence of neurons generated in the developing and adult hippocampus. *PLoS Biol.* 4:e409. doi: 10.1371/journal.pbio.0040409

Laplagne, D. A., Kamienkowski, J. E., Espósito, M. S., Piatti, V. C., Zhao, C., Gage, F. H., et al. (2007). Similar GABAergic inputs in dentate granule cells born during embryonic and adult neurogenesis. *Eur. J. Neurosci.* 25, 2973–2981. doi: 10.1111/j.1460-9568.2007.05549.x

Lavado, A., and Oliver, G. (2007). Prox1 expression patterns in the developing and adult murine brain. *Dev. Dyn.* 236, 518–524. doi: 10.1002/dvdy.21024

Liu, X., Tilwalli, S., Ye, G., Lio, P. A., Pasternak, J. F., and Trommer, B. L. (2000). Morphologic and electrophysiologic maturation in developing dentate gyrus granule cells. *Brain Res.* 856, 202–212. doi: 10.1016/S0006-8993(99)02421-X

Liu, Y. B., Lio, P. A., Pasternak, J. F., and Trommer, B. L. (1996). Developmental changes in membrane properties and postsynaptic currents of granule cells in rat dentate gyrus. *J. Neurophysiol.* 76, 1074–1088.

Marchal, C., and Mulle, C. (2004). Postnatal maturation of mossy fibre excitatory transmission in mouse CA3 pyramidal cells: a potential role for kainate receptors. *J. Physiol.* 561, 27–37. doi: 10.1113/jphysiol.2004.069922

Markwardt, S. J., Wadiche, J. I., and Overstreet-Wadiche, L. S. (2009). Input-specific GABAergic signaling to newborn neurons in adult dentate gyrus. *J. Neurosci.* 29, 15063–15072. doi: 10.1523/JNEUROSCI.2727-09.2009

McBain, C. J. (2008). Differential mechanisms of transmission and plasticity at mossy fiber synapses. *Prog. Brain Res.* 169, 225–240. doi: 10.1016/S0079-6123(07)00013-1

Menendez de la Prida, L., Bolea, S., and Sanchez-Andres, J. V. (1998). Origin of the synchronized network activity in the rabbit developing hippocampus. *Eur. J. Neurosci.* 10, 899–906. doi: 10.1046/j.1460-9568.1998.00097.x

Ming, G. L., and Song, H. (2011). Adult neurogenesis in the mammalian brain: significant answers and significant questions. *Neuron* 70, 687–702. doi: 10.1016/j.neuron.2011.05.001

Mullen, R. J., Buck, C. R., and Smith, A. M. (1992). NeuN, a neuronal specific nuclear protein in vertebrates. *Development* 116, 201–211.

Münster-Wandowski, A., Gómez-Lira, G., and Gutiérrez, R. (2013). Mixed neurotransmission in the hippocampal mossy fibers. *Front. Cell. Neurosci.* 7:210. doi: 10.3389/fncel.2013.00210

Overstreet, L. S., Hentges, S. T., Bumaschny, V. F., de Souza, F. S., Smart, J. L., Santangelo, A. M., et al. (2004). A transgenic marker for newly born granule cells in dentate gyrus. *J. Neurosci.* 24, 3251–3259. doi: 10.1523/JNEUROSCI.5173-03.2004

Overstreet-Wadiche, L. S., Bensen, A. L., and Westbrook, G. L. (2006). Delayed development of adult-generated granule cells in dentate gyrus. *J. Neurosci.* 26, 2326–2334. doi: 10.1523/JNEUROSCI.4111-05.2006

Overstreet-Wadiche, L. S., and Westbrook, G. L. (2006). Functional maturation of adult-generated granule cells. *Hippocampus* 16, 208–215. doi: 10.1002/hipo.20152

Safiulina, V. F., Caiati, M. D., Sivakumaran, S., Bisson, G., Migliore, M., and Cherubini, E. (2010). Control of GABA release at single mossy fiber-CA3 connections in the developing hippocampus. *Front. Syn. Neurosci.* 2:1. doi: 10.3389/neuro.19.001.2010

Safiulina, V. F., Fattorini, G., Conti, F., and Cherubini, E. (2006). GABAergic signaling at mossy fiber synapses in neonatal rat hippocampus. *J. Neurosci.* 26, 597–608. doi: 10.1523/JNEUROSCI.4493-05.2006

Schlessinger, A. R., Cowan, W. M., and Gottlieb, D. I. (1975). An autoradiographic study of the time of origin and the pattern of granule cell migration in the dentate gyrus of the rat. *J. Comp. Neurol.* 159, 149–175. doi: 10.1002/cne.901590202

Schmidt-Hieber, C., Jonas, P., and Bischofberger, J. (2004). Enhanced synaptic plasticity in newly generated granule cells of the adult hippocampus. *Nature* 429, 184–187. doi: 10.1038/nature02553

Schwarzer, C., and Sperk, G. (1995). Hippocampal granule cells express glutamic aci decarboxylase-67 after limbic seizures in the rat. *Neuroscience* 69, 705–709. doi: 10.1016/0306-4522(95)00348-M

Sivakumaran, S., Mohajerani, M. H., and Cherubini, E. (2009). At immature mossy-fiber-CA3 synapses, correlated presynaptic and postsynaptic activity persistently enhances GABA release and network excitability via BDNF and cAMP-dependent PKA. *J. Neurosci.* 29, 2637–2647. doi: 10.1523/JNEUROSCI.5019-08.2009

Sloviter, R. S., Dichter, M. A., and Rachinsky, T. L. (1996). Basal expression and induction of glutamate decarboxylase and GABA in excitatory granule cells of the rat and monkey hippocampal dentate gyrus. *J. Comp. Neurol.* 373, 593–618. doi: 10.1002/(SICI)1096-9861(19960930)373:4<593::AID-CNE8>3.0.CO;2-X

Spigelman, I., Zhang, L., and Carlen, P. L. (1992). Patch-clamp study of postnatal development of CA1 neurons in rat hippocampal slices: membrane excitability and K+ currents. *J. Neurophysiol.* 68, 55–69.

Walker, M. C., Ruiz, A., and Kullmann, D. M. (2001). Monosynaptic GABAergic signaling from dentate to CA3 with a pharmacological and physiological profile typical of mossy fiber synapses. *Neuron* 29, 703–715. doi: 10.1016/S0896-6273(01)00245-8

Ye, G. L., Song Liu, X., Pasternak, J. F., and Trommer, B. L. (2000). Maturation of glutamatergic neurotransmission in dentate gyrus granule cells. *Brain Res. Dev. Brain Res.* 124, 33–42. doi: 10.1016/S0165-3806(00)00103-6

Zander, J.-F., Munster-Wandowski, A., Brunk, I., Pahner, I., Gómez-Lira, G., Heinemann, U., et al. (2010). Synaptic and vesicular coexistence of VGLUT and VGAT in selected excitatory and inhibitory synapses. *J. Neurosci.* 30, 7634–7645. doi: 10.1523/JNEUROSCI.0141-10.2010

Zhao, S., Zhou, Y., Gross, J., Miao, P., Qiu, L., Wang, D., et al. (2010). Fluorescent labeling of newborn dentate granule cells in GAD67-GFP transgenic mice: a genetic tool for the study of adult neurogenesis. *PLoS ONE* 5:e12506. doi: 10.1371/journal.pone.0012506

Conflict of Interest Statement: The authors declare that the research was conducted in the absence of any commercial or financial relationships that could be construed as a potential conflict of interest.

Received: 20 December 2013; accepted: 30 January 2014; published online: 14 February 2014.

Citation: Pedroni A, Minh DD, Mallamaci A and Cherubini E (2014) Electrophysiological characterization of granule cells in the dentate gyrus immediately after birth. Front. Cell. Neurosci. ***8****:44. doi: 10.3389/fncel.2014.00044*

This article was submitted to the journal Frontiers in Cellular Neuroscience.

nature COMMUNICATIONS

ARTICLE

Received 4 Jun 2014 | Accepted 25 Aug 2014 | Published 9 Oct 2014

DOI: 10.1038/ncomms6066 OPEN

Pin1-dependent signalling negatively affects GABAergic transmission by modulating neuroligin2/gephyrin interaction

Roberta Antonelli[1], Rocco Pizzarelli[1], Andrea Pedroni[1], Jean-Marc Fritschy[2], Giannino Del Sal[3,4], Enrico Cherubini[1,5] & Paola Zacchi[1]

The cell adhesion molecule Neuroligin2 (NL2) is localized selectively at GABAergic synapses, where it interacts with the scaffolding protein gephyrin in the post-synaptic density. However, the role of this interaction for formation and plasticity of GABAergic synapses is unclear. Here, we demonstrate that endogenous NL2 undergoes proline-directed phosphorylation at its unique S714-P consensus site, leading to the recruitment of the peptidyl-prolyl *cis–trans* isomerase Pin1. This signalling cascade negatively regulates NL2's ability to interact with gephyrin at GABAergic post-synaptic sites. As a consequence, enhanced accumulation of NL2, gephyrin and $GABA_A$ receptors was detected at GABAergic synapses in the hippocampus of Pin1-knockout mice (Pin1 $-/-$) associated with an increase in amplitude of spontaneous $GABA_A$-mediated post-synaptic currents. Our results suggest that Pin1-dependent signalling represents a mechanism to modulate GABAergic transmission by regulating NL2/gephyrin interaction.

[1] Department of Neuroscience, International School for Advanced Studies (SISSA), via Bonomea 265, 34136 Trieste, Italy. [2] Institute of Pharmacology and Toxicology, University of Zurich, Winterthurerstrasse 190, 8057 Zurich, Switzerland. [3] Laboratorio Nazionale del Consorzio Interuniversitario per le Biotecnologie (LNCIB), Padriciano 99, 34012 Trieste, Italy. [4] Dipartimento di Scienze della vita, Universita' degli Studi di Trieste, Trieste, Italy. [5] European Brain Research Institute (EBRI), via del Fosso di Fiorano 64, 00143 Rome, Italy. Correspondence and requests for materials should be addressed to P.Z. (email: zacchi@sissa.it).

Structural and functional changes of post-synaptic density (PSD) components contribute to regulate synapse formation and plasticity. These remodelling events can affect trafficking, lateral mobility and turnover of several classes of structural and signalling molecules. They often involve interactions among specific proteins regulated by post-translational modifications, such as phosphorylation. At GABAergic synapses, the impact of phosphorylation on the gating properties, surface mobility and trafficking of the gamma-aminobutyric acid A receptors ($GABA_A$Rs) has been extensively studied[1,2]. Much less is known about the effects of phosphorylation of other post-synaptic proteins functionally linked to $GABA_A$Rs.

An important class of molecules involved in synapse formation, maturation and stabilization comprizes the cell adhesion molecules of the neuroligin (NLs) family[3]. These post-synaptic proteins functionally coordinate pre and post-synaptic rearrangements by binding, via their extracellular domain, the presynaptically localized neurexins (NRXs) and via specific intracellular motifs, synapse-specific scaffolding molecules[4–6]. Neuroligin2 (NL2) isoform is the only known adhesion molecule constitutively present at GABAergic PSDs[7], where it drives the recruitment of inhibitory neurotransmitter receptors as well as the scaffolding molecule gephyrin[6]. Gephyrin, initially identified as a constituent of purified glycine receptor preparations (GlyR)[8,9], was soon recognized a key player in α2 and γ2 subunit-containing $GABA_A$Rs clustering[10,11] and to be a central component of the GABAergic (and glycinergic) PSD[8,12]. On the basis of its auto-oligomerization properties, gephyrin builds a bidimensional lattice underneath the synaptic membrane, which exposes a high number of binding sites to accumulate GlyR and $GABA_A$Rs in front of the presynaptic releasing sites[13–17].

NL2 interacts with gephyrin through a conserved stretch of amino acid residues highly conserved among all family members[6]. Site-directed mutagenesis within this binding module identified a specific tyrosine residue (Y770A) whose alanine substitution impairs NL2 ability to recruit recombinant and endogenous gephyrin to post-synaptic sites[6]. Notably, the corresponding tyrosine residue on NL1, the isoform enriched at excitatory synapses, was found to be phosphorylated *in vivo*, preventing NL1–gephyrin interaction while favouring PSD95 recruitment at excitatory synapses[18]. Altogether, these findings point to the existence of intracellular signalling mechanisms able to modulate NL-scaffolding protein interactions by modifying specifically NL properties, leading to alteration in excitatory and inhibitory synaptic transmission.

In the present study, we have investigated whether post-phosphorylation prolyl-isomerization may affect GABAergic transmission in a similar manner. This signalling cascade targets serine and threonine residues preceding a proline residue to promote conformational changes on its substrate[19]. This effect is achieved by a unique enzyme, peptidyl-prolyl isomerase Pin1, whose catalytic activity facilitates the *cis–trans* isomerization of the peptide bond[20,21]. Notably, Pin1 was found to interact with gephyrin and to alter its overall conformation, thus enhancing its ability to bind the GlyR[22].

Here, we provide evidence that endogenous NL2 can be phosphorylated at its unique Pin1 consensus motif thus rendering it able to physically recruit the phospho-specific effector Pin1. We show that post-phosphorylation prolyl-isomerization can regulate NL2's ability to complex with gephyrin. Specifically, Pin1-mediated propyl-isomerization of phosphorylated serine 714 negatively modulates NL2–gephyrin complex formation, down-regulating GABAergic synaptic transmission.

Results

Endogenous NL2 undergoes proline-directed phosphorylation. The cytoplasmic domain (CD) of NL2 possesses a unique consensus motif for proline-directed phosphorylation, S714-P, located 15 amino acids apart from the transmembrane domain (Fig. 1a). To assess whether this site can undergo phosphorylation *in vivo* we used the mitotic phosphoprotein monoclonal 2 (MPM2) antibody that specifically recognizes phosphorylated S/T-P motifs (Davis *et al.*[23]). Endogenous NL2 was therefore immunoprecipitated from mouse brain homogenates using an affinity-purified polyclonal antibody raised against its CD or normal mouse IgG as negative control. Western blotting using the MPM2 antibody revealed a band at around 120 kDa that corresponds to the upper band of the doublet recognized by the NL2 antibody in parallel immunoprecipitation experiments (Fig. 1b), suggesting that at least a fraction of NL2 can be phosphorylated at its unique Pin1 consensus motif. To demonstrate that phosphorylation at serine 714 is the event responsible for NL2 detection by the MPM2 antibody, we generated the phospho-defective point mutant NL2HA-S714A. This mutation was introduced into a NL2HA hampered in gephyrin binding (NL2HA-S714A-ΔgephyrinBD, GBD) (see Supplementary Fig. 1), to exclude the possibility that the MPM2 antibody would immune-react with phosphorylated Pin1 consensus motifs on endogenous gephyrin, which is, at the same time, a Pin1 target[22] and an interacting partner of NL2 (ref. 6). Under these conditions, the MPM2 antibody efficiently immunoprecipitated only NL2HA-ΔGBD but not the corresponding point mutant, as indicated by the anti-HA immunoblot (Fig. 1c), thus demonstrating that S714 can be found phosphorylated on NL2.

The essential feature of proline-directed phosphorylation as a signalling mechanism relies on the ability of phosphorylated S/T-P motifs to recruit the prolyl isomerase Pin1 (refs 19,24). To test whether this unique phospho-epitope is able to recruit the effector molecule of the signalling cascade, we performed co-immunoprecipitation experiments from Pin1 +/+ and Pin1 −/− brain lysates. This approach unveiled that Pin1 can be detected in NL2, but not in control, immunoprecipitates or in the absence of Pin1 expression (Fig. 1d). To exclude the possibility that Pin1 co-precipitated by NL2 is bound to endogenous gephyrin, these assays were performed on co-expression of NL2HA-ΔGBD and Pin1-FLAG in HEK293 cells. Cell lysates were immunoprecipitated with the anti-FLAG antibody and bound protein complexes analysed by western blotting using anti-HA and anti-FLAG antibodies for NL2 and Pin1 detection, respectively. As shown in Fig. 1e, while NL2HA-ΔGBD was still able to be immunoprecipitated from cells expressing Pin1-FLAG, S714 to alanine mutagenesis completely abolished such interaction, indicating that S714 represents a newly identified Pin1 target.

Pin1 modulates gephyrin–NL2 interaction. The observation that two fundamental components of the GABAergic PSD are both targets of proline-directed phosphorylation prompted us to investigate whether such signalling cascade would modulate their interaction. To this end, we initially co-expressed gephyrin-FLAG and NL2HA in HEK293 cells and examined the amount of NL2HA that complex with gephyrin-FLAG at 48 h after treating the cells with the selective and reversible inhibitor of Pin1 isomerase activity PiB (IC_{50} of approximately 1.5 μM) (ref. 25). As shown in Fig. 2a, even though the anti-FLAG antibody immunoprecipitated comparable amounts of gephyrin-FLAG, a significant increase (64%) in the amount of co-precipitated NL2HA was observed on PiB treatment as compared with

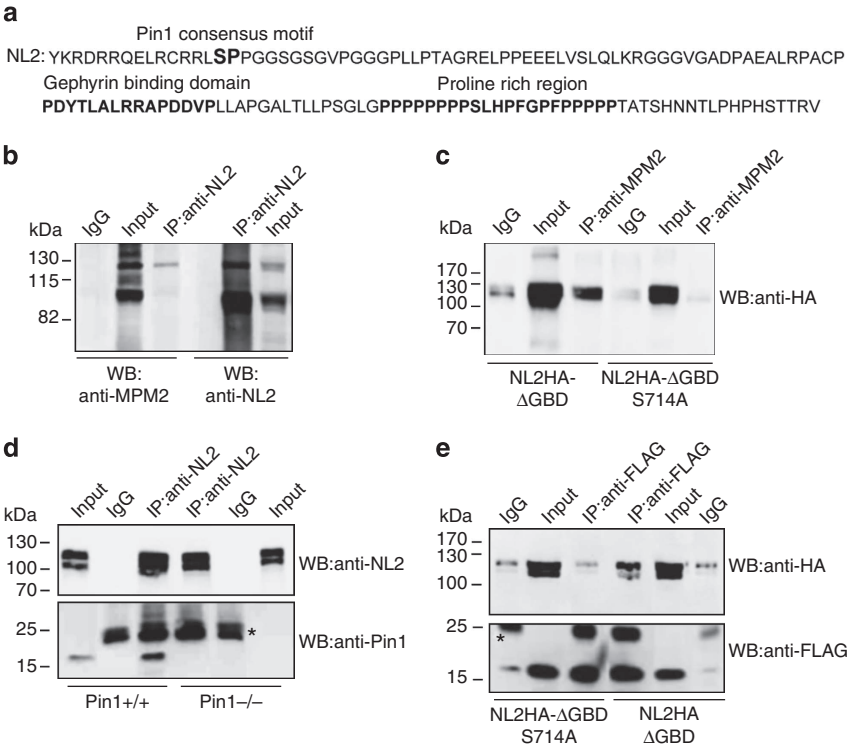

Figure 1 | NL2 is a proline-directed substrate. (**a**) Amino acid sequence of the NL2 CD. In bold is marked the unique Pin1 consensus motif (S714-P). The gephyrin-binding domain and the proline-rich region are highlighted in bold. (**b**) Representative immunoblotting of endogenous NL2 immunoprecipitated (IP) from mouse brain and probed with the anti-MPM2 that specifically recognizes phosphorylated S/T-P motifs and anti-NL2. Rabbit IgGs were used as negative control (IgG) ($n=4$). (**c**) Representative immunoblotting of overexpressed NL2HA lacking the gephyrin binding domain (NL2HA-ΔGBD) and the corresponding point mutant (NL2HA-ΔGBDSer714Ala) immunoprecipitated by the phospho-specific MPM2 antibody. Western blot analysis was carried out with anti-HA monoclonal antibody. Mouse IgGs were used as negative control ($n=5$). (**d**) Co-immunoprecipitation (Co-IP) of endogenous NL2 and Pin1 from DSP cross-linked brain homogenates of Pin1+/+ or Pin1−/− mice. Western blots were performed with anti-NL2 polyclonal and anti-Pin1 monoclonal antibodies. Mouse IgGs were used as negative control. Asterisk indicate the IgG light chains ($n=6$). (**e**) FLAG epitopes from cross-linked samples of HEK293 cells co-expressing Pin1-FLAG and NL2HA-ΔGBD or NL2HA-ΔGBDS714 were immunoprecipitated by anti-FLAG antibody. Western blot was performed with anti-HA and anti-FLAG monoclonal antibodies. Mouse IgGs were used as negative control ($n=4$). Full images of western blots are in Supplementary Fig. 5.

mock-treated cells (dimethylsulfoxide, DMSO). Interestingly, a marked increase (140%) was detected on gephyrin-FLAG co-precipitation by NL2HA-S714A as compared with NL2HA, indicating that Pin1 exerts a negative control on NL2–gephyrin complex formation, at least in part, through NL2 prolyl-isomerization (Fig. 2b).

This issue was then investigated using a source of native NL2–gephyrin complexes mouse brain homogenates from both genotypes. For these experiments, endogenous NL2 was immunoprecipitated using a rabbit polyclonal anti-NL2 antibody and the co-precipitated gephyrin fraction was visualized by the monoclonal 3B11 antibody (Fig. 2c). In the absence of Pin1 expression, the amount of gephyrin co-precipitated by NL2 was increased by 40% as compared with Pin1 expressing neurons. This approach was also applied on hippocampal tissues isolated from both mouse genotypes. Here, the enrichment of gephyrin co-precipitated by NL2 in the absence of Pin1 expression was even more dramatic as compared with the amount detected from whole brain (130% increase; Fig. 2d), suggesting a strong impact of such signalling pathway on GABAergic synapses of the hippocampus.

Characterization of gephyrin Pin1 sites S270-P and S319-P. The scaffolding molecule gephyrin possesses 10 putative Pin1 consensus motifs, the majority of them being concentrated in the central region (C-domain)[26]. To determine whether specific Pin1 sites may contribute to enhance NL2/gephyrin complex formation, we decided to focus on those located close to, or within, the NL2 binding site on gephyrin. A previous yeast two-hybrid screening identified a large portion of gephyrin encompassing the E-domain and part of the C-domain as the region involved in NL2 interaction[6]. We re-examine this issue by generating eGFP-tagged gephyrin truncated version to be tested in GST-NL2-CD pulldown assays. HEK293 cells transfected with different eGFP-gephyrin variants were incubated with GST-NL2-CD loaded beads or with GST alone as negative controls. As shown in Fig. 3a, while gephyrin 310–736 was recruited even better than the wild-type (WT) version, the mutants gephyrin 326–736 and gephyrin 1–310 (gephyrin GC) displayed a reduced binding activity as compared to both gephyrin full-length (FL) and the truncated version 310–736 (Fig. 3a). Since the two E-domain gephyrin versions, showing such a striking difference in the binding affinity, differ only for a short stretch of amino acids, we generated the deletion mutant removing, from the FL protein, only the residues contained in this region but belonging to the E-domain itself (gephyrinΔ319–329) and assayed it for NL2 binding. Interestingly, the lack of this short sequence almost completely abolished the interaction of gephyrin with NL2 (Fig. 3b), indicating that epitope(s) contained in the C-domain together with this minimal binding module are involved in gephyrin recruitment.

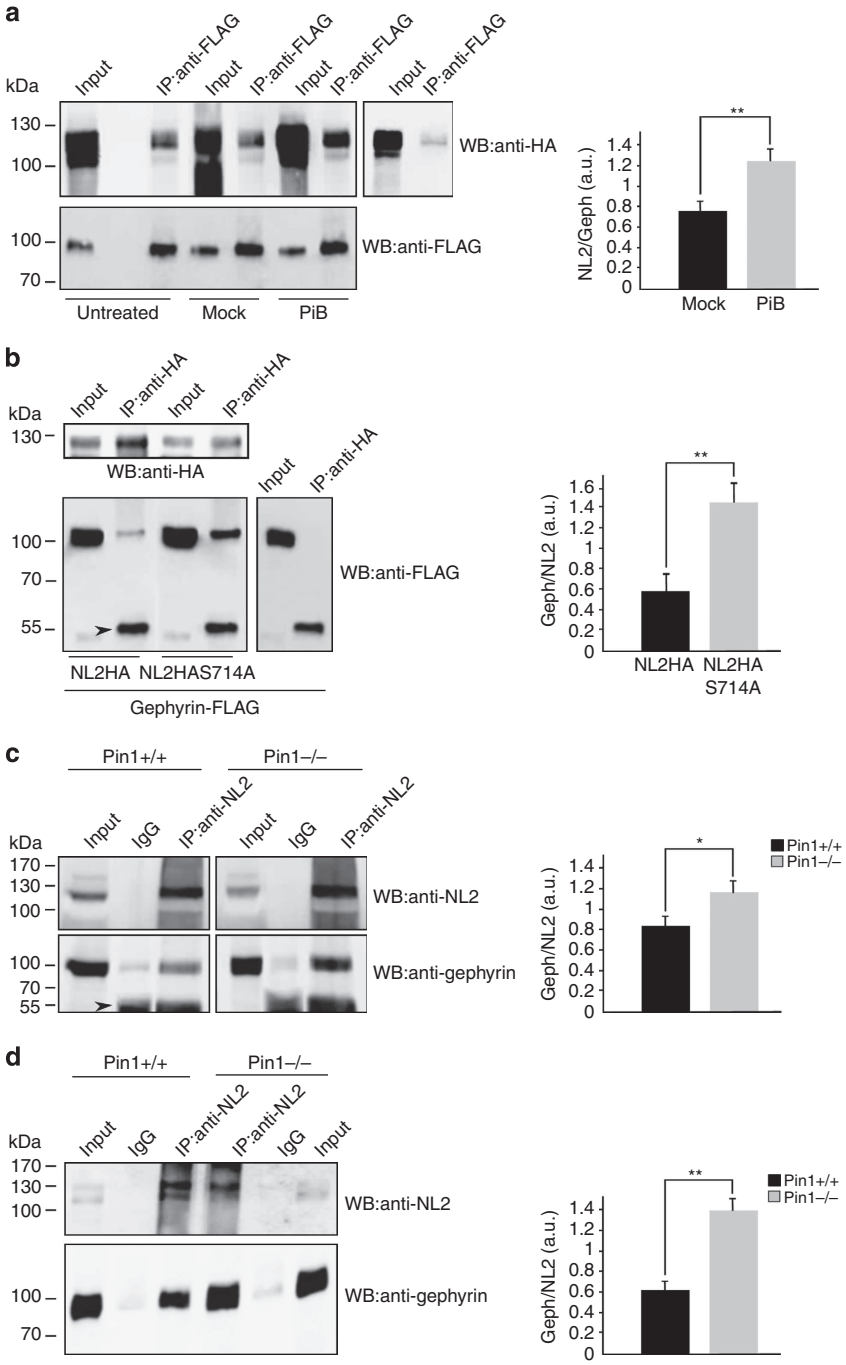

Figure 2 | Pin1 negatively modulates NL2/gephyrin interaction. (**a**) Representative IP of FLAG epitopes from samples of HEK293 cells co-expressing gephyrin-FLAG and NL2HA and treated for 48 h with PiB 2.5 μM, DMSO (mock) or untreated. IP was also performed on NL2HA single transfected cells as a negative control. Nitrocellulose membranes were probed with anti-HA and anti-FLAG antibodies. The histogram on the right shows the relative amount of NL2 co-precipitated by gephyrin-FLAG in control and PiB treated cells obtained from densitometric analysis ($n=5$, mean values ± s.d., $^{**}P<0.001$, Student's *t*-test). (**b**) Lysates of HEK cells transfected with gephyrin-FLAG in the presence of NL2HA or NL2HA-S714A or with gephyrin alone (as a negative control) were immunoprecipitated with anti-HA agarose. Immunoprecipitates were analysed by western blotting using anti-FLAG and anti-HA monoclonal antibodies. Arrowhead indicates the IgG heavy chains. The histogram on the right shows the relative amount of gephyrin-FLAG in complex with either NL2HA or NL2HA-S714A co-precipitated by anti-HA agarose obtained from densitometric analysis ($n=5$, mean values ± s.d., $^{**}P<0.001$, Student's *t*-test). (**c**) Co-IP of endogenous NL2/gephyrin complexes from DSP cross-linked brain homogenates of Pin1+/+ or Pin1−/− mice. Western blots were performed with anti-NL2 polyclonal and anti-gephyrin monoclonal antibodies. Rabbit IgGs were used as negative control. An increased amount of gephyrin co-precipitates in complex with NL2 in the absence of Pin1 expression. Arrowhead indicates the IgG heavy chains. The histogram on the right shows the relative amount (obtained from densitometric analysis) of endogenous gephyrin co-precipitated by endogenous NL2 from both mouse genotypes ($n=8$, mean values ± s.d., $^{*}P<0.01$, Student's *t*-test). (**d**) A similar experiment described in **c** was carries out on hippocampus isolated from of Pin1+/+ or Pin1−/− mice. The histogram on the right shows the relative amount (obtained from densitometric analysis) of endogenous gephyrin co-precipitated by endogenous NL2 from both mouse genotypes ($n=4$, mean values ± s.d., $^{**}P<0.001$, Student's *t*-test). Full images of western blots are in Supplementary Fig. 5.

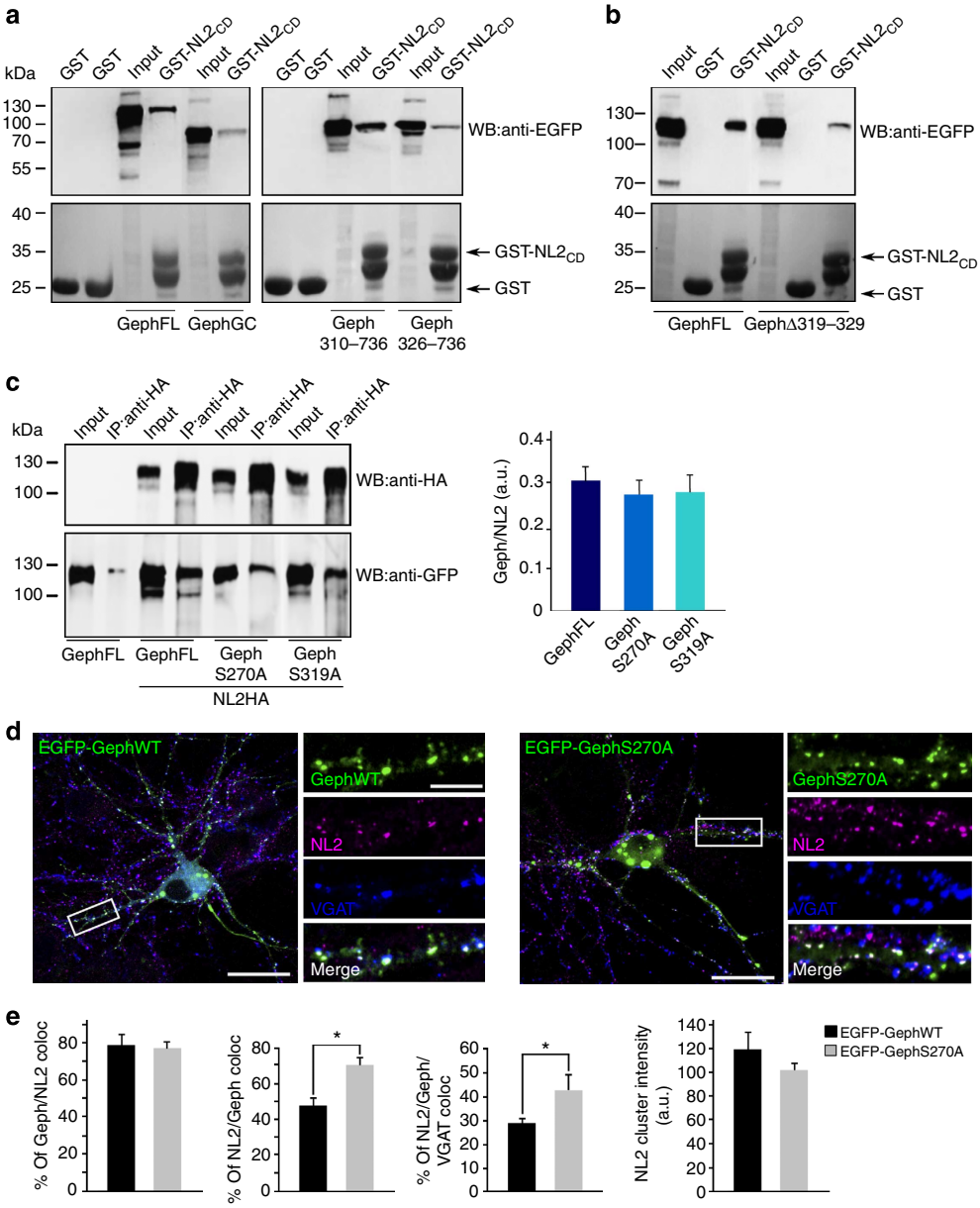

Figure 3 | Impact of gephyrin S270A and S319A in NL2/gephyrin interaction. (**a**) GST-NL2-CD pulldown from samples of HEK293 expressing EGFP-gephyrin full-length (FL), EGFP-gephyrin 310–736 (E-310), EGFP-gephyrin 326–736 (E-326) and EGFP-gephyrin GC. GST was used as negative control. Pulled down eGFPgephyrin variants were detected using an anti-GFP monoclonal antibody. The bottom panels show the levels of GST and GST-NL2-CD in the pulldown assays (Ponceau staining) ($n=8$). (**b**) EGFP-gephyrin Δ319 to 329 was tested in similar pulldown assays. Western blots in **a** and **b** were performed using anti-GFP antibody. Gephyrin requires amino acid sequence 319–329 for its efficient recruitment by NL2 ($n=6$). (**c**) Representative IP of HA epitopes from samples of HEK293 cells co-expressing NL2HA and EGFP-gephyrin WT, EGFP-gephyrinS270A or EGFP-gephyrinS319A. Nitrocellulose membranes were probed with anti-HA and anti-GFP antibodies. EGFP-gephyrin single transfected cells incubated with HA agarose were used as negative controls. The histogram on the right shows the relative amount of eGFP-gephyrinWT and point mutants co-precipitated by NL2HA ($n=4$, mean values ± s.d., $P>0.05$). (**d**) Representative images of hippocampal neurons transfected with EGFP-gephyrin and EGFP-gephyrinS270A point mutant immunolabeled for endogenous NL2 (magenta) and VGAT (blue) at DIV10. Enlarged boxed areas are shown aside to the corresponding full view image. Post-synaptic clustering is demonstrated by apposition of gephyrin/NL2 clusters to VGAT positive terminals on the merge window. Scale bars, 20 µm in full view images and 5 µm in enlarged panels. (**e**) Distribution histograms of the % of gephyrin clusters colabeled with NL2 (79 ± 5% in EGFP-gephyrinWT versus 77 ± 4% in EGFP-gephyrinS270A), % of NL2 clusters colabeled with gephyrin (48 ± 5% in EGFP-gephyrinWT versus 71 ± 4% in EGFP-gephyrinS270A), % of NL2 synaptically localized (29 ± 2% in EGFP-gephyrinWT versus 43 ± 6% in EGFP-gephyrinS270A) and NL2 clusters intensity (119 ± 15 a.u. in EGFP-gephyrinWT versus 102 a.u. ± 6 in EGFP-gephyrinS270A). The number of transfected hippocampal neurons investigated in each experiments (four independent experiments) were as follow: $n=15$ for eGFP-gephyrinWT, $n=10$ for eGFP-gepyrinS270A (for each neurons at least 4 dendritic regions of interests were measured, mean values ± s.d., $^*P<0.01$, Student's *t*-test).

On the basis of these results, two Pin1 consensus sites were further characterized, namely S319-P, located at the edge of the minimal binding module, and S270-P, positioned in its proximity, still contained, in the C-domain participating in NL2 binding. To this end, we introduced point mutations in eGFP-gephyrin to create S319A and S270A mutants and tested them for their ability

to interact with NL2HA. As judged by co-immunoprecipitation experiments, no significant differences were observed in binding capacity of the mutants as compared with gephyrin WT (Fig. 3c). These constructs were also overexpressed in cultured hippocampal neurons to analyse and quantify their impact on endogenous NL2 distribution using immunofluorescence staining and confocal microscopy. As previously reported, neurons expressing the S270A mutants had an increased number, unchanged in size, of gephyrin clusters compared with eGFP-gephyrin WT[27] (18.9 ± 1.7 per 20 µm dendritic segment versus 6.5 ± 0.6, $P = 0.00015$). The expression of the S319A construct produced a dramatic decrease in cluster density associated with a diffuse cytoplasmic staining. This latter effect seems to correlate with the intrinsic instability of the mutant protein that undergoes a high rate of degradation on neuronal expression (data not shown), hampering its further characterization. Clusters formed by gephyrin S270A co-localized with NL2 at the same extent as the WT protein (around 78%; Fig. 3d,e). The fraction of NL2 clusters co-localizing with S270A mutant as well as their synaptic localization were increased as compared with gephyrin WT but their intensity values (calculated by normalizing cluster fluorescence intensity to cluster area and expressed in a.u.: 119 a.u. ± 15.2 versus 102 ± 6.3) were unchanged (Fig. 3e). These data indicate that the increase in NL2/gephyrin S270 interaction observed by immunoprecipitation is simply due to the augmented S270A cluster density and not to an enhance affinity of the mutant for NL2.

Pin1 selectively controls NL2 synaptic enrichment. Pin1 has emerged as a negative regulator of gephyrin–NL2 interaction. Since these protein complexes are mainly localized at the plasma membrane, we tested whether Pin1 affects the amount of NL2 transported to, or maintained at, the neuronal plasma membrane. To this end, cultured hippocampal neurons derived from Pin1 +/+ and Pin1 −/− mice were subjected to surface biotinylation assay. Cell surface proteins were treated with the membrane-impermeant sulfo-NHS-biotin reagent, then isolated by binding to Streptavidin beads and probed with anti-NL2 antibody. To check for unspecific protein binding during surface biotinylation experiments, hippocampal neurons not labelled with biotin were processed with biotinylated samples. Western blot detecting the intracellular glycophosphatidylinositol-anchored protein Flotilin1 was included to ensure that similar amount of associated membrane proteins, biotinylated or not, where incubated with Streptavidin beads. No major differences on the total content of membrane localized NL2 were observed between Pin1 +/+ and Pin1 −/− (Fig. 4a).

These results allow excluding the involvement of Pin1 in NL2 transport and/or turnover at the plasma membrane. Surface biotinylation represents an experimental approach that cannot provide an accurate analysis of protein distributions among different membrane domains. Since NL2 is enriched at GABAergic synapses, but is also distributed on extrasynaptic sites[28], with

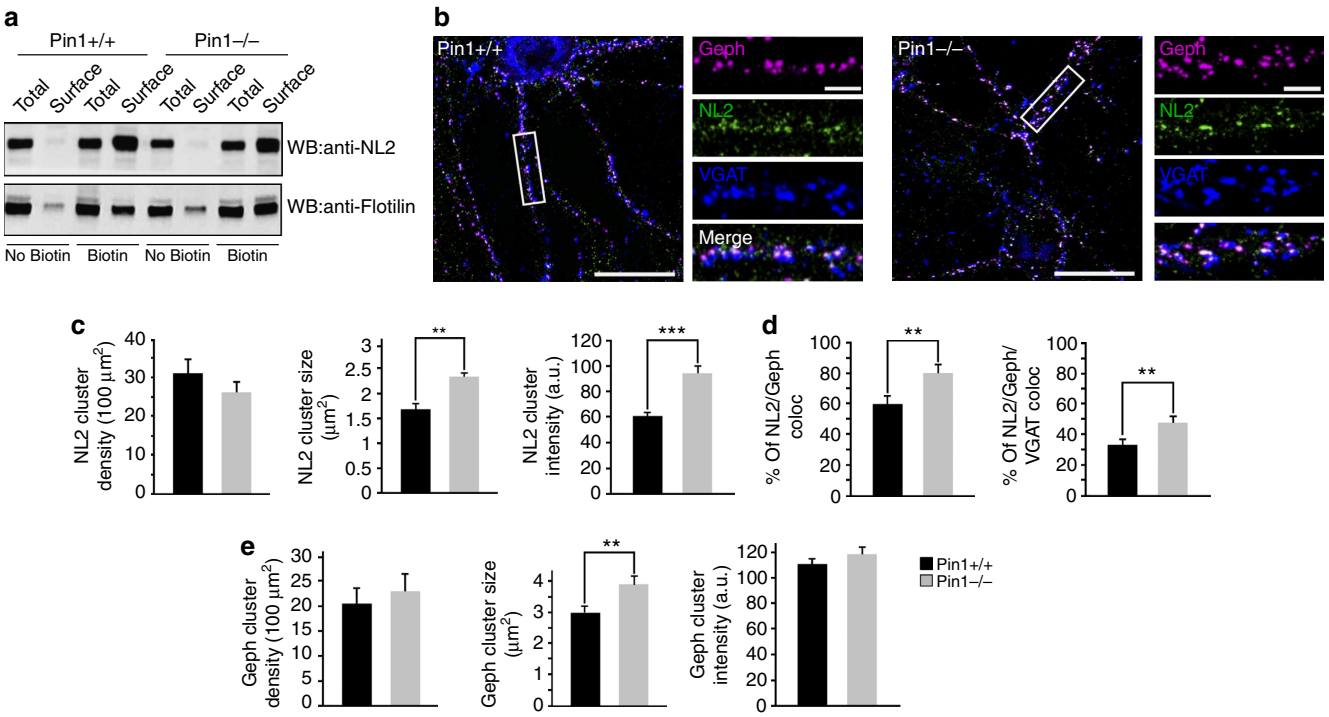

Figure 4 | Pin1 enhances NL2 synaptic content not its surface abundance. (**a**) Surface NL2 derived from cultured hippocampal neurons of Pin1 +/+ and Pin1 −/− mice was isolated by biotinylation assay and detected by anti-NL2 antibody. No biotinylated neuronal cells were processed in parallel to evaluate unspecific NL2 binding. Western blot detecting glycophosphatidylinositol-anchored Flotilin was used as loading control ($n = 4$). Full images of western blots are in Supplementary Fig. 5. (**b**) Typical examples of hippocampal neurons from Pin1 +/+ and Pin1 −/− immunolabeled for endogenous gephyrin (magenta), NL2 (green) and VGAT (blue) at DIV10. Enlarged boxed areas are shown aside to the corresponding full view image. Post-synaptic clustering is demonstrated by apposition of gephyrin/NL2 clusters to VGAT positive terminals on the merge window. Scale bars, 20 µm in full view images and 5 µm in enlarged panels. (**c**) Distribution histograms of NL2 cluster density (normalized to 100 µm²), the average cluster size and intensity in Pin1 +/+ and Pin1 −/− hippocampal neurons. (**d**) Distribution histograms of the percentage of NL2 co-localizing with gephryin and the percentage of double labelled NL2/gephyrin puncta overlapping with the presynaptic marker VGAT. (**e**) Distribution histograms of gephyrin cluster density (normalized to 100 µm²), the average cluster size and intensity (calculated as described in **c**) in both mouse genotypes. The number of hippocampal neurons investigated in each experiments (three independent experiments) were as follows: $n = 10$ for Pin1 +/+, $n = 12$ for Pin1 −/−. For each neurons, at least five dendritic regions of interests were measured, mean values ± s.d., $^{**}P < 0.001$, $^{***}P < 0.0001$, Student's t-test).

this approach differences in NL2 partitioning between these two compartments might have been missed.

To this aim, immunocytochemical experiments were performed in dissociated Pin1 +/+ and Pin1 −/− hippocampal neurons co-labelled for NL2, gephyrin and VGAT, a specific marker of GABAergic innervations[29] (Fig. 4b). In the absence of Pin1 expression a significant increase in NL2 cluster size (2.4 μm² ± 0.2 versus 1.7 μm² ± 0.2, $P = 0.00044$) and intensity (92 a.u. ± 4.0 versus 58 a.u. ± 2, $P < 0.00048$) was observed as compared with WT neurons, while no major changes in NL2 cluster density were detected (Fig. 4c). The fraction of NL2-positive clusters co-localized with endogenous gephyrin puncta was also enhanced in Pin1 −/− cells (80 ± 3.0% versus 60 ± 5%, $P = 0.00013$) and found enriched at post-synaptic sites, as demonstrated by the higher percentage of NL2/gephyrin co-stained puncta overlapping with the presynaptic marker VGAT (48 ± 4% versus 33 ± 4%, $P = 0.0008$; Fig. 4d). Gephyrin puncta appeared slightly, but significantly, increased in size while their density and intensity values were unchanged as compared with Pin1 +/+ (Fig. 4e). These observations suggest that the absence of Pin1 promotes the formation and/or stabilization of NL2/gephyrin complexes at GABAergic post-synaptic sites.

NL2/gephyrin complex modulates synaptic abundance of $GABA_A$Rs. The recruitment of $GABA_A$Rs at synaptic sites is functionally coupled to NLs expression levels as well as to the gephyrin scaffold[6]. To assess whether the enhanced NL2/gephyrin complex formation detected at GABAergic synapses similarly affects the distribution of synaptic γ2 subunit-containing $GABA_A$Rs, we performed a quantitative evaluation of the γ2 subunit present in synaptosome suspensions isolated from the hippocampus of Pin1 +/+ and Pin1 −/− mice. Quantitative immunoblot analysis was also extended to NL2 and gephyrin to further verify their synaptic enrichment. As shown in Fig. 5a, the amount of all three markers investigated was significant increased in Pin1 −/− mice as compared with Pin1 +/+. The synaptic enrichment (synaptic fraction versus homogenate) was 35 ± 5% for the NL2, 30 ± 6% for the γ2 subunit and 20 ± 4% for gephyrin.

We also examined the number of puncta labelled for gephyrin and γ2 subunit-specific antibodies, as well as their levels of colocalization with the presynaptic marker VGAT, in the CA1 region of the hippocampus of both genotypes. The staining pattern of gephyrin in Pin1 −/− demonstrated a slight increase in the number of clusters both in the stratum oriens (SO) and stratum radiatum (SR) as compared with Pin1 +/+ (SO 16 ± 3 clusters per 100 μm² and SR 28 ± 3 clusters per 100 μm² versus SO 10 ± 2 clusters per 100 μm² and SR 19 ± 3 clusters per 100 μm²; $P < 0.05$; Fig. 5b,c). This increase was paralleled by a small increase (around 6–8%) in gephyrin puncta co-localized with presynaptic VGAT (SO 30 ± 2% and SR 39 ± 1.4% versus SO 24 ± 2% and SR 31 ± 2%; $P < 0.05$; Fig. 5b,c). The average cluster size and intensity were similar in both genotypes (3.6 μm² ± 0.2 versus 3.5 μm² ± 0.3 and 61 ± 7 versus 65 ± 4 a.u. for cluster size and intensity in Pin1 −/− versus Pin1 +/+, respectively).

The γ2 subunit staining pattern exhibited a similar cluster density in the two strata analysed in both genotypes (SO 8 ± 2 and SR 18 ± 2 versus SO 8 ± 1 and SR 17 ± 1.2; $P > 0.05$; Fig. 5d,e). A small, although significant, increase in their intensity was evident (120 ± 3 RFU versus 106 ± 2 RFU in Pin1 −/− versus Pin1 +/+; $P < 0.05$) but they were similar in size (4.3 μm² ± 0.5 versus 3.7 μm² ± 0.5). VGAT colocalization was increased by 10–15% in tissue from knockout animals (SO 38.9 ± 2.7% and SR 52 ± 3% versus SO 29 ± 2% and SR 36 ± 3%; $P < 0.05$; Fig. 5d,e). The changes in gephyrin and γ2 subunit synaptic fraction are not due to an increase in synapses numbers, the density of inhibitory terminals being unaltered between the two genotypes, as assessed by quantification of VGAT immunolabeling (SO 14 ± 2% and SR 22 ± 3% versus SO 13 ± 2% and SR 21 ± 3%; $P > 0.05$).

Altogether, these data indicate that the enhanced interaction between gephyrin and NL2 observed in the absence of Pin1 is associated with a concomitant increase in the synaptic recruitment of γ2 subunit-containing $GABA_A$Rs.

Pin1 signalling affects the number of synaptic $GABA_A$Rs. To functionally explore whether the enrichment of γ2 subunit-containing $GABA_A$Rs in Pin1 −/− mice affects GABAergic transmission, whole-cell recordings in voltage clamp configuration were performed from CA1 principal cells in hippocampal slices obtained from Pin1 +/+ and Pin1 −/− mice at postnatal (P) day P10–P13. These neurons presented similar resting membrane potential (V_{rest}) and input resistance (R_{in}) values (data not shown), thus indicating that Pin1 does not affect the passive membrane properties of principal cells. Spontaneous $GABA_A$-mediated inhibitory post-synaptic currents (sIPSCs) were then recorded from both genotypes in the presence of 6,7-dinitroquinoxaline-2,3-dione (DNQX; 20 μM) to block AMPA-mediated excitatory post-synaptic currents (sEPSCs). As shown in Fig. 6a, recordings from Pin1 −/− mice exhibited sIPSCs of higher amplitude values compared with control littermates (106 ± 12 pA versus 62 ± 8 pA; $P < 0.05$), in the absence of any significant change in frequency (4.2 ± 0.5 Hz versus 3.6 ± 0.6 Hz; $P > 0.05$; Fig. 6b). The amplitude distribution histogram of sIPSCs recorded in Pin1 −/− unveiled a clear peak at ∼200 pA (Fig. 6c). The observed effects were selective for sIPSCs since no significant differences in amplitude (22 ± 2 pAin Pin1 −/− mice and 27 ± 4 pA in Pin1 +/+; $n = 6$ for both genotypes; $P > 0.05$) or frequency (1.7 ± 0.3 Hz in Pin1 −/− mice and 1.3 ± 0.4 Hz in Pin1 +/+ mice; $P > 0.05$) of sEPSCs (recorded in the presence of picrotoxin, PTX, 100 μM) were detected between the two genotypes (Supplementary Fig. 2a,b).

Spontaneous inhibitory events from hippocampal neurons in culture overexpressing the NL2HA-S714A mutation exhibited, compared with NL2HA-transfected cells, a significant increase in amplitude (but not frequency), which in part mimicked the phenotype observe in Pin1 −/− mice, suggesting that the interaction of Pin1 with NL2 is critical for this effect (Fig. 7a). As shown in the cumulative amplitude plot (Fig. 7b), the curve obtained from NL2HA-S714A transfected cells was shifted to the right as compared with cells expressing NL2HA ($P < 0.05$).

The selective increase in amplitude of sIPSCs detected in Pin1 −/− mice suggest a post-synaptic site of action. This may involve an increase in the number of active $GABA_A$Rs or changes in single-receptor channel conductance. To distinguish between these two possibilities, peak-scaled non-stationary fluctuations analysis of sIPSCs was performed only on stable recordings with no time-dependent changes in either peak amplitude, 10–90% rise time and decay time (Fig. 8a) (electrotonic filtering was excluded on the basis of no correlation between 10–90% rise time and decay time[30]). Plotting the mean current amplitude versus variance and fitting individual points with the parabolic equation (equation (2) in the methods; Fig. 8b), allowed estimating single-channel conductance and the number of channels open at the peak of spontaneous IPSCs. The single-channel conductance was calculated according to equation (3), assuming a reversal potential for chloride equal to 0. Interestingly, while the values of single-channel conductance were similar in both genotypes (Fig. 8c), the average number of active channels open at the peak of sIPSCs (Np) was significantly increased in Pin1 −/− mice compared with controls (53 ± 11 versus 26 ± 5; $P = 0.03$; Fig. 8c).

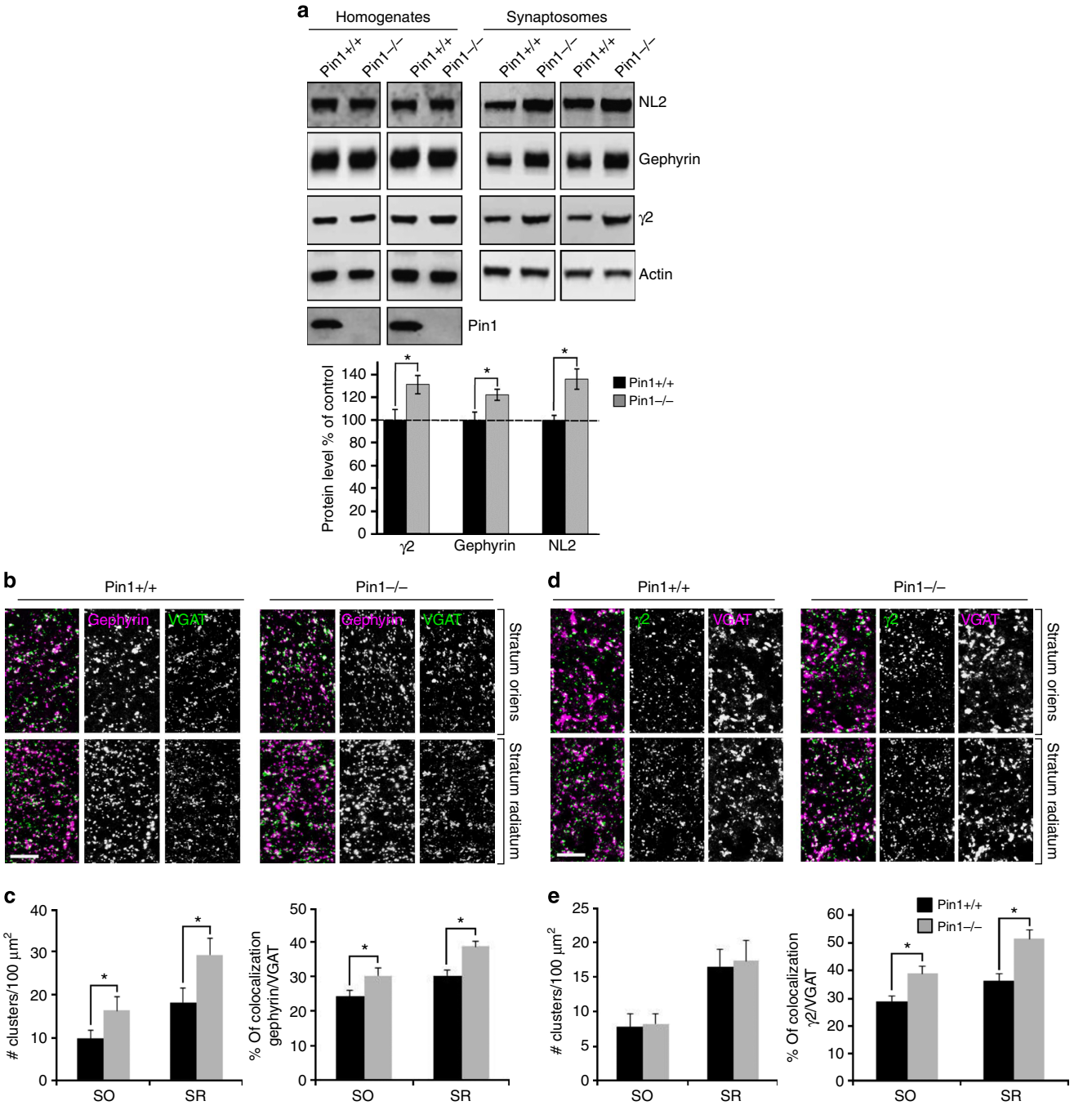

Figure 5 | Synaptic enrichment of $GABA_A$Rs is achieved in Pin1 $-/-$. (**a**) Representative immunoblots of NL2, gephyrin and γ2 subunit of $GABA_A$ receptor extracted from the hippocampus of Pin1 $+/+$ and Pin1 $-/-$ mice (littermates) in two different sets of experiments. Total proteins from the homogenates and synaptosome suspension fractions were analysed by western blotting. Below: quantification of the indicated antigens extracted from hippocampal tissues of Pin1 $+/+$ and Pin1 $-/-$ mice. All markers analysed are enriched at inhibitory synapses. Western blot to actin was done as loading control. Pin1 immunoblot indicates hyppocampus from Pin1 $+/+$ and Pin1 $-/-$ ($n=6$ littermate pairs, mean values ± s.d, $^*P<0.05$, Student's *t*-test) Full images of western blots are in Supplementary Fig. 5. (**b**) Representative confocal micrographs of frontal brain sections showing segments of the SR and SO of the CA1 region of the hippocampus from adult Pin1 $+/+$ and Pin1 $-/-$ mice immunolabeled for gephyrin (magenta) and VGAT (green). Scale bar, 5 µm. (**c**) Quantification of gephyrin punctum density (normalized to 100 μm^2) and their percentage of colocalization with the presynaptic marker VGAT in both mouse genotypes. (**d**) Confocal micrographs as in **a** immunolabeled for $GABA_A$ receptor γ2 subunit (green) and VGAT (magenta). (**e**) Quantification of γ2 subunit punctum and their percentage of colocalization with VGAT in both mouse genotypes. The number of gephyrin, γ2, gephyrin and VGAT puncta was assessed in at least eight sections for each genotypes (Pin1 $+/+$ and Pin1 $-/-$), by taking at least four images of SR and SO of the CA1 region of each hippocampus in each set of experiments ($n=3$). Mean values ± s.d., $^*P<0.05$, Student's *t*-test. Scale bar, 5 µm.

To further evaluate the possibility that higher amplitude inhibitory events recorded in Pin1 $-/-$ mice may originate from $GABA_A$Rs containing different subunits, we measured in both genotypes the decay time constants of small and large amplitude events. Spontaneous IPSCs were plotted against their decay half-widths and arbitrarily divided in two main classes whose

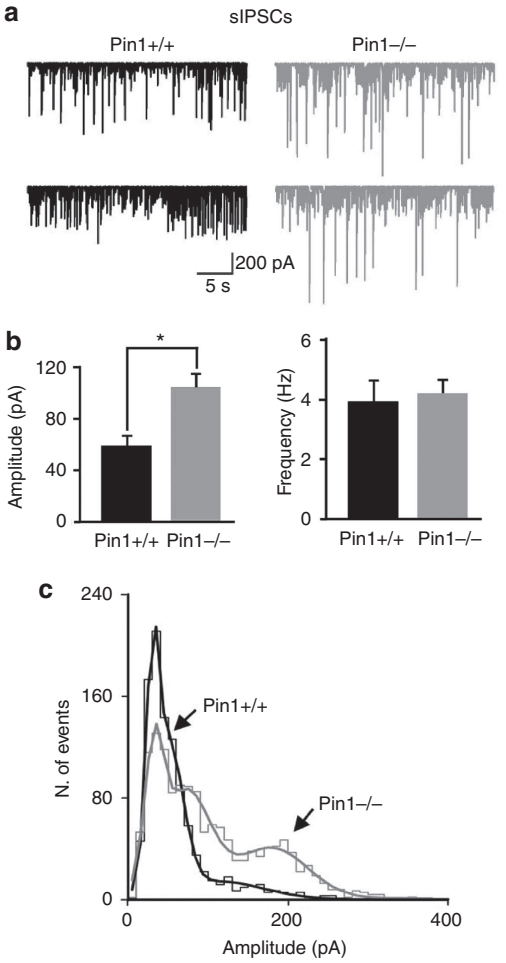

Figure 6 | Pin1 affects the amplitude but not the frequency of sIPSCs. (**a**) Representative traces of sIPSCs recorded from CA1 principal cells at P11 in hippocampal slices from Pin1+/+ (black) and Pin1−/− mice (grey). Note higher amplitude events in Pin1−/− mice. (**b**) Each column represents the mean frequency and amplitude values of sIPSCs recorded from Pin1+/+ (black, $n=9$) and Pin−/− mice (grey, $n=8$). *$P<0.05$, Student's t-test). (**c**) Amplitude distribution histograms of sIPSCs recorded in Pin1+/+ (1,030 events; black) and in Pin1−/− mice (1,412 events; grey). Note the appearance of a clear peak at ~200 pA in Pin1−/− mice.

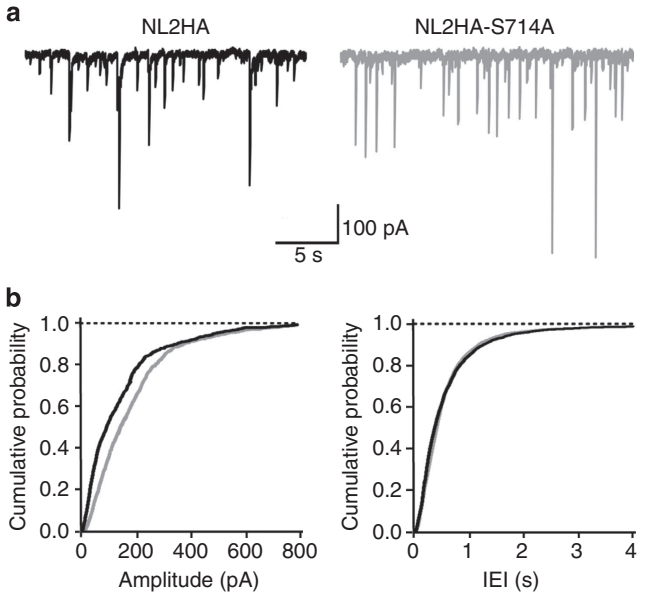

Figure 7 | Changes in amplitude of sIPSCs involve the interaction of Pin1 with NL2. (**a**) Samples traces of sIPSCs recorded from hippocampal neurons in culture expressing either the NL2HA or the NL2HA-S714A mutation. (**b**) Amplitude and inter-event interval (IEI) plots of sIPSCs recorded in cells transfected either with the NL2HA (black; $n=7$) or the NL2HA-S714A point mutant (grey; $n=12$). $P<0.05$; Kolmogorov–Smirnov test. Note the shift to the right of the cumulative amplitude distribution curve obtained from cells transfected with the mutant as compared to controls.

amplitude was <or>150 pA (Fig. 9a, in green and blue, respectively). Notably, larger amplitude events (>150 pA) prevailed in Pin1−/− mice. No differences in decay of sIPSCs <or>150 pA were observed between Pin1+/+ and Pin1−/− mice, thus excluding the involvement of multiple receptor subtypes with different kinetics (the 90–10% decay (τ) of sIPSCs <150 pA was 9±1 ms in Pin−/− mice and 11±2 ms in Pin1+/+; $P>0.05$; τ of sIPSCs >150 pA was 11±2 ms in Pin−/− mice and 10±2 ms in Pin1+/+; $P>0.05$. The 90–10% decay time ($\tau_{90-10\%}$) of all sIPSCs was 11±2 ms and 10±2 ms in Pin1+/+ and Pin1−/− mice, respectively; Fig. 9b,c, P>0.05). These data altogether suggest that the observed increase in amplitude of sIPSCs in Pin1−/− mice is exclusively due a genuine increase in number of $GABA_A$Rs composed of the same subunits.

GABA release and tonic inhibition are unaltered in Pin1−/−. In a previous study, we demonstrated that the functional knockdown of NL2 was accompanied by a reduction in the probability of GABA release[31], thus underlying the role of NLs as retrograde regulators of presynaptic function. Therefore, we evaluated here whether Pin1-dependent modulation of NL2–gephyrin interaction could also affect GABA release from presynaptic nerve terminals. To this end, we used 1,2,5,6-tetrahydropyridin-4-yl methylphosphinic acid (TPMPA), a low affinity competitive $GABA_A$R antagonist[32]. This approach allowed to compare differences in presynaptic GABA transients between Pin1+/+ and Pin1−/− mice. Similar reduction of sIPSCs amplitude in both genotypes (51±6% versus 54±8%, $P>0.05$, Supplementary Fig. 3a,b) was detected on bath application of TPMPA (200 µM), thus excluding a transsynaptic action of Pin1 on GABA release.

Part of GABA released during synaptic activity may escape the cleft and invade the extracellular space to activate extrasynaptic high affinity $GABA_A$Rs. This feature generates a persistent $GABA_A$-mediated conductance[33] that is involved in a number of physiological processes[34]. To determine whether Pin1 signalling affects extrasynaptic $GABA_A$Rs, we analysed the tonic $GABA_A$-mediated conductance in both Pin1+/+ and Pin1−/− mice. The tonic conductance was assessed by the shift of the holding current induced by application of the $GABA_A$R channel blocker PTX (100 µM) (Supplementary Fig. 4a). This drug caused a similar shift in holding current in Pin1−/− and Pin1+/+ mice (Supplementary Fig. 4b,c), indicating that extrasynaptic $GABA_A$ receptors are not influenced by Pin1-mediated signalling.

Discussion

The present study shows that NL2 is a newly identified substrate of proline-directed phosphorylation. This post-translational modification, acting on its unique Pin1 consensus motif localized within the CD (S714-P), modulates the amount of NL2–gephyrin

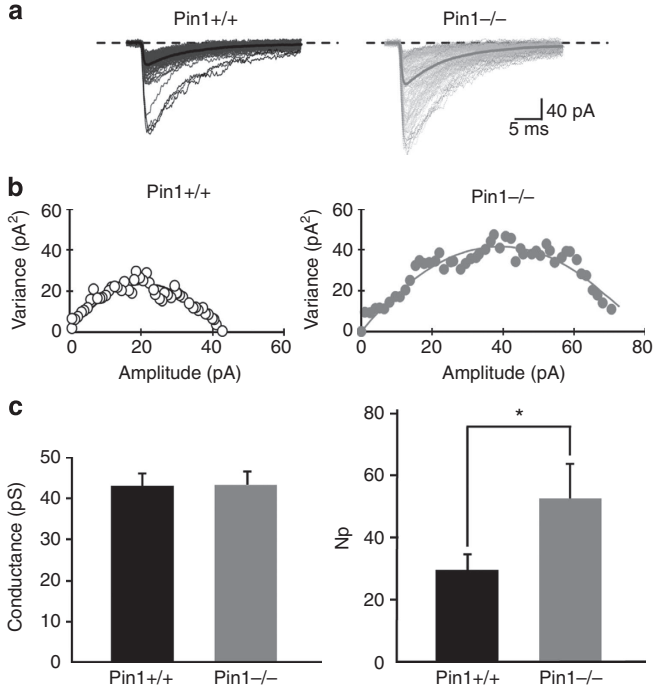

Figure 8 | Pin1 controls the number of active receptor channels at GABAergic synapses. (**a**) Individual sIPSCs from Pin1+/+ (black) and Pin1−/− mice (grey) are shown with the average currents (thick lines). (**b**) Current/variance relationships for sIPSCs shown in **a** (**c**) Summary plots of weighted mean channel conductance (43 ± 3 pS and 43 ± 3 pS, $P = 0.9$, Student's *t*-test) and number of $GABA_A$ receptor channels (Np) in wt (black; $n = 8$) and in Pin1−/− mice (gray; $n = 5$). *$P = 0.03$, Student's *t*-test.

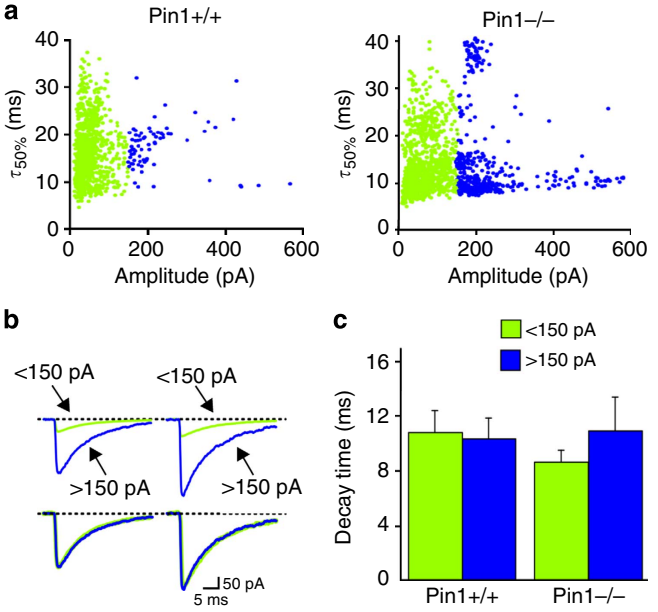

Figure 9 | Pin1 does not affect the decay kinetics of spontaneous IPSCs. (**a**) The peak amplitude of individual sIPSCs <150 pA (green) and >150 pA (blue) is plotted against their decay half-widths (τ_{50}%) in Pin1+/+ and in Pin1−/− mice. (**b**) In the upper part, average traces of spontaneous IPSCs shown in **a**. In the lower part, average traces are normalized and superimposed. (**c**) Each column represents the mean 90–10% decay time constant of spontaneous IPSCs in Pin1+/+ and Pin1−/− mice, <150 pA (green), $n = 8$ and 7, respectively and >150 pA (blue), $n = 6$ and 7, respectively. For all comparisons, $P > 0.05$, Student's *t*-test.

complexes at synaptic sites. This modulation impacts on GABAergic transmission, by selectively affecting the total number of synaptic $GABA_A$Rs. On the basis of these findings, post-phosphorylation prolyl-isomerization can play a crucial role in remodelling the GABAergic PSD to sustain plasticity processes.

Protein phosphorylation on serine and threonine residues preceding a proline, the so-called proline-directed phosphorylation, has emerged as a mechanism regulating signalling events through conformational changes that are catalysed by the phospho-dependent recruitment of the peptidyl-prolyl isomerase Pin1. While the different roles of Pin1 in dividing cells have long been established and characterized[19], its function in post-mitotic neurons in general and at synapses in particular is still poorly understood. In a previous study, we identified gephyrin, the main scaffolding protein of inhibitory PSD, as a new target of post-phosphorylation prolyl-isomerization[22].

Here, by inspecting the protein sequence of NL CDs, we identified S/T-P motifs that may provide Pin1 binding sites if phosphorylated *in vivo*. In particular, NL2 presents a unique Pin1 consensus site in its cytoplasmic region, S714-P, which is located 15 amino acids apart from the transmembrane domain. Even though this proximity to the plasma membrane raises doubts about its accessibility by a proline-directed kinase, several lines of evidence suggest that endogenous NL2 can undergo proline-directed phosphorylation. First, this isoform was recognized by the MPM2 antibody on NL2 immunoprecipitation from mouse brain homogenates. Second, MPM2-mediated NL2 immunoprecipitation was still maintained on removal of the NL2–gephyrin-binding domain, excluding the possibility of an indirect recognition mediated by endogenous gephyrin. Third, such detection was completely lost on NL2HA-S714A mutagenesis. This phosphorylation event is then able to directly recruit the effector molecule of the signalling cascade Pin1, as shown by co-immunoprecipitation experiments with endogenous neuronal proteins. Also in this case, Pin1 binding to NL2 was still maintained on the removal of the GBD, while it was completely abolished by mutating S714 to alanine, thus suggesting that the prolyl isomerase can be directly recruited by the unique NL2 Pin1 consensus motif in a phosphorylation-dependent manner. These results altogether indicate that NL2 represents a newly identified substrate for proline-directed signalling cascade *in vivo*.

Our biochemical data demonstrate that NL2–gephyrin interaction is negatively regulated by proline-directed phosphorylation. Co-immunoprecipitation experiments on recombinantly expressed gephyrin-FLAG and NL2HA unveiled an enhanced complex formation on pharmacological inhibition of Pin1 catalytic activity. Similarly, endogenous NL2/gephyrin complexes pulled down from whole brain or hippocampal tissues of Pin1−/− animals were significantly augmented as compared with the corresponding WT tissues. These biochemical findings were also validated by immunocytochemistry performed on cultured hippocampal neurons, where we could detect a high number of clusters co-labelled for NL2 and gephyrin as well as their increased apposition to presynaptic GABAergic inputs in the absence of Pin1 expression. Interestingly, the NL2 point mutant unable to undergo prolyl-isomerization was capable to recruit gephyrin even more efficiently as compared with the WT form, whereas gephyrin mutagenesis at two putative Pin1 consensus motifs, S270A and S319A, located within, or close to, the minimal NL2 binding domain, was completely ineffective. The fact that this post-translational modification seems to control the strength of NL2 association with gephyrin by acting mainly on NL2, and not *vice versa*, further reinforces the emerging idea

that cell adhesion molecules are key determinant in regulating synapse function. In a recent study by Giannone *et al.*[18], it has been demonstrated that the level of NL1 phosphorylation at a specific tyrosine residue located within the GBD dictates the strength of NL1/gephyrin interaction. In other words, NL1, the isoform enriched at excitatory synapses and therefore mostly associated with PSD95, can potentially recruit gephyrin as well as NL2, but its phosphorylation, promoted by neurexin–adhesion signalling, precludes such interaction while favouring PSD95 binding. Our experimental data indicate that proline-directed phosphorylation is acting similarly to tyrosine phosphorylation signalling. Since NL2 S714 is not positioned within the GBD, but is located just 50 amino acid upstream, it is reasonable to believe that Pin1-driven conformational changes, by affecting the overall folding of the CD, will induce gephyrin release (Fig. 10a). Alternatively, these conformational changes may promote NL2 tyrosine phosphorylation, an event shown to impede NLs/gephyrin interaction[18] (Fig. 10b). Interestingly, tyrosine to alanine mutagenesis on NL2 was shown to completely abolish recombinant gephyrin recruitment by the mutant protein or to strongly reduce its interaction with endogenous gephyrin[6]. Whether NL2 phosphorylation occurs at tyrosine 770 and whether this event is able to hamper gephyrin binding is still unknown.

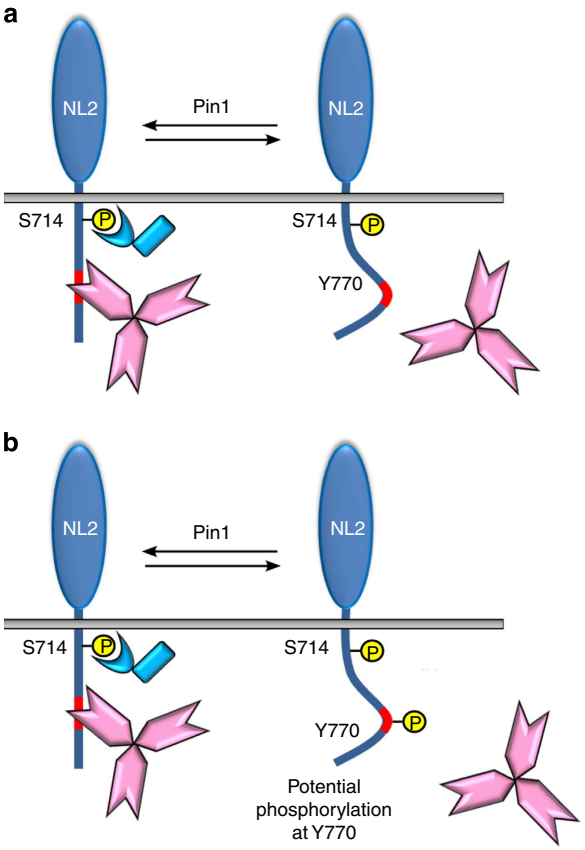

Figure 10 | Model of the putative cross-talk between proline-directed phosphorylation and tyrosine phosphorylation. Phosphorylation of NL2 CD at S714 by a proline-directed kinase allows the recruitment of the proly isomerase Pin1. Pin1-driven conformational changes, by altering the folding of the NL2 CD, may represent the main cause responsible for gephyrin detachment (**a**). Alternatively, Pin1-mediated structural rearrangement may render the conserved tyrosine residue of the GBD (Y770) susceptible to phosphorylation, an event shown to prevent NL1/gephyrin interaction (**b**).

The other partner of the complex is represented by gephyrin, a recognized target of Pin1 (ref. 22). Gephyrin contains 10 consensus motifs mostly concentrated in its C-domain, and all of them found to be phosphorylated *in vivo*[35,36]. This region of the protein is positioned between the amino-terminal G- and carboxyl-terminal E-domains, which are directly involved in gephyrin multimerization. Conformational changes induced by phosphorylation, possibly followed by prolyl-isomerization, are expected to alter the conformation of the gephyrin C-domain and in turn, regulate specific functional properties of gephyrin, in particular its binding to interacting proteins, including possibly NL2. However, the complexity of the system under investigation makes it very difficult to determine whether and how a specific phosphorylation event can contribute, directly or indirectly, to enhance gephyrin association to NL2. Nevertheless, it should be emphasized that gephyrin is robustly phosphorylated at several residues *in vivo*, thus suggesting that a specific pattern of phosphorylation, rather than a single post-translational modification, is functionally determinant. In contrast, NL2 possesses a unique target for prolyl-isomerization suggesting that it could represent the master switch of the signalling cascade.

Our electrophysiological experiments clearly demonstrate that deletion of Pin1 specifically affects GABAergic transmission, causing a dramatic increase in amplitude, but not in frequency, of sIPSCs due to an increase in the number of $GABA_A$Rs at post-synaptic sites. Notably, such enhancement was detected on neuronal overexpression of the NL2 mutant unable to undergo prolyl-isomerization, suggesting a functional link between the signalling cascade strengthening NL2/gephyrin interaction and the increased synaptic recruitment of $GABA_A$Rs. There is a large body of evidence underlying the key role played by NL2 in promoting clustering and/or stabilization of $GABA_A$Rs at post-synaptic sites. By employing a heterologous expression system, it was shown that $GABA_A$Rs are able to co-aggregate with NL2 and only the presence of this isoform can induce strong GABAergic presynaptic differentiation from co-cultured neurons and promote the establishment of fully functional hemi-synapses[37]. In NL2-deficient mice, the number of functional $GABA_A$Rs detected in the retina was shown to be drastically reduced[38]. Furthermore, targeting of $GABA_A$Rs and gephyrin scaffold appeared severely compromised in the pyramidal cell layer of the CA1 region of the hippocampus, a morphological phenotype accompanied by a strong deficit in synaptic inhibition[6].

The increased recruitment of synaptic $GABA_A$ receptors in Pin1 −/− mice may simply depend on the enhanced gephyrin targeting at synaptic sites. More scaffold deposition should offer a high number of binding sites available for the transient immobilization of $GABA_A$Rs at inhibitory synapses. In addition, or alternatively, we cannot exclude the possibility that the extracellular domain of NL2 could also participate in $GABA_A$Rs receptor recruitment. The unique S714-P consensus motif, located very close to the NL2 transmembrane domain, could influence the folding of the extracellular domain of NL2, rendering it incapable to interact in *cis* with $GABA_A$R subunits. This type of mechanism has been shown to operate at excitatory synapses, where the abundance of NMDARs is controlled by the interaction occurring between the GluN1 subunit with NL1-specific sequences located in its extracellular domain[39].

In conclusion, our findings unveil the existence of a new signalling pathway operating at GABAergic synapses to alter the efficacy of GABAergic transmission by modulating NL2/gephyrin interaction. Although a comprehensive understanding of the molecular mechanisms underlying the action of Pin1 on NL2/gephyrin interaction is still lacking, we believe that our study further emphasizes the key role played by NL2 in organizing and stabilizing GABAergic synapses.

Methods

Plasmid constructs. The expression construct for HA-tagged human NL2 in pNice was kindly provided by P. Scheiffele (Biozentrum, Basel). The amino acid sequence ranging from residues 768 to 782 was removed to generate the NL2HA lacking the gephyrin binding domain (pNice-NL2HA-ΔGBD). S714A mutation was also introduced into pNice-NL2HA-ΔGBD to remove the unique Pin1 consensus site (pNice-NL2HA-ΔGBDS714A). All PCR-based mutagenesis were fully sequenced to exclude the possibility of second site mutations. pcDNA3-FLAG-Pin1 WT and pcDNA3-gephyrin-FLAG have been previously described[22]. EGFP-tagged gephyrin point mutants (S270A and S319A), the WT and the truncated version ranging from amino acid 326 to 736 and 310 to 736, were PCR cloned into the *Xho*I/*Hin*dIII sites of pEFP-C1 (Clontech, Mountain View, CA). EGFP-tagged gephyrin GC (1–310) was kindly provided by G. Schwarz (University of Cologne, Germany)[40].

Cell cultures and transfections. HEK-293-T cells were cultured at 37 °C under a 5% CO2 atmosphere in Dulbecco's modified Eagle's medium supplemented with 10% fetal bovine serum. They were transiently transfected with various plasmid constructs using Lipofectamine 2000 (Invitrogen) according to the manufacturer's protocol. Cells were collected 24–48 h after transfection.

Primary hippocampal neurons from P0 Pin1 +/+ and Pin1 −/− littermates and rat hippocampal neurons were prepared as previously described[41]. Being Pin1 −/− mice infertile, Pin1 +/+ and Pin1 −/− littermates for neuronal cultures were routinely obtained by mating heterozygous mice[42]. Each hippocampus derived from single newborn littermate was processed and plated separately and identified by tail genotyping. Neurons were Lipofectamine transfected after 8 DIV with 1 μg of EGFP-gephyrinWT or EGFP-gephyrinS270A and processed for immunofluorescence 2–3 days later. For electrophysiological recordings, neurons were co-transfected with 1 μg NL2HA/NL2HA-S714A and 500 ng of green fluorescent protein (GFP) to visualize transfected cells.

PiB treatments. To inhibit Pin1 catalytic activity, the chemical inhibitor PiB (diethyl-1,3,6,8-tetrahydro-1,3,6,8-tetraoxobenzol-phenanthroline-2,7-diacetate) was added to the culture medium for 24 h at a concentration of 2.5 μm. PiB was purchased from Calbiochem and resuspended in DMSO.

Immunoprecipitation and chemical cross-linking. Immunoprecipitation for MPM2 experiments was performed using a lysis buffer containing 50 mM Tris–HCl, pH 7.5, 1% Nonidet P-40, 0.5% Triton X-100, 150 mM NaCl, 1 mM Na_3VO_4, 50 mM NaF and protease inhibitor mixture (Sigma). For NL2HA and gephyrin co-immunoprecipitation, HEK293 cells overexpressing NL2HA and gephyrin-FLAG were treated 48 h after transfection with 2.5 mM PiB or mock treated with DMSO as negative controls. Cells were lysed in 50 mM Tris-HCl, pH 7.5, 100 mM NaCl, 0.1% Tween 20, 10% glycerol, 10 mM EDTA, 2 mM $MgCl_2$ and protease inhibitor mixture and immunoprecipitated by either the anti-FLAG antibody or anti-HA agarose (Pierce).

Co-immunoprecipitation of native gephyrin–NL2 complexes from p15 Pin1 +/+ and Pin1 −/− mouse brains or hippocampal tissues was performed using a chemical cross-linking approach on postnuclear homogenates as previously described[6]. Primary antibodies were revealed by HRP-conjugated secondary antibodies (Sigma) followed by ECL (Amersham Biosciences).

Biotinylation assay and analysis on synaptosomes. To examine changes in NL2 transported at the plasma membrane, we performed biotinylation assays on hippocampal neuronal cultures derived from Pin1 +/+ and Pin1 −/− mice. Neuronal cells were incubated with 0.5 mg ml^{-1} EZ-Link Sulfo-NHS-LC-Biotin (Pierce) in PBS at 4 °C for 30 min. To quench the reaction, cells were washed three times with cold PBS containing 0.1 M Tris-HCl pH 7.4. Cells were then lysed in lysis buffer containing protease inhibitor cocktail followed by centrifugation at 1,000*g* for 5 min. The collected lysate were incubated with streptavidin cross-linked to agarose beads (Pierce) for 2 h at 4 °C. The beads were then washed twice with lysis buffer, and eluted with SDS loading buffer. The amount of membrane protein loaded in each experiments was normalized to the amount of the glycophosphatidylinositol-anchored protein Flotilin1, whose expression levels are identical in both mouse genotypes.

PSD enriched extracts were prepared by using the Syn-PER Synaptic Protein Extraction Reagent (ThermoScientific) following the manufacturer's instructions. Briefly, a pool of four hippocampi derived from the same genotypes were homogenized in the Extraction reagents (10 ml of reagent per g of tissue), centrifuged at 1,200*g* for 10 min. The pellet was discarded while the supernatant (homogenate) was additionally centrifuged at 15,000*g* for 20 min. The cytosolic fraction was discarded and the pellet containing the synaptosomes was resuspended in 400–500 μl of reagent and analysed by western blot analysis. The protein concentration of each sample was determined using the Pierce BCA Protein Assay to allow an equal loading of total protein.

Western blot analysis. Western blot image acquisition was performed using the ECL detection kit and the Alliance 4.7 software (UVITECH, Cambridge). Quantifications were performed using the UVIband imager software (Amersham). The relative amount (Input, 1/20 of the total lysate) of the different antigens considered in this study and the immunoprecipitated fractions were determined by densitometry on the acquired images. The amount of immunoprecipitated and coimmunoprecipitated proteins are first normalized to their corresponding inputs and then the coimmunoprecipated value is additionally normalized on the immunoprecipitated antigen. Full images of western blots are in Supplementary Fig. 5.

Antibodies. The following antibodies were used in immunohistochemistry and immunocitochemistry: anti-gephyrin Mab7a (Synaptic System Cat. No 147021), anti-VGAT rabbit or guinea pig (1:1,000, Synaptic System Cat. No 131004), anti-NL2 rabbit affinity purified (1:500, Synaptic system Cat, No 129203), guinea pig anti-$GABA_A$ γ2 subunit (1:2,000 (ref. 43)), biotinylated anti-guinea pig (1:200, Vector Laboratories, Cat No BA-7000). The following primary antibodies were used in immunoprecipitation and western blot analysis: mouse monoclonal anti-FLAG M2 (Sigma Cat No F1804), mouse monoclonal anti-gephyrin 3B11 (Synaptic System Cat No 147111) and rabbit polyclonal anti-NL2 (Synaptic Systems Cat. No 129202), pS/pT-P (MPM2, Upstate Biotechnology Cat No 05-368), high affinity rat monoclonal anti-HA 3F10 (Roche), anti-GFP rabbit monoclonal (Life Technology, Cat No G10362). Validation of antibodies used in these assays can be found on the respective manufacturers' websites.

Immunohistochemistry and immunocytochemistry. Eight-week-old Pin1 +/+ and Pin1 −/− littermates (for each genotype, $n=3$) were anaesthetized and perfused transcardially with 0.1 M phosphate buffer, pH 7.4 (PB). Brains were quickly removed from the skull and frozen with isopentane cooled to −40 °C with liquid nitrogen. Ten to 12-μm thick cryostat sections were collected on Superfrost glass slides and further processed for immunostaining for combined detection of VGAT and GABAA γ2 or VGAT and gephyrin. Briefly, cryostat sections were fixed by immersion in 2% paraformaldehyde, and mildly treated with pepsin as antigen-retrieval procedure, and then incubated for 48 h with different combination of primary antibodies. Secondary antibody staining was performed for 1 h at room temperature using anti-isotypic fluorophore-conjugated antibodies Alexa-488 and Alexa-594 at dilutions of 1:1,000 (Molecular Probes).

Hippocampal neurons grown on glass coverslips were fixed with 4% paraformaldehyde and 4% sucrose in PBS. Unspecific binding was blocked by incubation with 10% normal goat serum in PBS. Primary and secondary antibodies were diluted in 5% normal goat serum/PBS. Secondary antibodies included anti-isotypic fluorophore conjugated antibodies Alexa-488, Alexa-594 and streptavidin-Alexa 405 at dilutions of 1:1,000 (Molecular Probes).

Confocal microscopy and image analysis. Fluorescence images were acquired on a TCS-SP confocal laser scanning microscope (Leica, Bensheim, Germany) with a ×40 1.4 NA or ×63 1.4 NA oil immersion objectives, additionally magnified fivefold with the pinhole set at 1 Airy unit. All the parameters used in confocal microscopy were consistent in each experiment, including the laser excitation power, detector and off-set gains and the pinhole diameter. Stacks of z-sections (12–13 optical sections) with an interval of 0.3 μm were sequentially scanned three times for each emission line to improve the signal/noise ratio. The number of gephyrin, γ2 subunit and VGAT puncta was assessed in at least eight sections for each genotypes (Pin1 +/+ and Pin1 −/−), by taking at least four images of strata radiatum and oriens of the CA1 region of each hippocampus in each set of experiments ($n=3$). In the pyramidal cell layer, the high density and elongated shape of VGAT positive terminals precluded the determination of their numbers and their colocalization with the other two antigens investigated.

For immunocitochemistry samples, at least 10 cells from at least three independent batches per condition were used for analysis. Images were acquired as a *z*-stack (six to seven optical sections, 0.25 μm step size). In each image, at least five dendritic segments were outlined and saved as regions of interest.

Quantification of immunofluorescence data was performed using the Volocity3D Image Analysis Software (PerkinElmer, London, UK). Gephyrin, NL2, $GABA_AR$ γ2 and VGAT clusters were determined after thresholding of images. Thresholds were determined using the 'voxel spy' facility of the software and chosen such that all recognizable punctuate structures were included into the analysis (minimal area, 0.1 μm^2); colocalization was evaluated based on the determination of thresholded Pearson's correlation coefficient (PCC > 0,5) for each gephyrin and γ2 cluster previously identified and quantified[44]. NL2 colocalization with gephyrin puncta was also quantified utilizing the software function 'intersect object' that measures size, volume and intensity values of intersecting objects identified by separate protocols in each channel. To determine the degree of apposition of NL2/gephyrin colabeled clusters with the presynaptic marker VGAT, we superimposed the mask of all identified overlapping puncta onto the third channel and count them manually.

Hippocampal slice preparation and drug treatment. All experiments were performed in accordance with the European Community Council Directive of November 24, 1986 (86/609EEC) and were approved by the local authority veterinary service and by SISSA ethical committee. All efforts were made to

minimize animal suffering and to reduce the number of animal used. Transverse hippocampal slices (300 μm thick) were obtained from postnatal (P) day P10–P13 mice (male and female) using a standard protocol[45]. Briefly, after being anaesthetized with CO_2, animals were decapitated. The brain was quickly removed from the skull and placed in ice-cold artificial cerebrospinal fluid containing (in mM): 130 NaCl, 25 glucose, 3.5 KCl, 1.2 NaH_2PO_4, 25 $NaHCO_3$, 2 $CaCl_2$ and 1.3 $MgCl_2$, saturated with 95% O_2 and 5% CO_2 (pH 7.3–7.4). Transverse hippocampal slices (300 μm thick) were cut with a vibratome and stored at room temperature (22–24 °C) in a holding bath containing the same solution as above. After incubation for at least 45 min, an individual slice was transferred to a submerged recording chamber and continuously superfused at 33–34 °C with oxygenated artificial cerebrospinal fluid at a rate of 3–4 ml min^{-1}.

The following drugs were used: DNQX, PTX and bicuculline, purchased from Ascent Scientific; TPMPA purchased from Tocris Bioscence. DNQX and PTX were dissolved in DMSO. The final concentration of DMSO in the bathing solution was 0.1%. At this concentration, DMSO alone did not modify the membrane potential, input resistance or the firing properties of CA1 pyramidal neurons. Drugs were applied in the bath by gravity via a three-way tap system by changing the superfusion solution to one differing only in its content of drug(s). The ratio of flow rate to bath volume ensured a complete exchange within 2 min.

Electrophysiological recordings. Whole-cell patch-clamp recordings (in voltage clamp configuration) were performed from CA1 pyramidal cells, visualized with an upright microscope equipped with differential interference contrast optics and infrared video camera, using a patch-clamp amplifier (Axopatch 1D amplifier, Molecular Devices, Sunnyvale, CA, USA). Patched electrodes were pulled from borosilicate glass capillaries (Hingelberg, Malsfeld, Germany). They had a resistance of 4–6 MΩ when filled with the intracellular solution containing (in mM): 125 Cs-methanesulphonate, 10 CsCl, 10 HEPES, 0.3 EGTA, 2 MgATP, 0.3 NaGTP (pH adjusted to ~7.3 with CsOH; the osmolarity was adjusted to 290 mOsmol). The stability of the patch was checked by repetitively monitoring the input and series resistance during the experiment. Cells exhibiting >20% changes in series resistance were excluded from the analysis. The series resistance was <25 MΩ and was not compensated.

Spontaneous GABAergic (sIPSCs) and glutamatergic (sEPSCs) post-synaptic currents were routinely recorded from a holding potential of −60 mV in the presence of DNQX (20 μM) and PTX (10 μM), respectively. While sEPSCs were recorded using patch pipettes filled with the above mentioned solution, sIPSCs were recorded using an intracellular solution containing (in mM): CsCl 137, Hepes 10, BAPTA 11, MgATP 2, $MgCl_2$ 2, $CaCl_2$ 1 and 5 QX-314 (pH adjusted to ~7.3 with CsOH).

sIPSC were also recorded from cultured hippocampal neurons co-transfected with GFP and NL2HA or NL2HA-S714A 24 h after transfection, at a holding potential of −60 mV in presence of DNQX (20 μM) with the same intracellular solution used for the acute slices experiment. The extracellular solution contained (in mM) 137 NaCl, 5 KCl, 2 $CaCl_2$, 1 $MgCl_2$, 20 glucose and 10 HEPES, pH 7.4 (corrected with NaOH).

Data analysis. Data were acquired and digitized with an A/D converter (Digidata 1,200, Molecular Devices) and stored on a computer hard disk. Acquisition and analysis were performed with Clampfit 9 (Molecular Devices).

Data were acquired at 20 kHz, filtered with a cut-off frequency of 2 kHz and stored on computer hard disk to perform off-line analysis. The resting membrane potential was measured immediately after break-in and establishing whole-cell recording. The membrane input resistance (R_{in}) was calculated by measuring the amplitude of voltage responses to steady hyperpolarizing current steps, using the Clampfit 10.0 program (Molecular Devices).

Spontaneous AMPA- and $GABA_A$-mediated post-synaptic currents were analysed using Clampfit 10.0 (Molecular Devices). This programme uses a detection algorithm based on a sliding template. The template did not induce any bias in the sampling of events because it was moved along the data trace by one point at a time and was optimally scaled to fit the data at each position. The detection criterion was calculated from the template-scaling factor and from how closely the scaled template fitted the data.

Spontaneous GABAergic currents were analysed with Mini Analysis program (version 6.0.1, Synaptosoft, Leonia, NJ) for their decay time constants. Only events with no deflections in the rising or decaying phases were included in the analysis. Low amplitude (<5 pA) events as well as events whose amplitude correlated with the rising or decaying time constants were discarded from the analysis because they were thought to be affected by dendritic filtering. The decay time of s IPSCs were fitted with a single exponential function as:

$$I(t) = Aexp(-t/\tau) \quad (1)$$

where $I(t)$ is the current as a function of time, A is the amplitude at time 0, τ is the time constant.

The Mini Analysis programme was used to perform peak-scaled non-stationary noise analysis according to Traynelis and co-workers[46]. Individual, not correlated, events were aligned to the point of steepest rise time. The peak of the mean current response waveform was scaled to the response value at the corresponding point in time of each individual event before subtraction to generate the difference waveforms. The ensemble mean post-synaptic current was binned into 50 bins of equal amplitude to assign similar weights to all phases of ensemble mean waveform. Variance was plotted against amplitude and individual points were fitted with the equation:

$$\sigma^2(I) = iI - I^2/N + \sigma_b^2 \quad (2)$$

where i is the unitary single-channel current, I is the mean current, N is the number of channels open at the current peak and σ_b^2 is the variance of the background noise. The single-channel chord conductance (γ) was calculated as:

$$\gamma = i/(E_m - E_{rev}) \quad (3)$$

from the holding potential (E_m) of −60 mV, assuming a reversal potential (E_{rev}) of 0 mV.

Amplitude distribution of sIPSCs amplitude was obtained fitting data with the following Gaussian function:

$$n(I) = \sum_{i=1}^{n} (a_i/\sqrt{2\pi\sigma^2})\ exp(-(I_i - I_{\sigma i})^2/2\,\sigma_i^2) \quad (4)$$

where I_σ is the mean current, a_i is the area and σ is the variance.

The amplitude of the tonic current was estimated by the outward shift of the baseline current after the application of the $GABA_A$ receptor channel blocker PTX (100 μM). Only current recordings that exhibited a stable baseline were included in the analysis. Baseline currents were estimated by plotting four to five 0.5 s periods in all point histograms. These were fitted with a Gaussian function. The peak of the fitted Gaussian was considered as the mean holding current[47].

Statistics. Statistical analyses for Co-IP, PSD enriched extracts fractions analyses were performed by using Microsoft Excel. Comparisons were performed by Student's t-test two-tailed distribution unequal variance. Deviation and error bars were calculated using the same software. Statistical significance was defined as $P<0.05$.

Statistical analyses of morphological data (NL2 and gephyrin cluster size and density) were performed pair-wise (Pin1 −/− versus Pin1 +/+) using unpaired, two-tailed Student's t-test. Bars indicate (s.d.)

Statistical analyses for electrophysiological experiments were performed by using pClamp 10 and Microsoft Excel. Comparison were perfomed by Student's t-test unless otherwise stated. Statistical significance was defined as $P<0.05$.

References

1. Vithlani, M. & Moss, S. J. The role of $GABA_AR$ phosphorylation in the construction of inhibitory synapses and the efficacy of neuronal inhibition. *Biochem. Soc. Trans.* **37,** 1355–1358 (2009).
2. Jacob, T. C., Moss, S. J. & Jurd, R. GABA(A) receptor trafficking and its role in the dynamic modulation of neuronal inhibition. *Nat. Rev. Neurosci.* **9,** 331–343 (2008).
3. Südhof, T. C. Neuroligins and neurexins link synaptic function to cognitive disease. *Nature* **455,** 903–911 (2008).
4. Levinson, J. N. *et al.* Neuroligins mediate excitatory and inhibitory synapse formation: involvement of PSD-95 and neurexin-1beta in neuroligin-induced synaptic specificity. *J. Biol. Chem.* **280,** 17312–17319 (2005).
5. Craig, A. M. & Kang, Y. Neurexin-neuroligin signalling in synapse development. *Curr. Opin. Neurobiol.* **17,** 43–52 (2007).
6. Poulopoulos, A. *et al.* Neuroligin2 drives postsynaptic assembly at perisomatic inhibitory synapses through gephyrin and collybistin. *Neuron* **63,** 628–642 (2009).
7. Varoqueaux, F., Jamain, S. & Brose, N. Neuroligin 2 is exclusively localized to inhibitory synapses. *Eur. J. Cell Biol.* **83,** 449–456 (2004).
8. Pfeiffer, F., Graham, D. & Betz, H. Purification by affinity chromatography of the glycine receptor of rat spinal cord. *J. Biol. Chem.* **257,** 9389–9393 (1982).
9. Prior, P. *et al.* Primary structure and alternative splice variants of gephyrin, a putative glycine receptor-tubulin linker protein. *Neuron* **8,** 1161–1170 (1992).
10. Essrich, C., Lorez, M., Benson, J. A., Fritschy, J. M. & Luscher, B. Postsynaptic clustering of major GABAA receptor subtypes requires the gamma2 subunit and gephyrin. *Nat. Neurosci.* **1,** 563–571 (1998).
11. Kneussel, M. *et al.* Loss of postsynaptic GABA(A) receptor clustering in gephyrin-deficient mice. *J. Neurosci.* **19,** 9289–9297 (1999).
12. Tretter, V. *et al.* Gephyrin, the enigmatic organizer at GABAergic synapses. *Front. Cell. Neurosci.* **6,** 1–16 (2012).
13. Schwarz, G., Schrader, N., Mendel, R. R., Hecht, H. J. & Schindelin, H. Crystal structures of human gephyrin and plant Cnx1 G domains: comparative analysis and functional implications. *J. Mol. Biol.* **312,** 405–418 (2001).
14. Sola, M., Kneussel, M., Heck, I. S., Betz, H. & Weissenhorn, W. X-ray crystal structure of the trimeric N-terminal domain of gephyrin. *J. Biol. Chem.* **276,** 25294–25301 (2001).
15. Sola, M. *et al.* Structural basis of dynamic glycine receptor clustering by gephyrin. *EMBO J.* **23,** 2510–2519 (2004).
16. Maric, H. M., Mukherjee, J., Tretter, V., Moss, S. J. & Schindelin, H. Gephyrin-mediated GABA(A) and glycine receptor clustering relies on a common binding site. *J. Biol. Chem.* **286,** 42105–42114 (2011).

17. Kowalczyk, S. *et al.* Direct binding of GABAA receptor β2 and β3 subunits to gephyrin. *Eur. J. Neurosci.* **37,** 544–554 (2013).
18. Giannone, G. *et al.* Neurexin-1β binding to neuroligin-1 triggers the preferential recruitment of PSD-95 versus gephyrin through tyrosine phosphorylation of neuroligin-1. *Cell Rep.* **3,** 1996–2007 (2013).
19. Lu, K. P. & Zhou, X. Z. The prolyl isomerase PIN1: a pivotal new twist in phosphorylation signaling and disease. *Nat. Rev. Mol. Cell. Biol.* **8,** 904–916 (2007).
20. Ranganathan, R., Lu, K. P., Hunter, T. & Noel, J. P. Structural and functional analysis of the mitotic rotamase Pin1 suggests substrate recognition is phosphorylation dependent. *Cell* **89,** 875–886 (1997).
21. Shen, M., Stukenberg, P. T., Kirschner, M. W. & Lu, K. P. The essential mitotic peptidyl-prolyl isomerase Pin1 binds and regulates mitosis-specific phosphoproteins. *Genes Dev.* **12,** 706–720 (1998).
22. Zita, M. M. *et al.* Post-phosphorylation prolyl isomerisation of gephyrin represents a mechanism to modulate glycine receptors function. *EMBO J.* **26,** 1761–1771 (2007).
23. Davis, F. M., Tsao, T. Y., Fowler, S. K. & Rao, P. N. Monoclonal antibodies to mitotic cells. *Proc. Natl Acad. Sci. USA* **80,** 2926–2930 (1983).
24. Lu, K. P. Pinning down cell signaling, cancer and Alzheimer's disease. *Trends Biochem. Sci.* **29,** 200–209 (2004).
25. Uchida, T. *et al.* Pin1 and Par14 peptidyl prolyl isomerase inhibitors block cell proliferation. *Chem. Biol.* **10,** 15–24 (2003).
26. Zacchi, P., Antonelli, R. & Cherubini, E. Gephyrin phosphorylation in the functional organization and plasticity of GABAergic synapses. *Front. Cell. Neurosci.* **8,** 103 (2014).
27. Tyagarajan, S. K. *et al.* Regulation of GABAergic synapse formation and plasticity by GSK3beta-dependent phosphorylation of gephyrin. *Proc. Natl Acad. Sci. USA* **108,** 379–384 (2011).
28. Levinson, J. N. *et al.* Postsynaptic scaffolding molecules modulate the localization of neuroligins. *Neuroscience* **165,** 782–793 (2010).
29. Dumoulin, A., Lévi, S., Riveau, B., Gasnier, B. & Triller, A. Formation of mixed glycine and GABAergic synapses in cultured spinal cord neurons. *Eur. J. Neurosci.* **12,** 3883–3892 (2000).
30. Momiyama, A. *et al.* The density of AMPA receptors activated by a transmitter quantum at the climbing fibre-Purkinje cell synapse in immature rats. *J. Physiol.* **549,** 75–92 (2003).
31. Varley, Z. K. *et al.* Gephyrin regulates GABAergic and glutamatergic synaptic transmission in hippocampal cell cultures. *J. Biol. Chem.* **286,** 20942–20951 (2011).
32. Barberis, A., Petrini, E. M. & Cherubini, E. Presynaptic source of quantal size variability at GABAergic synapses in rat hippocampal neurons in culture. *Eur. J. Neurosci.* **20,** 1803–1810 (2004).
33. Farrant, M. & Nusser, Z. Variations on an inhibitory theme: phasic and tonic activation of GABA(A) receptors. *Nat. Rev. Neurosci.* **6,** 215–229 (2005).
34. Brickley, S. G. & Mody, I. Extrasynaptic GABA(A) receptors: their function in the CNS and implications for disease. *Neuron* **73,** 23–34 (2012).
35. Herweg, J. & Schwarz, G. Splice-specific glycine receptor binding, folding, and phosphorylation of the scaffolding protein gephyrin. *J Biol Chem.* **287,** 12645–12656 (2012).
36. Tyagarajan, S. K. *et al.* Extracellular signal-regulated kinase and glycogen synthase kinase 3β regulate gephyrin postsynaptic aggregation and GABAergic synaptic function in a calpain-dependent mechanism. *J. Biol. Chem.* **288,** 9634–9647 (2013).
37. Dong, N., Qi, J. & Chen, G. Molecular reconstitution of functional GABAergic synapses with expression of neuroligin-2 and GABAA receptors. *Mol. Cell. Neurosci.* **35,** 14–23 (2007).
38. Hoon, M. *et al.* Neuroligin 2 controls the maturation of GABAergic synapses and information processing in the retina. *J. Neurosci.* **29,** 8039–8050 (2009).
39. Budreck, E. C. *et al.* Neuroligin-1 controls synaptic abundance of NMDA-type glutamate receptors through extracellular coupling. *Proc. Natl Acad. Sci. USA* **110,** 725–730 (2013).
40. Lardi-Studler, B. *et al.* Vertebrate-specific sequences in the gephyrin E-domain regulate cytosolic aggregation and postsynaptic clustering. *J. Cell Sci.* **120,** 1371–1382 (2007).
41. Andjus, P. R., Stevic-Marinkovic, Z. & Cherubini, E. Immunoglobulins from motoneurone disease patients enhance glutamate release from rat hippocampal neurones in culture. *J. Physiol.* **504,** 103–112 (1997).
42. Atchison, F. W., Capel, B. & Means, A. R. Pin1 regulates the timing of mammalian primordial germ cell proliferation. *Development* **130,** 3579–3586 (2003).
43. Mohler, H. *et al.* Heterogeneity of $GABA_A$-receptors: cell-specific expression, pharmacology, and regulation. *Neurochem. Res.* **20,** 631–636 (1995).
44. Barlow, A. L., MacLeod, A., Noppen, S., Sanderson, J. & Guérin, C. J. Colocalization analysis in fluorescence micrographs: verification of a more accurate calculation of Pearson's correlation coefficient. *Microsc. Microanal.* **16,** 710–724 (2010).
45. Griguoli, M. *et al.* Nicotine blocks the hyperpolarization-activated current Ih and severely impairs the oscillatory behavior of oriens-lacunosum moleculare interneurons. *J. Neurosci.* **30,** 10773–10783 (2010).
46. Traynelis, S. F., Silver, R. A. & Cull-Candy, S. G. Estimated conductance of glutamate receptor channels activated during EPSCs at the cerebellar mossy fiber-granule cell synapse. *Neuron* **11,** 279–289 (1993).
47. Glykys, J. & Mody, I. The main source of ambient GABA responsible for tonic inhibition in the mouse hippocampus. *J. Physiol.* **582,** 1163–1178 (2007).

Acknowledgements

We are grateful to Dr P. Scheiffele (Biozentrum, University of Basel, Basel, Switzerland) for kindly providing us NL2HA cDNA. We thank B. Pastore for her excellent technical support with neuronal cultures. We are extremely grateful to L. Gasperini, E. Meneghetti and F. Ruggeri for their help and for critical discussion during experiments and to E. Grdina for managing the animal house facility. This work was partially supported by grants from Telethon (GGP11043), Human Brain Project (Neuroantibodies #604102) and MIUR (PRIN 2012) to E.C.

Author contributions

R.A., E.C. and P.Z. conceived the project. R.A. performed most of the molecular biology experiments; R.P. and A.P. performed the electrophysiological experiments; G.D.S. and J.-M.F. supplied some reagents; E.C. and P.Z. wrote the manuscript, which was revised by all authors in collaboration.

Additional information

Supplementary Information accompanies this paper at http://www.nature.com/naturecommunications

Competing financial interests: The authors declare no competing financial interests.

Reprints and permission information is available online at http://npg.nature.com/reprintsandpermissions/

How to cite this article: Antonelli, R. *et al.* Pin1-dependent signalling negatively affects GABAergic transmission by modulating neuroligin2/gephyrin interaction. *Nat. Commun.* 5:5066 doi: 10.1038/ncomms6066 (2014).

Chapter 6

Conclusion and Future Perespective

The objective of my PhD thesis was to investigate structural and functional properties of the HCN2 channels. We perform pulling experiments on the purified and functionalized c-linker and CNBD construct from the hHCN2 channel, obtaining a huge amount of data both in the absence and in the presence of the cAMP. We had immediately to deal with an unexpected variability in F-d curves patterns, and several informatics tools have been developed, tested and validated to guarantee a strong automation and reproducibility in the analytic procedures. Our results from SMFS measurement on the construct revealed different unfolding pathways sampled during the mechanical unfolding both in the presence and in the absence of the cyclic nucleotide. Identification and characterization of the single unfolding pathways highlighted differences between the apo and holo configuration of the molecule. Thus, the construct in the presence of the cAMP unfolds predominantly in a three- and four-state like manner, whereas in the absence of the cAMP the construct does not show preferential unfolding routes but single intermediate states appear to be recurrently visited during the mechanical unfolding. Moreover, on the base of the solved crystal structure in the presence of the nucleotide we proposed a structural interpretation for the most conserved unfolding intermediates. Results suggested an independent unfolding behavior of the c-linker and the CNBD in the absence of the cAMP and a major continuum in mechanical stability along the whole molecule in the presence of the cAMP. With this work we revealed the complex nature of the unfolding behaviour of the c-linker + CNBD domain from the hHCN2 channel, and confirmed AFM-based SMFS and our informatics tools as a suitable approach to explore complex or stochastic biological phenomena such as protein folding and unfolding.

The increasing complexity of the problem approached in biological science is redefining the quantity and the quality of collected data, and is becoming necessary to develop strongly reproducible and operator-independent procedures to handle large amount of data, possibly in an automatic manner. Moreover, during the past years we developed several algorithms for F-d curves analysis, and our tools compound has been made more and more strong and complete. For these

reasons, we decide to develop an open-source platform (called FaceTheWind), offering an all-in-one environment for F-d curves analysis. We enclosed in our software both widely accepted statistical features and advanced tools dedicated to protein unfolding studies (i.e. clustering algorithms, automatic trace alignment procedure and unfolding pathways determination). Our purpose would be to create a community of AFM users, for developing, validating and shearing novel analytical methods, and keep them together in an all-in-one open-source software.

A possible continuation of this project may focuses on the investigation of the unfolding behavior of the whole HCN2 channel expressed in physiological environment as already done in our lab on the CNGA1 channel (Maity et al., 2015). Thus, we overexpressed the mHCN2 channel in the heterologous system of *Xenopus Laevis* oocytes and started performed pulling experiment. We are trying to use the most conserved unfolding pathways from the c-liker and CNBD domain as a fingerprint to identify, among the variety of spectra coming from endogenous proteins in oocytes, the candidate traces coming from the HCN channel. Much more data are still required to validate this procedure, but we are confident that it can be the right direction.

The combination of SMFS experiment and automation in analysis procedure may leads to extremely versatile applications.The characterization of F-d curves from purified excised domain or subdomains of complex proteins, pulled from artificial substrates, may represent a valuable method for obtain fingerprints for the identification of those proteins in more variable physiological system. More powerful analytical tools may leads to a faster and stronger characterization of the endogenous spectra in preferential near-physiological system such as *Xenopus Laevis* oocytes, making straightforward the identification of any artificially overexpressed protein. Such a strong approach may quickly lead to the identification of possible common features for entire family of proteins (i.e. ionic channels), disclosing the possibility to perform SMFS measurements in fully-physiological environment like neurons.

Considering that the majority of the human pathologies came from incorrect folding processes, the possibility to have a methodology for a direct identification of unfolding profiles of misfolded proteins in pathological phenotype, comparing with profiles in healthy phenotype, would leads to extreme powerful application in biomedical and pharmacological field.

Chapter 7

Bibliography

Alexander, S., Hellemans, L., Marti, O., Schneir, J., Elings, V., Hansma, P.K., Longmire, M., and Gurley, J. (1989). An atomic-resolution atomic-force microscope implemented using an optical lever. J. Appl. Phys. 65, 164-167.

Altomare, C., Terragni, B., Brioschi, C., Milanesi, R., Pagliuca, C., Viscomi, C., Moroni, A., Baruscotti, M., and DiFrancesco, D. (2003). Heteromeric HCN1-HCN4 channels: a comparison with native pacemaker channels from the rabbit sinoatrial node. J. Physiol. 549, 347-359.

Anfinsen, C.B. (1973). Principles that govern the folding of protein chains. Science 181, 223-230.

Anfinsen, C.B., Redfield, R.R., Choate, W.L., Page, J., and Carroll, W.R. (1954). Studies on the gross structure, cross-linkages, and terminal sequences in ribonuclease. J. Biol. Chem. 207, 201-210.

Anfinsen, C.B., Haber, E., Sela, M., and White, F.H. (1961). The kinetics of formation of native ribonuclease during oxidation of the reduced polypeptide chain. Proc. Natl. Acad. Sci. U. S. A. 47, 1309-1314.

Baldwin, R.L., and Rose, G.D. (1999a). Is protein folding hierarchic? I. Local structure and peptide folding. Trends Biochem. Sci. 24, 26-33.

Baldwin, R.L., and Rose, G.D. (1999b). Is protein folding hierarchic? II. Folding intermediates and transition states. Trends Biochem. Sci. 24, 77-83.

Bell, G.I. (1978). Models for the specific adhesion of cells to cells. Science 200, 618?627.

Berg, B. van den, Clemons, W.M., Collinson, I., Modis, Y., Hartmann, E., Harrison, S.C., and Rapoport, T.A. (2004). X-ray structure of a protein-conducting channel. Nature 427, 36-44.

Berg, J.M., Tymoczko, J.L., Stryer, L., Berg, J.M., Tymoczko, J.L., and Stryer, L. (2002). Biochemistry (W H Freeman).

Betzig, E., Trautman, J.K., Harris, T.D., Weiner, J.S., and Kostelak, R.L. (1991). Breaking the Diffraction Barrier: Optical Microscopy on a Nanometric Scale. Science 251, 1468-1470.

Betzig, E., Finn, P.L., and Weiner, J.S. (1992). Combined shear force and near?field scanning optical microscopy. Appl. Phys. Lett. 60, 2484-2486.

Biel, M., and Michalakis, S. (2009). Cyclic nucleotide-gated channels. Handb. Exp. Pharmacol. 111-136.

Biel, M., Schneider, A., and Wahl, C. (2002). Cardiac HCN Channels: Structure, Function, and Modulation. Trends Cardiovasc. Med. 12, 206-213.

Bigelow, H.R., Petrey, D.S., Liu, J., Przybylski, D., and Rost, B. (2004). Predicting transmembrane beta-barrels in proteomes. Nucleic Acids Res. 32, 2566-2577.

Binnig, G., Rohrer, H., Gerber, C., and Weibel, E. (1982a). Tunneling through a controllable vacuum gap. Appl. Phys. Lett. 40, 178-180.

Binnig, G., Rohrer, H., Gerber, C., and Weibel, E. (1982b). Surface Studies by Scanning Tunneling Microscopy. Phys. Rev. Lett. 49, 57-61.

Binnig, G., Quate, C.F., and Gerber, C. (1986). Atomic Force Microscope. Phys. Rev. Lett. 56, 930-933.

Bowie, J.U. (2005). Solving the membrane protein folding problem. Nature 438, 581-589.

Bryngelson, J.D., and Wolynes, P.G. (1987). Spin glasses and the statistical mechanics of protein folding. Proc. Natl. Acad. Sci. 84, 7524-7528.

Bryngelson, J.D., Onuchic, J.N., Socci, N.D., and Wolynes, P.G. (1995). Funnels, pathways, and the energy landscape of protein folding: a synthesis. Proteins 21, 167-195.

Bustamante, C., Marko, J.F., Siggia, E.D., and Smith, S. (1994). Entropic elasticity of lambda-phage DNA. Science 265, 1599-1600.

Bustamante, C., Rivetti, C., and Keller, D.J. (1997). Scanning force microscopy under aqueous solutions. Curr. Opin. Struct. Biol. 7, 709-716.

Cappella, B., and Dietler, G. (1999). Force-distance curves by atomic force microscopy. Surf. Sci. Rep. 34, 1-104.

Carrion-Vazquez, M., Oberhauser, A.F., Fisher, T.E., Marszalek, P.E., Li, H., and Fernandez, J.M. (2000). Mechanical design of proteins studied by single-molecule force spectroscopy and protein engineering. Prog. Biophys. Mol. Biol. 74, 63-91.

Chen, C.J. (1992). Electromechanical deflections of piezoelectric tubes with quartered electrodes. Appl. Phys. Lett. 60, 132-134.

Chen, S., Wang, J., and Siegelbaum, S.A. (2001). Properties of hyperpolarization-activated pacemaker current defined by coassembly of HCN1 and HCN2 subunits and basal modulation by cyclic nucleotide. J. Gen. Physiol. 117, 491-504.

Cheung, C.L., Hafner, J.H., and Lieber, C.M. (2000). Carbon Nanotube Atomic Force Microscopy Tips: Direct Growth by Chemical Vapor Deposition and Application to High-Resolution Imaging. Proc. Natl. Acad. Sci. U. S. A. 97, 3809-3813.

Cleveland, J.P., Manne, S., Bocek, D., and Hansma, P.K. (1993). A nondestructive method for determining the spring constant of cantilevers for scanning force microscopy. Rev. Sci. Instrum. 64, 403-405.

Cluzel, P., Lebrun, A., Heller, C., Lavery, R., Viovy, J.-L., Chatenay, D., and Caron, F. (1996). DNA: An Extensible Molecule. Science 271, 792-794.

Craven, K.B., and Zagotta, W.N. (2004). Salt bridges and gating in the COOH-terminal region of HCN2 and CNGA1 channels. J. Gen. Physiol. 124, 663-677.

Cuthbertson, J.M., Doyle, D.A., and Sansom, M.S.P. (2005). Transmembrane helix prediction: a comparative evaluation and analysis. Protein Eng. Des. Sel. PEDS 18, 295-308.

DeVecchio, D., and Bhushan, B. (1998). Use of a nanoscale Kelvin probe for detecting wear precursors. Rev. Sci. Instrum. 69, 3618-3624.

DiFrancesco, D. (2010). The Role of the Funny Current in Pacemaker Activity. Circ. Res. 106, 434-446.

DiFrancesco, D., and Tortora, P. (1991). Direct activation of cardiac pacemaker channels by intracellular cyclic AMP. Nature 351, 145-147.

Dill, K.A., and Chan, H.S. (1997). From Levinthal to pathways to funnels. Nat. Struct. Biol. 4, 10-19.

Dill, K.A., and MacCallum, J.L. (2012). The Protein-Folding Problem, 50 Years On. Science 338, 1042-1046.

Dill, K.A., Ozkan, S.B., Shell, M.S., and Weikl, T.R. (2008). The Protein Folding Problem. Annu. Rev. Biophys. 37, 289-316.

Dobson, C.M. (2003). Protein folding and misfolding. Nature 426, 884-890.

Drake, B., Prater, C.B., Weisenhorn, A.L., Gould, S.A., Albrecht, T.R., Quate, C.F., Cannell, D.S., Hansma, H.G., and Hansma, P.K. (1989). Imaging crystals, polymers, and processes in water with the atomic force microscope. Science 243, 1586-1589.

Drenth, J. (2007). Principles of Protein X-Ray Crystallography (Springer Science & Business Media).

Engel, A., and Gaub, H.E. (2008). Structure and mechanics of membrane proteins. Annu. Rev. Biochem. 77, 127-148.

Evans, E. (1998). Energy landscapes of biomolecular adhesion and receptor anchoring at interfaces explored with dynamic force spectroscopy. Faraday Discuss. 1-16.

Evans, E. (2001). Probing the Relation Between Force-Lifetime-and Chemistry in Single Molecular Bonds. Annu. Rev. Biophys. Biomol. Struct. 30, 105-128.

Evans, E., and Ritchie, K. (1997). Dynamic strength of molecular adhesion bonds. Biophys. J. 72, 1541-1555.

Floudas, C.A., Fung, H.K., McAllister, S.R., Mönnigmann, M., and Rajgaria, R. (2006). Advances in protein structure prediction and de novo protein design: A review. Chem. Eng. Sci. 61, 966-988.

Flynn, G.E., Black, K.D., Islas, L.D., Sankaran, B., and Zagotta, W.N. (2007). Structure and rearrangements in the carboxy-terminal region of SpIH channels. Struct.

Lond. Engl. 1993 15, 671-682.

Gauss, R., Seifert, R., and Kaupp, U.B. (1998). Molecular identification of a hyperpolarization-activated channel in sea urchin sperm. Nature 393, 583-587.

Gosse, C., and Croquette, V. (2002). Magnetic tweezers: micromanipulation and force measurement at the molecular level. Biophys. J. 82, 3314-3329.

Han, W., Lindsay, S.M., and Jing, T. (1996). A magnetically driven oscillating probe microscope for operation in liquids. Appl. Phys. Lett. 69, 4111-4113.

Hansma, P.K., Drake, B., Marti, O., Gould, S.A., and Prater, C.B. (1989). The scanning ion-conductance microscope. Science 243, 641-643.

Harris, N.J., and Booth, P.J. (2012). Folding and stability of membrane transport proteins in vitro. Biochim. Biophys. Acta BBA - Biomembr. 1818, 1055-1066.

Heinrich, S.U., Mothes, W., Brunner, J., and Rapoport, T.A. (2000). The Sec61p Complex Mediates the Integration of a Membrane Protein by Allowing Lipid Partitioning of the Transmembrane Domain. Cell 102, 233-244.

Heinz, W.F., and Hoh, J.H. (1999). Spatially resolved force spectroscopy of biological surfaces using the atomic force microscope. Trends Biotechnol. 17, 143-150.

Henderson, R., and Unwin, P.N. (1975). Three-dimensional model of purple membrane obtained by electron microscopy. Nature 257, 28-32.

Hessa, T., Kim, H., Bihlmaier, K., Lundin, C., Boekel, J., Andersson, H., Nilsson, I., White, S.H., and von Heijne, G. (2005). Recognition of transmembrane helices by the endoplasmic reticulum translocon. Nature 433, 377-381.

Huang, C., Lin, Y.Y., and Tang, T.A. (2004). Study on the tip-deflection of a piezoelectric bimorph cantilever in the static state. J. Micromechanics Microengineering 14, 530.

Hutter, J.L., and Bechhoefer, J. (1993). Calibration of atomic?force microscope tips. Rev. Sci. Instrum. 64, 1868-1873.

Ishii, T.M., Takano, M., Xie, L.H., Noma, A., and Ohmori, H. (1999). Molecular characterization of the hyperpolarization-activated cation channel in rabbit heart sinoatrial node. J. Biol. Chem. 274, 12835-12839.

Ji, X.-L., and Liu, S.-Q. (2011). Is stoichiometry-driven protein folding getting out of thermodynamic control? J. Biomol. Struct. Dyn. 28, 621?623; discussion 669-674.

Kedrov, A., Janovjak, H., Sapra, K.T., and Müller, D.J. (2007). Deciphering molecular interactions of native membrane proteins by single-molecule force spectroscopy. Annu. Rev. Biophys. Biomol. Struct. 36, 233-260.

Kendrew, J.C., Bodo, G., Dintzis, H.M., Parrish, R.G., Wyckoff, H., and Phillips, D.C. (1958). A three-dimensional model of the myoglobin molecule obtained by x-ray analysis. Nature 181, 662-666.

Kendrew, J.C., Dickerson, R.E., Strandberg, B.E., Hart, R.G., Davies, D.R., Phillips, D.C., and Shore, V.C. (1960). Structure of Myoglobin: A Three-Dimensional Fourier Synthesis at 2 |[angst]|. Resolution. Nature 185, 422-427.

Kim, S., Blainey, P.C., Schroeder, C.M., and Xie, X.S. (2007). Multiplexed single-molecule assay for enzymatic activity on flow-stretched DNA. Nat. Methods 4, 397-399.

Kishino, A., and Yanagida, T. (1988). Force measurements by micromanipulation of a single actin filament by glass needles. Nature 334, 74-76.

Kuwajima, K. (1989). The molten globule state as a clue for understanding the folding and cooperativity of globular-protein structure. Proteins Struct. Funct. Bioinforma. 6, 87-103.

Kyte, J., and Doolittle, R.F. (1982). A simple method for displaying the hydropathic character of a protein. J. Mol. Biol. 157, 105-132.

Lee, G.U., Kidwell, D.A., and Colton, R.J. (1994). Sensing Discrete Streptavidin-Biotin Interactions with Atomic Force Microscopy. Langmuir 10, 354-357.

Leopold, P.E. (1992). Protein Folding Funnels: Kinetic Structure of Compact Conformation Space. PhD Thesis.

Leopold, P.E., Montal, M., and Onuchic, J.N. (1992). Protein folding funnels: a kinetic approach to the sequence-structure relationship. Proc. Natl. Acad. Sci. 89, 8721-8725.

Levinthal, C. (1968). Are there pathways for protein folding. J Chim Phys 65, 44-45.

Levinthal, C. (1969). How to fold graciously. Mossbauer Spectrosc. Biol. Syst. 67, 22-24.

Lu, H., and Booth, P.J. (2000). The final stages of folding of the membrane protein bacteriorhodopsin occur by kinetically indistinguishable parallel folding paths that are mediated by pH. J. Mol. Biol. 299, 233-243.

Ludwig, A., Zong, X., Jeglitsch, M., Hofmann, F., and Biel, M. (1998). A family of hyperpolarization-activated mammalian cation channels. Nature 393, 587-591.

Luheshi, L.M., Crowther, D.C., and Dobson, C.M. (2008). Protein misfolding and disease: from the test tube to the organism. Curr. Opin. Chem. Biol. 12, 25-31.

Männikkö, R., Elinder, F., and Larsson, H.P. (2002). Voltage-sensing mechanism is conserved among ion channels gated by opposite voltages. Nature 419, 837-841.

Marko, J.F., and Siggia, E.D. (1995). Stretching DNA. Macromolecules 28, 8759-8770.

Marti, O., Colchero, J., and Mlynek, J. (1990). Combined scanning force and friction microscopy of mica. Nanotechnology 1, 141.

Martin, Y., and Wickramasinghe, H.K. (1987). Magnetic imaging by "force microscopy" with 1000 Åresolution. Appl. Phys. Lett. 50, 1455-1457.

Marx, T., Gisselmann, G., Störtkuhl, K.F., Hovemann, B.T., and Hatt, H. (1999). Molecular cloning of a putative voltage- and cyclic nucleotide-gated ion channel present in the antennae and eyes of Drosophila melanogaster. Invertebr. Neurosci. IN 4, 55-63.

Mate, C.M., McClelland, G.M., Erlandsson, R., and Chiang, S. (1987). Atomic-Scale Friction of a Tungsten Tip on a Graphite Surface. In Scanning Tunneling Microscopy, H. Neddermeyer, ed. (Springer Netherlands), pp. 226-229.

Milne, J.L.S., Borgnia, M.J., Bartesaghi, A., Tran, E.E.H., Earl, L.A., Schauder, D.M., Lengyel, J., Pierson, J., Patwardhan, A., and Subramaniam, S. (2013). Cryo-electron microscopy: A primer for the non-microscopist. FEBS J. 280, 28-45.

Moult, J. (1999). Predicting protein three-dimensional structure. Curr. Opin. Biotechnol. 10, 583-588.

Moy, V.T., Florin, E.L., and Gaub, H.E. (1994). Intermolecular forces and energies between ligands and receptors. Science 266, 257-259.

Much, B., Wahl-Schott, C., Zong, X., Schneider, A., Baumann, L., Moosmang, S., Ludwig, A., and Biel, M. (2003). Role of subunit heteromerization and N-linked glycosylation in the formation of functional hyperpolarization-activated cyclic nucleotide-gated channels. J. Biol. Chem. 278, 43781-43786.

Müller, D.J., and Engel, A. (1997). The height of biomolecules measured with the atomic force microscope depends on electrostatic interactions. Biophys. J. 73, 1633-1644.

Napoli, M., Bamieh, B., and Turner, K. (2003). Mathematical modeling, experimental validation and observer design for a capacitively actuated microcantilever. (IEEE), pp. 3732-3737.

Neubauer, G., Cohen, S.R., McClelland, G.M., Horne, D., and Mate, C.M. (1990). Force microscopy with a bidirectional capacitance sensor. Rev. Sci. Instrum. 61, 2296-2308.

Nonnenmacher, M., O?Boyle, M.P., and Wickramasinghe, H.K. (1991). Kelvin probe force microscopy. Appl. Phys. Lett. 58, 2921-2923.

Ohgushi, M., and Wada, A. (1983). "Molten-globule state": a compact form of globular proteins with mobile side-chains. FEBS Lett. 164, 21-24.

Onuchic, J.N., Wolynes, P.G., Luthey-Schulten, Z., and Socci, N.D. (1995). Toward an outline of the topography of a realistic protein-folding funnel. Proc. Natl. Acad. Sci. U. S. A. 92, 3626-3630.

Pauling, L., and Corey, R.B. (1951). Atomic Coordinates and Structure Factors for Two Helical Configurations of Polypeptide Chains. Proc. Natl. Acad. Sci. U. S. A. 37, 235-240.

Pauling, L., Corey, R.B., and Branson, H.R. (1951). The structure of proteins: Two hydrogen-bonded helical configurations of the polypeptide chain. Proc. Natl. Acad. Sci. 37, 205-211.

Perutz, M.F., Rossmann, M.G., Cullis, A.F., Muirhead, H., Will, G., and North, A.C.T. (1960). Structure of Haemoglobin: A Three-Dimensional Fourier Synthesis at 5.5-|[angst]|. Resolution, Obtained by X-Ray Analysis. Nature 185, 416-422.

Popot, J.L., and Engelman, D.M. (1990). Membrane protein folding and oligomerization: the two-stage model. Biochemistry (Mosc.) 29, 4031-4037.

Postea, O., and Biel, M. (2011). Exploring HCN channels as novel drug targets. Nat. Rev. Drug Discov. 10, 903-914.

Rapoport, T.A. (2007). Protein translocation across the eukaryotic endoplasmic reticulum and bacterial plasma membranes. Nature 450, 663-669.

Roder, H., Elöve, G.A., and Englander, S.W. (1988). Structural characterization of folding intermediates in cytochrome c by H-exchange labelling and proton NMR. Nature 335, 700-704.

Sader, J.E., Larson, I., Mulvaney, P., and White, L.R. (1995). Method for the calibration of atomic force microscope cantilevers. Rev. Sci. Instrum. 66, 3789-3798.

Sadlish, H., Pitonzo, D., Johnson, A.E., and Skach, W.R. (2005). Sequential triage of transmembrane segments by Sec61? during biogenesis of a native multispanning membrane protein. Nat. Struct. Mol. Biol. 12, 870-878.

Santoro, B., Liu, D.T., Yao, H., Bartsch, D., Kandel, E.R., Siegelbaum, S.A., and Tibbs, G.R. (1998). Identification of a gene encoding a hyperpolarization-activated pacemaker channel of brain. Cell 93, 717-729.

Saponaro, A., Pauleta, S.R., Cantini, F., Matzapetakis, M., Hammann, C., Donadoni, C., Hu, L., Thiel, G., Banci, L., Santoro, B., et al. (2014). Structural basis for the mutual antagonism of cAMP and TRIP8b in regulating HCN channel function. Proc. Natl. Acad. Sci. 111, 14577-14582.

Semisotnov, G.V., Rodionova, N.A., Razgulyaev, O.I., Uversky, V.N., Gripas', A.F., and Gilmanshin, R.I. (1991). Study of the "molten globule" intermediate state in protein folding by a hydrophobic fluorescent probe. Biopolymers 31, 119-128.

Senden, T., and Ducker, W. (1994). Experimental Determination of Spring Constants in Atomic Force Microscopy. Langmuir 10, 1003-1004.

Stern, J.E., Terris, B.D., Mamin, H.J., and Rugar, D. (1988). Deposition and imaging of localized charge on insulator surfaces using a force microscope. Appl.

Phys. Lett. 53, 2717?2719. Tanford, C. (1978). The Hydrophobic Effect and the Organization of Living Matter. Science 200, 1012-1018.

Taraska, J.W., Puljung, M.C., Olivier, N.B., Flynn, G.E., and Zagotta, W.N. (2009). Mapping the structure and conformational movements of proteins with transition metal ion FRET. Nat. Methods 6, 532-537.

Tieleman, D.P., Sansom, M.S., and Berendsen, H.J. (1999). Alamethicin helices in a bilayer and in solution: molecular dynamics simulations. Biophys. J. 76, 40-49.

Torii, A., Sasaki, M., Hane, K., and Okuma, S. (1996). A method for determining the spring constant of cantilevers for atomic force microscopy. Meas. Sci. Technol. 7, 179.

Wahl-Schott, C., and Biel, M. (2009). HCN channels: structure, cellular regulation and physiological function. Cell. Mol. Life Sci. CMLS 66, 470-494.

Wainger, B.J., DeGennaro, M., Santoro, B., Siegelbaum, S.A., and Tibbs, G.R. (2001). Molecular mechanism of cAMP modulation of HCN pacemaker channels. Nature 411, 805?810. White, S.H. (2007). Membrane protein insertion: the biology-physics nexus. J. Gen. Physiol. 129, 363-369.

Williams, C.C., and Wickramasinghe, H.K. (1990). Microscopy of chemical-potential variations on an atomic scale. Nature 344, 317-319.

Wilson, N.R., and Macpherson, J.V. (2009). Carbon nanotube tips for atomic force microscopy. Nat. Nanotechnol. 4, 483-491.

Wuthrich, K. (1986). NMR of proteins and nucleic acids. George Fish. Bak. Non-Resid. Lecturesh. Chem. Cornell Unversity USA.

Yeh, M.K., Chen, B.Y., Tai, N.H., and Chiu, C.C. (2006). Force Measurement by AFM Cantilever with Different Coating Layers. Key Eng. Mater. 326-328, 377-380.

Yon, J.M. (2002). Protein folding in the post-genomic era. J. Cell. Mol. Med. 6, 307-327.

Zagotta, W.N., Olivier, N.B., Black, K.D., Young, E.C., Olson, R., and Gouaux, E. (2003). Structural basis for modulation and agonist specificity of HCN pacemaker channels. Nature 425, 200-205.

Zhou, L., and Siegelbaum, S.A. (2007). Gating of HCN channels by cyclic nucleotides: residue contacts that underlie ligand binding, selectivity, and efficacy. Struct. Lond. Engl. 1993 15, 655-670.

Zlatanova, J., Lindsay, S.M., and Leuba, S.H. (2000). Single molecule force spectroscopy in biology using the atomic force microscope. Prog. Biophys. Mol. Biol. 74, 37-61.

Zocher, M., Bippes, C.A., Zhang, C., and Müller, D.J. (2013). Single-molecule force spectroscopy of G-protein-coupled receptors. Chem. Soc. Rev. 42, 7801-7815.